Structural and Biochemical Characterization of Ligand Bound States of the FeMo-cofactor of Nitrogenase

Thesis by

Kathryn A Pérez

In Partial Fulfillment of the Requirements for

the degree of

Doctor of Philosophy

CALIFORNIA INSTITUTE OF TECHNOLOGY

Pasadena, California

2016

(Defended 19 April 2016)

ABSTRACT

Nitrogenase is the only known enzyme capable of nitrogen fixation, the reduction of dintrogen to ammonia, a metabolically available form of nitrogen. Developing an understanding of the complex mechanism required for biological nitrogen fixation requires that the enzyme be characterized in catalytically relevant states, such as those involving ligand binding and reduction. Nitrogenase catalyzes this reaction through the cyclic interaction of two metalloproteins, the Fe-protein and the MoFe-protein which contain three distinct metalloclusters, in an ATP-hydrolysis dependent electron transfer reaction. The binding and subsequent reduction of substrates requires multiple electrons donated from the Fe-protein to the MoFe-protein, in which the active site is located. In this study, we have structurally characterized the binding of two inhibitors to the FeMo-cofactor, CO and the Se of $SeCN^-$. Both interactions involve the displacement of a single S, and the Se was used as a label to follow the interchange of three S sites within the FeMo-cofactor during catalysis. These finding change any future approaches to characterize the mechanism of biological nitrogen fixation, requiring that structural changes be considered for substrate binding and reduction.

PUBLISHED CONTENT AND CONTRIBUTIONS

Spatzal, T.[*], Perez K. A.[*], Howard J. B., Rees, D. C. (2015) "Catalysis-dependent selenium incorporation and migration in the nitrogenase active site iron-molybdenum cofactor". In: eLife; 4: e11620. doi: http://dx.doi.org/10.7554/eLife.11620

[*]These authors contributed equally to this work: Thomas Spatzal & Kathryn A Perez

KAP, Purified, crystallized and biochemically characterized the enzyme samples, and collected the X-ray crystallographic data; Processed, refined and analyzed the X-ray data; Contributed equally to the study; Discussed the results and participated in writing the manuscript.

Spatzal, T., Perez K. A., Einsle, O., Howard J. B., Rees, D. C. (2014) "Ligand binding to the FeMo-cofactor: Structures of CO-bound and reactivated nitrogenase". In: Science 345, pp. 1620-1623. doi: 10.1126/science.1256679

KAP, Purified, crystallized and biochemically characterized the enzyme samples, and collected the X-ray crystallographic data; assisted with processing, refining and analyzing the X-ray data; Discussed the results and participated in writing the manuscript.

TABLE OF CONTENTS

LIST OF ILLUSTRATIONS AND/OR TABLES

Table number *Page*

Introduction

Summary

Nitrogenase is the only known enzyme capable of reducing dintrogen to ammonia in a process called biological nitrogen fixation. This step within the nitrogen cycle is key to transforming inert dintrogen into a metabolically available form due to the immense nitrogen requirement by all biological systems in the production of amino acids and nucleic acids. Nitrogenase is composed of two proteins, the Fe-protein and the MoFe-protein. The two component proteins contain three metalloclusters central to the reduction of substrates. The Fe-protein contains a single [4Fe:4S] cluster responsible for electron transfer to the MoFe-protein. The MoFe-protein contains two unique metalloclusters: the P-cluster [8Fe:7S], and the nitrogenase active site, the FeMo-cofactor [7Fe:9S:Mo:C]-*R*-homocitrate. The nitrogenase mechanism is not well-understood, which is reflective of the complex nature of this catalytic process and the poorly characterized electronic structure of the FeMo-cofactor.

The work described herein focused on the characterization of CO-ligand binding and catalytically-dependent selenium incorporation and migration in the FeMo-cofactor. X-ray crystallography, kinetic analysis, continuous-wave electron paramagnetic resonance (cw-EPR) spectroscopy, and electron spin echo envelope modulation (ESEEM) spectroscopy were used to explore the properties of these states.

A crystallographic structure was refined from data collected on crystals of CO-inhibited MoFe-protein. Characterization of this ligand-bound state required the preparation of a CO-inhibited sample for protein crystallization from a heterogeneous mix of both component proteins in an assay containing an ATP-regeneration system. The data resulted in the first ligand-bound structure of the FeMo-cofactor, demonstrating that the active site undergoes structural changes upon ligand binding, replacing a bridging sulfur with a CO. Upon reactivation of the CO-inhibited MoFe-protein, the CO dissociated and the site was re-

occupied with a sulfur, demonstrating that the structure of the CO-inhibited protein was of mechanistic relevance for ligand binding.

Following the recognition of a sulfur dissociating from the FeMo-cofactor upon ligand binding, we identified and characterized a selenium containing inhibitor of substrate reduction, $SeCN^-$, and determined the structure of the inhibited MoFe-protein. The $SeCN^-$ inhibited MoFe-protein structure, Av1_Se2B, showed that the same site where CO binds to the cofactor had a selenium atom, site specifically incorporated. Determination of the catalytic activity of the Se-incorporated FeMoco and structural characterization of the protein following catalytic turnover resulted in migration of the selenium through three sulfur sites. Time-dependent analysis of turnover-dependent migration culminated in a series of structures showing migration to the three FeMo-cofactor sites, indicating structural rearrangements occurring that involved the labilization of three sulfur atoms during catalysis.

Additionally, inspection of the CO-inhibited structure revealed electron density at a pocket in the MoFe-protein possibly corresponding to the binding site for a sulfur species. The pocket is lined with positively charged amino acids, making it a possible anion-binding site. Non-specific anion binding at this site was tested by co-crystallization of the MoFe-protein with NaBr, NaI, and KSCN, revealing no increased density at the site with NaBr or NaI, but analysis of both electron density and anomalous difference density maps indicated that a SCN^- anion could occupy this site. Inspection of the Av1_Se2B structures resulted in identification of increased electron density at this site, possibly by a low-occupancy Se atom, although no Se was identified at this site in the Se-migration freeze-quench experiments. The biological relevance of this site is not clear from these experiments. Further experiments must be run to identify if it is a sulfur-binding pocket used to store a sulfur atom to bind at the FeMo-cofactor after dissociation of ligands.

Due to the unique crystallographic and spectroscopic properties of selenium, cw-EPR and ESEEM measurements were performed in collaboration with the Weber and Einsle labs, at

Albert-Ludwigs-Universität Freiburg, on Av1_Se2B samples with natural abundance and ^{77}Se isotopically labeled selenium. Initial spectral analysis indicates zero-field splitting of the principal g-values, and identification of peaks only present in the isotopically labeled ESEEM spectra indicate hyper fine coupling. The physical characteristics resulting in this data are not determined, although these experiments provide important information to determine electronic and magnetic details of the FeMo-cofactor.

The Nitrogen Cycle

Nitrogen is essential to all living organisms, as a necessary component of amino acids and nucleic acids, the building blocks of life. Despite the fact that our atmosphere contains approximately 78% nitrogen, atmospheric dinitrogen is inert under most conditions, making it unavailable for uptake into biological systems. In order to ensure bioavailability of nitrogen compounds, many enzymes have evolved to interconvert different forms of nitrogen for use in various metabolic pathways in a process called the nitrogen cycle.

The Nitrogen Cycle involves the chemical transformations that dinitrogen undergoes in the ecosystem. This cycle includes multiple steps that reduce and oxidize nitrogen compounds in order to introduce nitrogen into systems and return it to the atmosphere in the form of N_2. The main processes involved include: nitrogen fixation, nitrification (ammonia oxidation, nitrite oxidation), denitrification, and anaerobic ammonium oxidation (anamox) [4] (see fig 1).

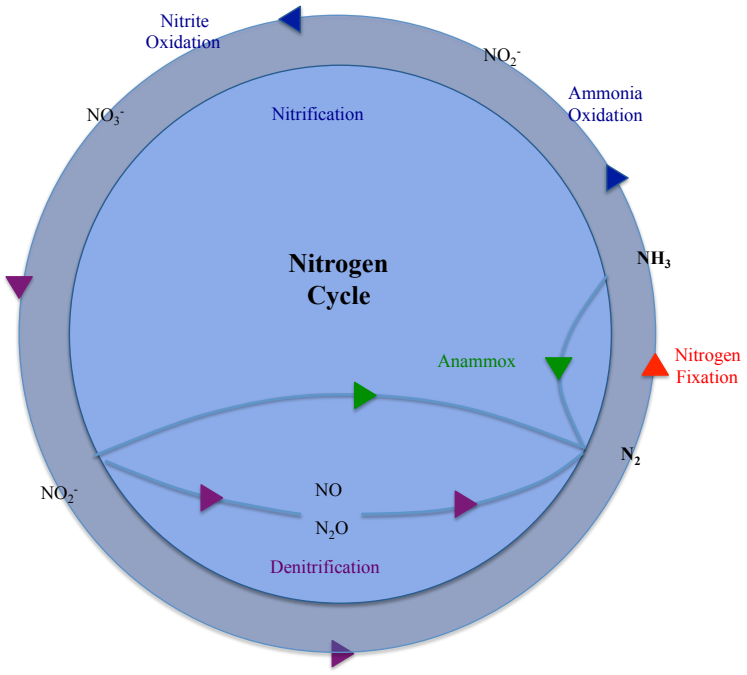

Figure 1: Major reactions in the nitrogen cycle. (this figure is based upon figure 1 in [4])

Nitrogen Fixation

Nitrogen fixation is the reduction of inert dinitrogen to produce ammonia, a chemically and metabolically available form of nitrogen, and is the only process capable of introducing N_2 into the Nitrogen cycle.

The overall chemical equation describing nitrogen fixation is:

$$N_2 + 6H^+ + 6e^- \rightarrow 2NH_3$$

This reaction is thermodynamically favorable (the overall Gibbs free energy of NH3 formation from N_2 is -16 kJ/mol), but kinetically unfavorable (at ambient temperatures) due to the strong NN triple bond (the bond dissociation enthalpy for N_2 is 941 kJ/mol) that creates an insurmountable activation energy when not in the presence of a catalyst (see figure 2). The catalyzed formation of NH_3 may to occur through the formation of intermediates through 2- and 4- proton and electron N_2 reduced species (diazene and hydrazine) which both have enthalpies of formation that require energy input (diazene: +212 kJ/mol, hydrazine: +95 kJ/mol). [5]

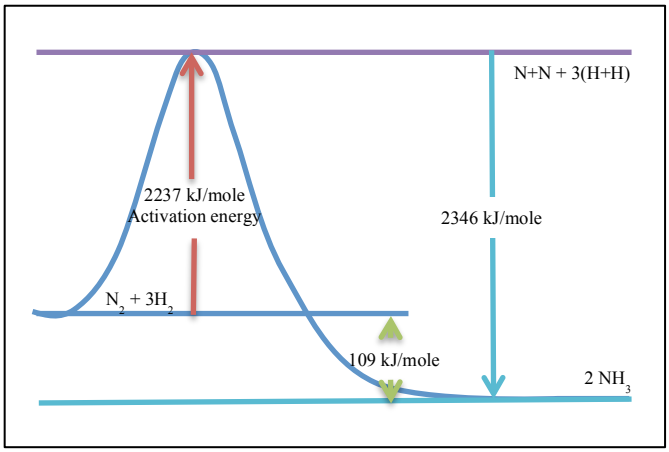

Figure 2: The energy barrier for reducing N_2 to produce NH_3 [6].

Nitrification (aerobic)

From ammonia, nitrates can be formed via oxidation, in a process called nitrification. In this multistep process, ammonia, NH_3, is converted to nitrite, NO_2^-, and then finally to nitrate, NO_3^- [4].

The enzymatic conversion of NH_3 to NO_2^- involves a two-step process in which ammonia is first oxidized to hydroxylamine by the enzyme ammonia monooxygenase, followed by a second oxidation step converting hydroxylamine to nitrite by the enzyme hydroxylamine oxidoreductase. The overall reactions for nitrification are:

1) $NH_3 + O_2 + 2e^- + 2H^+ \rightarrow NH_2OH + H_2O$
2) $NH_2OH + H_2O \rightarrow NO_2^- + 5H^+ + 4e^-$

Nitrite oxidation to produce nitrate is performed by nitrite-oxidizing bacteria. The overall chemical reaction is: $NO_2^- + ½\ O_2 \rightarrow NO_3^-$

Anammox (anaerobic ammonia oxidation)

Anammox is the anaerobic oxidation of ammonia by anammox bacteria that uses nitrite as an electron acceptor, with N_2 and water as the end products [4]. The bacteria responsible for anammox are of the phylum Plantomycetes [7]. The overall chemical reaction occurring during anammox is:

$NH_4^+ + NO_2^- \rightarrow N_2 + 2H_2O$

Denitrification (anaerobic)

Denitrification is the process by which nitrate is converted back to dinitrogen. The multistep denitrification process also produces other gaseous nitrogen species such as NO and N_2O. The overall reaction steps for denitrification are:

1) $NO_3^- \rightarrow NO_2^- \rightarrow NO + N_2O \rightarrow N_2$

The complete redox reaction of denitrification is:

2) $2NO_3^- + 10e^- + 12H^+ \rightarrow N_2 + 6H_2O$

The Nitrogen Cycle is a very important part of the biogeochemical system. The production and consumption of such a variety of nitrogen compounds highlights the complexity and necessity of this delicately balanced process. The global nitrogen cycle has been altered significantly due to human activity, with benefits deriving from increased food production, and drawbacks from negative human health issues, decreased biodiversity, and climate change. Due to the enormous impacts from anthropomorphic influence, developing a

greater understanding of this cycle as a whole and the individual reactions within it are important for maintaining sustainability [8].

Nitrogen Fixation

Nitrogen Fixation is the only step in the nitrogen cycle in which N_2 is introduced into the cycle as a metabolically available and chemically active form. Due to the significant biological requirements for nitrogen, nitrogen fixation is one of the most impactful biochemical processes.

There are two main sources for producing ammonia: nitrogenase, and the industrial Haber-Bosch process. Nitrogenase is a two-component metalloenzyme, and is produced in a small group of mainly bacteria, and some archaea, called diazotrophs. Nitrogenase carries out biological nitrogen fixation in an ATP hydrolysis-dependent reaction at physiological temperatures and pressures (~25°C, 1 atm) in the absence of oxygen (it should be noted that the enzyme is oxygen sensitive, but diazotrophs survive in a variety of conditions).

The Haber-Bosch process utilizes an iron catalyst and high temperatures (300-500°C) and high pressures (15-25 MPa) to carry out industrial nitrogen fixation. This process provides nitrogen for fertilizers and is used in producing ~50% of the world food supply, making it incredibly important for supporting the current world population [9]. Unfortunately, the extreme conditions required for this process lead to many consequences including consumption of approximately 1-2% of world energy production [8, 9]. In addition, the application of nitrogen fertilizer has not been limited, and so additional consequences derive from widespread overuse of nitrogen rich fertilizer and consequent leakage into soils, vegetation, and water. Denitrification of these sources leads to the production of many reactive species (i.e. NO_x into the atmosphere) and long term increased concentrations of nitrogen species (such as in the oceans where nitrogen species can easily accumulate) [8].

Developing an understanding of biological nitrogen fixation provides a pathway to address energy concerns related to the Haber-Bosch process by providing biological inspiration for the synthesis of nitrogen-fixing analogs.

Diazotrophs

Diazotrophs are organisms capable of nitrogen fixation; of the nitrogen-fixing organisms known, most are bacteria and some are archaea. Diazotrophs exist as both free-living organisms and in symbiotic systems. Free-living diazotrophs include both anaerobic (such as *Clostridium*) and aerobic (such as *Azotobacter*) bacteria as well as photosynthetic bacteria (such as cyanobacteria; these include aerobic and anaerobic photosynthetic systems). Symbiotic diazotrophs include organisms such as rhizobia, found in nodules of legume plant roots, and symbiotic cyanobacteria that associate with fungi as lichens or with ferns and cycads.

Azotobacter vinelandii

Of the diazotrophs, *Azotobacter vinelandii* is the best characterized with respect to nitrogenase production, and thus is an excellent model for studying biological nitrogen fixation. *Azotobacter vinelandii* is an obligate aerobe, gram-negative soil bacterium of the class *Gammaproteobacteria* [10]. It produces Mo-dependent nitrogenase, but under conditions of limited Mo, will produce the V- and Fe-only- dependent nitrogenase [11, 12].

Nitrogenase is an anaerobic enzyme, and is irreversibly inactivated by contact with O_2. Due to this caveat for enzymatic activity, *Azotobacter vinelandii* has a high rate of oxidative respiration, thus providing an anoxic environment within the cell. *Azotobacter vinelandii* produces five terminal oxidases in combination with multiple NADH-dependent respiratory complexes to ensure high respiration and ATP production rates [13]. Additionally, oxidases from *Azotobacter vinelandii* have increased affinity for oxygen relative to other organisms [14].

Azotobacter vinelandii requires a complex set of maturation proteins with approximately 82

genes associated with the formation and regulation of nitrogenase production [15]. The 82 genes associated with nitrogenase production are organized into 16 different gene clusters, with specific genes associated with production of the nitrogenase enzyme with molybdenum, vanadium, or iron-only, termed "Nif", "Vnf", and "Anf", respectively. These genes encode proteins associated with nitrogenase production and assembly, regulation, and housekeeping, indicating a complex system for performing nitrogen fixation [15].

Nitrogenase

Nitrogenase is the only known enzyme capable of biological nitrogen fixation, the reduction of N_2 to produce NH_3. The stoichiometric biological reduction of nitrogen is:

$$N_2 + 8H^+ + 8e^- + 16ATP + \rightarrow 2NH_3 + 16ADP + 16P_i$$

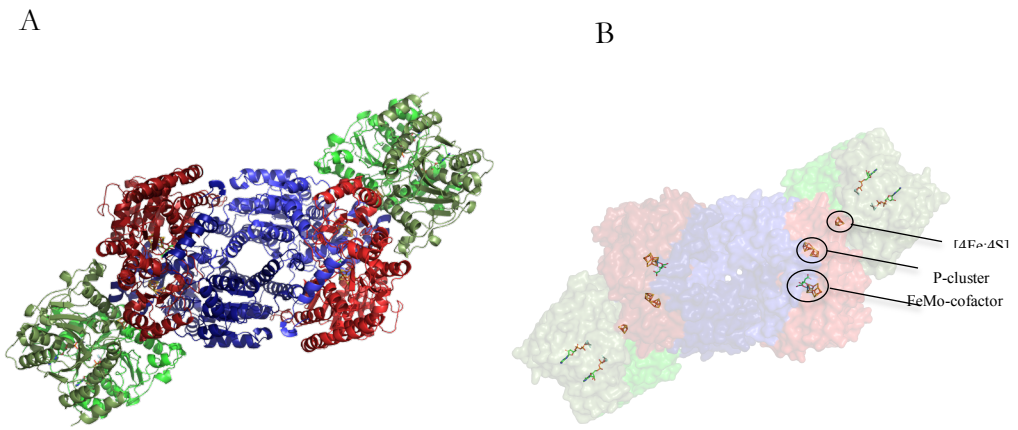

Figure 3: Nitrogenase complex. [from PDB: 1N2C]

A) The nitrogenase complex shown in ribbon diagram. In green is the Fe-protein dimer, and in blue and red is the MoFe-protein $\alpha_2\beta_2$ heterotetramer. B) The nitrogenase complexes are shown with the metal clusters highlighted. In the Fe-protein (green), two ADP·AlF_4 are shown bound to each dimer and the Fe_4S_4 cluster is at the dimer interface. In the MoFe protein, the P-cluster and FeMo-cofactor are highlighted, with one set of metalloclusters per $\alpha\beta$ unit.

Nitrogenase utilizes two proteins (which contain three different metalloclusters), ATP, and endogenous ferredoxins/flavodoxins to ultimately reduce N_2 under ambient conditions. Nitrogenase consists of two proteins, the MoFe protein and the Fe protein; the Fe protein is

a homodimer with a [4Fe:4S] cluster at the interface between the two subunits, and the MoFe protein is an $\alpha_2\beta_2$ heterotetramer with each $\alpha\beta$ dimer forming a single catalytic unit containing two unique metalloclusters, the P-cluster and the FeMo-cofactor (see figure 3). The P-cluster [8Fe:7S] acts as an intermediate electron acceptor/donor, receiving electrons from the Fe-protein and delivering them to the FeMo-cofactor, the active site for substrate reduction. The FeMo-cofactor is the most complex metallocluster known in biology, consisting of a three-fold symmetric [7Fe:9S:Mo:C]-*R*-homocitrate complex. During biological nitrogen fixation, ferredoxins/flavodoxins deliver initial electrons to the Fe-protein, followed by an ATP-hydrolysis dependent electron transfer from the Fe-protein to the MoFe-protein.

Iron Protein

Figure 4: Fe-Protein structure (PDB: 2N1P): from top view down the 2-fold molecular symmetry axis (left), side view (right).

The iron protein is the only known reductant of the MoFe-protein capable of driving NH_3 production. The iron protein is a 60 kDa homodimer (γ_2), and has a single [4Fe:4S] cluster at the interface between the two monomers, coordinated by two cysteines in each subunit (Cys97 and Cys132) (see figure 4) [16]. The iron protein is a member of the MinD family of the SIMIBI (Signal Recognition Particle, MinD and BioD) class of NTPases which all contain a deviant Walker A motif [17], demonstrating a KGG signature sequence. The iron protein binds two MgATP per dimer, with the ATPs oriented parallel to the dimer interface with the phosphate groups bound at the Walker A motif [18]. The Fe-protein interacts with

and transfers electrons to the MoFe-protein. Upon binding, the Fe protein undergoes structural changes, including a ~13 degree rotation of each monomer, and a shift of the [4Fe:4S] cluster ~4 Å towards the surface of the complex [19].

Each monomer contains some common elements of nucleotide binding proteins, including: predominant beta-sheets flanked by alpha helices, a Walker-A motif, and two switch regions (switch I and switch II) that interact with the gamma phosphate of bound ATP (see figure 5) [20]. Each monomer has a structure described as an eight stranded β-sheet flanked by nine α-helices. The β-sheet core is composed of seven parallel and one anti-parallel strands [21]. Upon ATP hydrolysis, the two switch regions undergo conformational changes resulting in dissociation with the gamma phosphate. In this way, the two switch regions act as conformational change relays, inducing changes to other molecules bound in these regions dependent upon the bound nucleotide state [20].

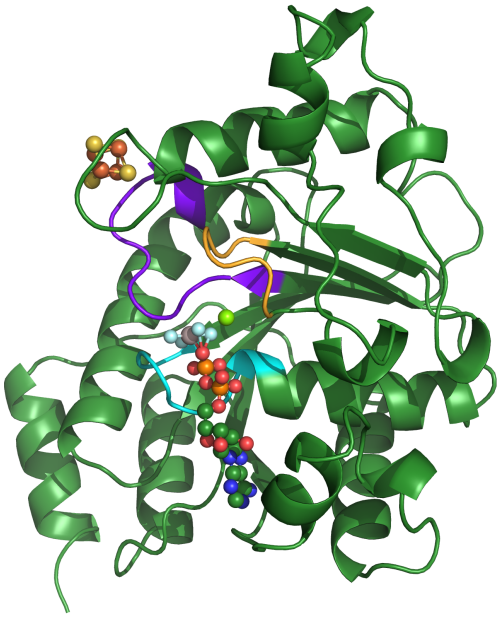

Figure 5: Fe-protein monomer (from PDB: 1N2C): highlighted are Walker-A motif (cyan) corresponding with residues 9-16, switch I region (orange) corresponding to residues 38-43, and switch II region (purple) corresponding to residues 125-135.

In addition to participating as a reductase, the Fe protein has also been shown to act as a Mo-homocitrate insertase, participating in the maturation of the FeMo-cofactor. [22]. *In vitro,* the Fe protein inserts molybedenum and the homocitrate moiety in an ATP-

dependent reaction, with the pre-formed Mo-free precursor metallocluster on NifEN (NifEN is the maturase protein for the FeMo-cofactor). After Fe-protein dependent maturation, the active FeMo-cofactor is transferred into the MoFe-protein [7]. Where molybdenum and homocitrate bind and how they are inserted remain unknown.

[4Fe:4S] Cluster

[4Fe:4S] clusters are ubiquitous within biological systems, participating in redox reactions and exhibiting a broad range of midpoint potentials, making them very versatile [23]. These iron-sulfur clusters can occupy four oxidation states, between 0 and +3, with the +1 and +3 oxidation states being spin active for analysis by EPR (the 0 state in nitrogenase Fe-protein has a S=4 spin and is EPR active [24, 25]), whereas the +2 state is EPR silent. The +1 state exhibits an axial spectrum, and is not heavily influenced by the polypeptide environment. In contrast, the +3 state exhibits a rhombic signal, and demonstrates variability due to the polypeptide environment.

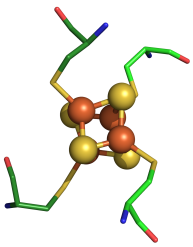

The [4Fe:4S] cluster of the nitrogenase Fe protein (left) is coordinated by the thiol groups of two cysteines from each monomer (Cys97 and Cys132), and is solvent accessible. Upon interaction with the MoFe protein (and MgATP binding), it is shifted toward the surface of the MoFe protein, making the distance between the [4Fe:4S] cluster and the P-cluster 14 Å, providing strong evidence for electron transfer from the [4Fe:4S] cluster to the P-cluster [18]. It is debated within the field if the cluster cycles between a +1/+2 oxidation state, or if an all-ferrous state is biologically relevant [26]. The cycling between an all-ferrous state and the +2 state could imply a 2 e- transfer for every two ATP hydrolyzed, whereas the +1/+2 cycling would imply a single electron transferred per two ATP hydrolyzed [26]. Differences in measured midpoint potentials for each oxidation state are likely affected by structural rearrangements occurring upon complex formation between the Fe- and MoFe- proteins, and electrochemical measurements may have been affected by the reductants (i.e. dithionite or Ti(III)citrate) used in each experiment [26]).

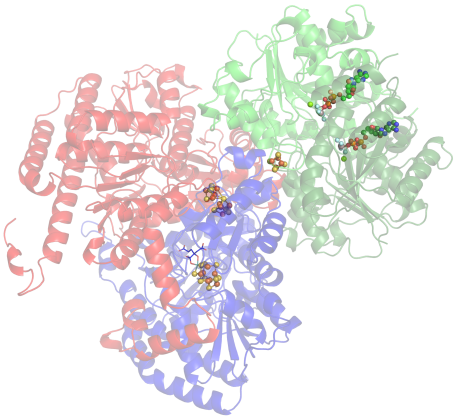

Figure 6: Nitrogenase single catalytic unit modeled in cartoon. (from PDB: 1N2C)

MoFe-protein

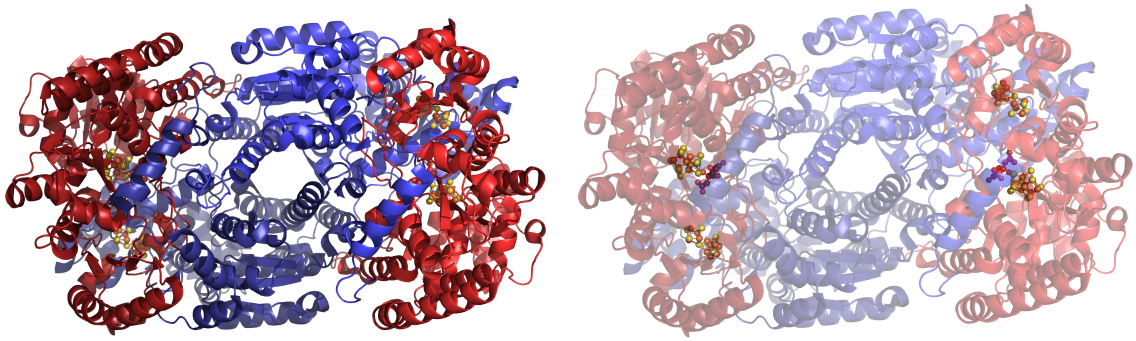

Figure 7: MoFe protein crystal structure modeled in cartoon, at right it is shown in transparency to highlight the location of the metalloclusters (from PDB: 3U7Q)

The MoFe protein is an $\alpha_2\beta_2$ heterotetramer of molecular weight ~230 kDa, with two αβ catalytic units per protein (see figure 7). Within each αβ catalytic unit, there is a single P-cluster and FeMo-cofactor [27-29]. The P-cluster lies at the interface between the α- and β-subunits, approximately 10 Å from the surface, and approximately 14 Å from the FeMo-cofactor, located in the α-subunit [27]. The α- and β- subunits have similar secondary structures consisting of three domains, but show minimal sequence homology [27]. The three domains composing each subunit form a cleft at the center, and in the α-subunit, this is the site where the FeMo-cofactor resides [27]. The αβ-subunit pair has extensive contacts between the subunits, especially in the region surrounding the P-cluster (see figure 8).

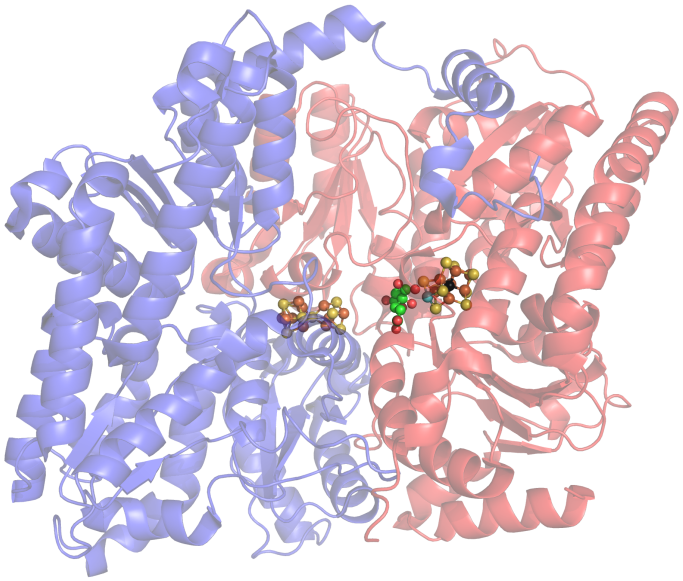

Figure 8: The αβ-subunit pair as seen from the MoFe-protein two-fold axis relating the α- and β- subunits. The α-subunit is shown in red, and the FeMo-cofactor can be seen sitting near the center of the α-subunit. The β-subunit is shown in blue. The P-cluster can be seen sitting at the interface between the two subunits. (from PDB: 3U7Q)

P-Cluster

The P-cluster is a complex [8Fe:7S] metal center, with redox properties capable of regulating multiple electron transfer reactions to reduce the FeMo-cofactor during catalysis. The P-cluster likely acts at an electron "gatekeeper" between the [4Fe:4S] of the Fe protein and the FeMo-cofactor, and ensures that electron flow is one-directional [30-33].

In the as-isolated, dithionite reduced state, the P-cluster is in an all-ferrous diamagnetic state, P^N, but it can achieve multiple oxidation states. In [33], the P^{2+}/P^{1+} redox couple was characterized to involve a proton coupled e^- transfer at physiological pH, whereas the P^{1+}/P^N redox couple does not involve a coupled proton transfer. Additionally, they measured the midpoint potential of these two redox pairs, identifying the P^{2+}/P^{1+} midpoint potential to be pH dependent and ranging between -224 mV at pH=6.0 to -348 mV at pH=8.5. The P^{1+}/P^N midpoint potential was determined to be -290 mV and non-pH dependent. The spin states of the oxidation states were identified as: P^N S=0, P^{+1} S=3, P^{+2} S=1/2 and S=7/2, and P^{3+} S>2 [34]. The P^{2+} and P^N states additionally have been proposed to display different structural conformations (see figure 9).

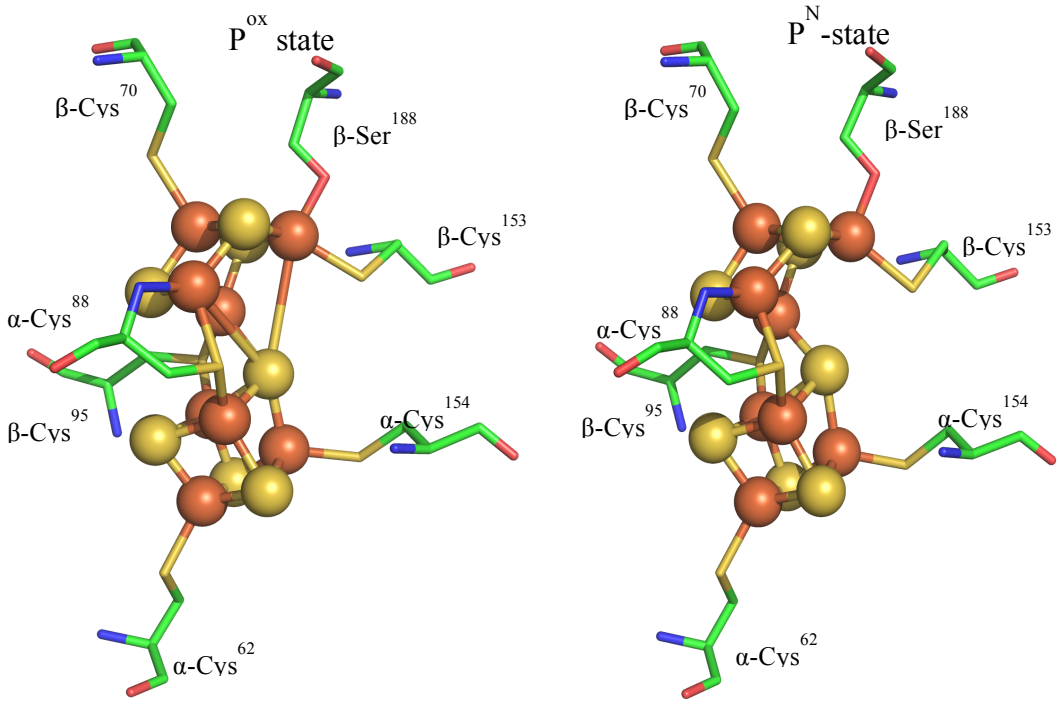

Figure 9: Putative Oxidation-state P-Cluster conformational changes. At left is the P^{ox} 2+ oxidized structure (from PDB: 2MIN), at right is the P^{N} all-ferrous structure (from PDB 3U7Q).

FeMo-cofactor

The FeMo-cofactor is the most elaborate metal-cofactor known in biology. It is an approximately three-fold symmetric [7Fe:9S:C:Mo]-*R*-homocitrate cluster. The central 6 iron atoms form a trigonal-prism with one iron and one molybdenum at the peak of the two prisms. Each metal atom is coordinated by three sulfides, and the entire cluster is coordinated to the protein by two ligands in the α-subunit: α-Cys275 at Fe1 and α-His442, with the *R*-homocitrate moiety, at the Mo (see figure 10).

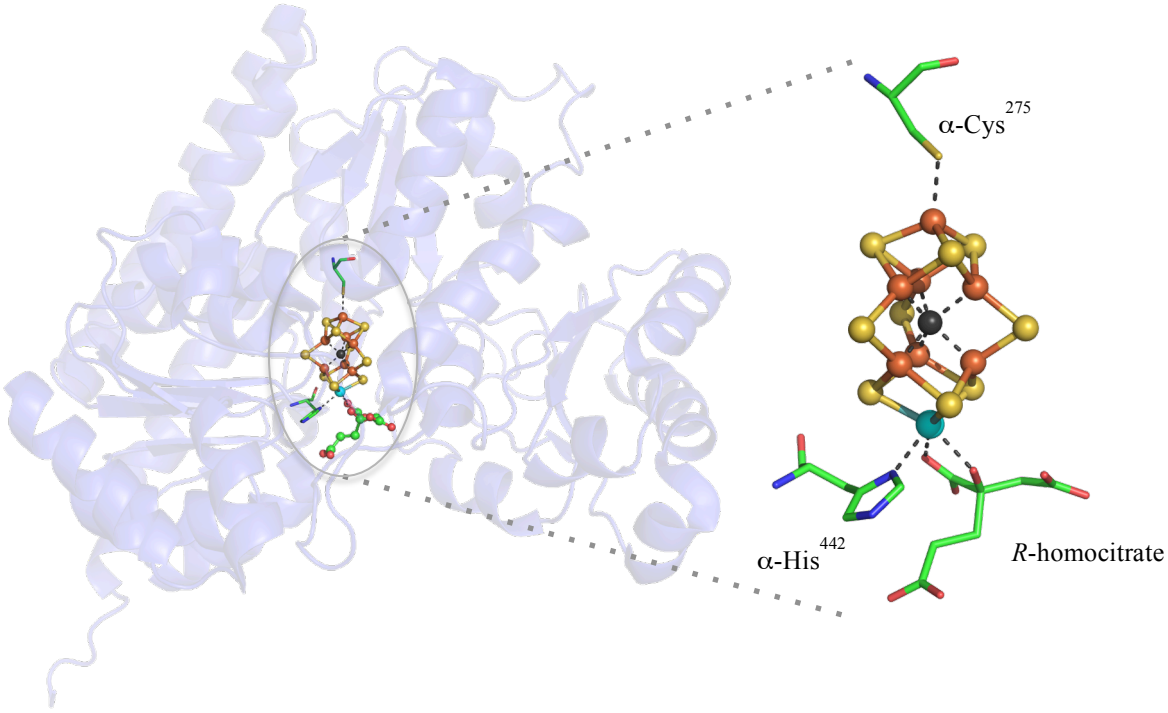

Figure 10: FeMo-cofactor. At left the position of the FeMo-cofactor at a cleft in the α-subunit (colored in blue) of the MoFe-protein. At right, a view of the FeMo-cofactor with the coordinating residues α-Cys275 and α-His442, and the R-homocitrate moiety. Color scheme is as follows: Fe atoms are orange, S atoms are yellow, Mo atom is cyan, the interstitial carbide is dark grey, all other carbons are green, oxygens are red, and nitrogen is blue.

The first structural characterization of Av1 at 2.72 Å, by Kim and Rees in 1992 [35], determined that the FeMo-cofactor is an iron-sulfur-molybdenum metal cluster, with a composition of [7Fe:9S:Mo]. Then, in 2002, Einsle et al. [36] published a much higher

resolution Av1 structure at 1.16 Å, revealing that the FeMo-cofactor contained a central atom, sitting within the metal cluster. The identity of the central atom was not determined, but analysis showed consistency with a light element, C, N, or O. Following the identification of a light atom present in the FeMo-cofactor, in 2011 Spatzal et al. [37] characterized an atomic-resolution structure of Av1 at 1.0 Å, thereby providing significant improvement in the data to allow for integration of the sphere radius to identify the central atom as C. Spatzal et al. complimented the atomic resolution crystallographic data with ESEEM data of uniformly-isotopically labeled Av1 (^{13}C, ^{15}N), demonstrating unequivocally that the identity of the central atom was indeed carbon. Also in 2011, Lancaster et al [38] published a paper in which they also identified the central atom as a carbon using X-ray emission spectroscopy. In 2012, Wiig et al [39] showed that the interstitial carbon originates from a methyl group of S-adenosylmethionine (SAM), inserted into a FeMo-cofactor precursor, by a maturation protein, *nifB*.

Many efforts have been made to identify the electronic and magnetic properties of the FeMo-cofactor. Analysis of the electronic and magnetic properties of the FeMo-cofactor has focused on the as-isolated, dithionite-reduced, state. The as-isolated FeMo-cofactor, $FeMoco^{N}$, reduced by the presence of dithionite, has an S=3/2 spin state, and has been analyzed using a variety of spectroscopic methods including Mössbauer, EPR, XANES, ENDOR, and EXAFS [40-44]. Several oxidation state assignments have been made for the metals in the $FeMoco^{N}$ in the S=3/2 spin state: $2Fe^{II}5Fe^{III}Mo^{IV}$ over $4Fe^{II}3Fe^{III}Mo^{IV}$ to $6Fe^{II}1Fe^{III}Mo^{IV}$ [44-49]. A study in 2014 identified the Mo to be a Mo^{III}, requiring that the oxidation states be reconsidered [49], such as in [50] in which the likely oxidation state identified was $3Fe^{II}4Fe^{III}Mo^{III}$.

In addition to the $FeMoco^{N}$ state, other states have been also been characterized, namely, $FeMoco^{R}$ and $FeMoco^{ox}$ [34, 41, 46]. The $FeMoco^{R}$ state is the 1 e- reduced state, which was freeze trapped under turnover conditions (the Fe protein is the only physiological reductant). The $FeMoco^{R}$ state has been heavily analyzed using EPR and ENDOR [51-54],

exhibiting spin states $S \geq 1$ [41, 46, 55]. The likelihood of freeze quenching a single electronic state within a mixture seems unlikely, making these samples most assuredly a mixture of states. Due to difficulty in reducing the FeMo-cofactor, and the action by the P-cluster as a electron shuttle between the [Fe4:S4] and FeMo-cofactor, the redox potential of the $FeMoco^{R}$-$FeMoco^{N}$ pair is unknown. In addition to $FeMoco^{R}$, a 1 e- oxidized state, $FeMoco^{ox}$, has also been characterized. The $FeMoco^{ox}$ state has S = 0 spin state, and the $FeMoco^{N}$- $FeMoco^{ox}$ pair has a redox potential of -42 mV [56, 57]. The $FeMoco^{ox}$ state may not have a physiological role, but it provides more details regarding the complex redox and electronic states of the FeMo-cofactor.

CO was first identified by Lind and Wilson [58] as a potent and specific inhibitor of nitrogenase activity. Since then, many studies have characterized various aspects of substrate and inhibitor binding to the FeMo-cofactor. CO-binding to the cofactor has been of especial interest since CO is isoelectronic to N_2 and serves as a strong reversible inhibitor of nitrogenase activity, excluding proton reduction [59, 60]. EPR techniques and FTIR have been popular techniques applied to the analysis of CO binding in nitrogenase. The identification of the "lo-CO" and "hi-CO" signals [61] have led to many spectroscopic characterizations of these states, along with modeling to identify where the CO was bound [62-67] . These studies produced multiple proposed binding states, and resulted in analyses that concluded that the "lo-CO" state represented a single CO bound at the "waist" of the FeMo-cofactor possibly in a bridging manner, and the "hi-CO" state represented two CO terminally bound [64, 66]. Unfortunately, without either the possibility of spatially characterizing the binding of CO, nor the ability to identify if multiple species were present in a sample, determination of exactly how and where the CO were bound has not been possible. In 2012, a study used extended x-ray absorption spectroscopy (EXAFS) and nuclear resonance vibrational spectroscopy (NRVS) to study binding of propargyl alcohol to the FeMo-cofactor and determined that the substrate was binding at an iron, not molybdenum, and that a μ-2 Fe-S-Fe bond was broken in the process [67]. Also in 2014, a study combining NRVS, EXAFS, and density functional theory (DFT) looked at binding of CO to the FeMo-cofactor and the role of the interstitial

carbon [68]. In this study, the authors concluded that the 6-Fe core of the FeMo-cofactor is distorted upon CO binding, and the interstitial carbon acts to modulate the chemical reactivity of atoms within the metallocluster. Unfortunately, without the possibility of spatially characterizing the binding of CO, or the ability to identify if multiple species were present in a sample, determination of exactly how and where the CO were bound was not possible.

Previous data have revealed unexpected structural rearrangement in the cofactor, building on the intrinsic complexity of this two-protein, three-metal cluster, ATP-dependent process. Understanding the structural, electronic configuration, and redox activity of the enigmatic FeMo-cofactor and its mechanism are difficult but important tasks.

The Lowe-Thorneley Model

The Lowe-Thorneley model (LT-model) is a kinetic description of the catalytic cycle for nitrogenase based upon a series of stop-flow and rapid-quenched spectrophotometry kinetic experiments. In this model, the Fe-protein and the MoFe-protein undergo a series of interactions involving ATP-hydrolysis coupled electron transfer, with proton transfer also occurring during catalysis [69-73]. The stoichiometric equation for nitrogen fixation is considered in this model, with $2NH_3$ and one H_2 produced per N_2 reduced. The requirement for 8 e^- requires multiple electron transfer events from the Fe-protein, thereby requiring multiple Fe-MoFe-protein binding and dissociation events [74]. Here, in figure 11, the LT model is simplified, and shown in two parts, the Fe-protein cycle and the MoFe protein cycle. In the Fe-protein cycle, the Fe-protein goes through several states: a reduced state from reduction by endogenous ferredoxin (Fd) or flavodoxin (Fld), a reduced ATP bound state, binding with the MoFe-protein followed by electron transfer, followed by dissociation producing an oxidized ADP-bound state. The MoFe-protein cycle is coupled to the Fe-protein cycle through the ATP-hydrolysis coupled electron transfer from the [4Fe:4S] cluster to the MoFe-protein. The MoFe-protein is modeled as going through eight states (E^0-E^7) in which it is reduced by an electron (from the Fe-protein) each time, with protons coupled reactions [41]. In the LT model, N_2 binds at the E^3 or E^4 reduced state, and

NH_3 is produced subsequently in the more reduced states, from E^5 on (see figure 11) [41, 75].

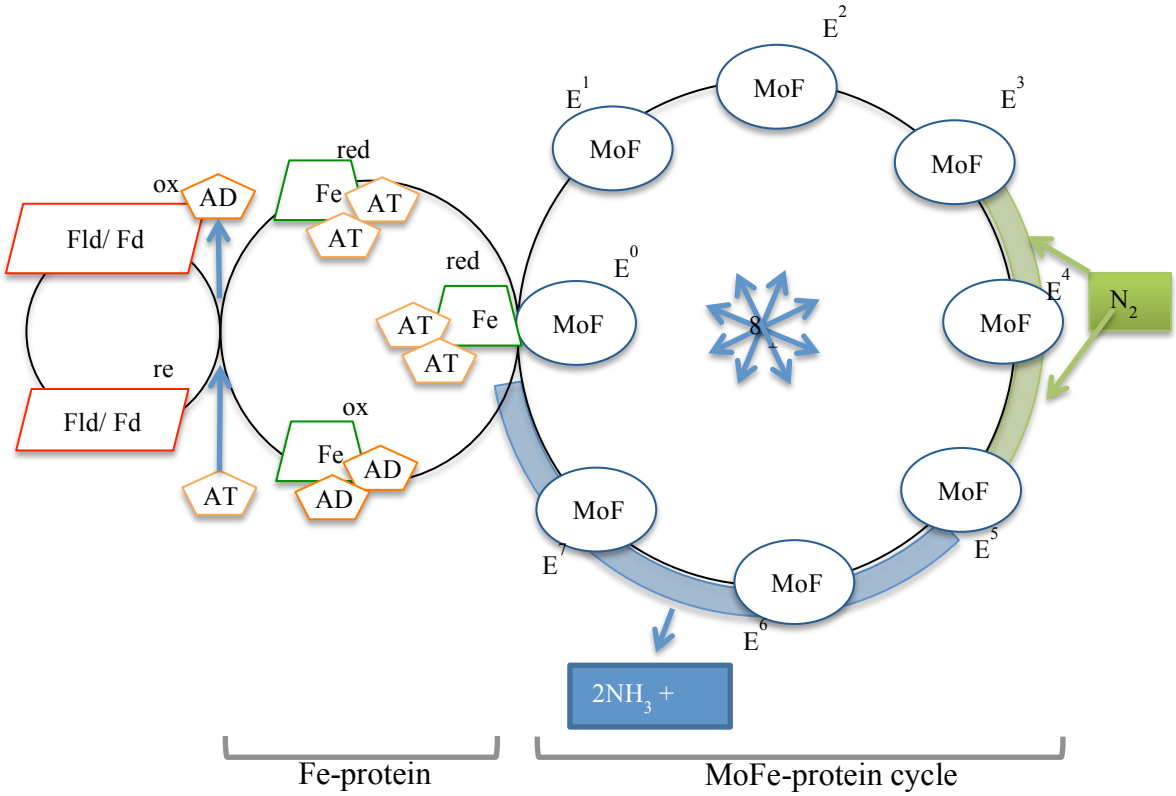

Figure 11: The Nitrogenase cycle without proton binding and hydrogen release states
The Nitrogenase cycle can be broken down into two coupled parts, the Fe-protein cycle, and the MoFe-protein cycle. In the Fe-protein cycle, the Fe-protein is reduced by ferredoxins (Fd) or flavodoxins (Fld), and binds two ATP, which are hydrolyzed and an electron is transferred to the MoFe-protein. In the MoFe-protein cycle, the MoFe-protein is reduced by eight electrons, taking it through eight different states (E^0-E^7), during which it reduces N_2. The likely parts of the cycle for N_2 to bind (E^3-E^4) are highlighted in green, and the likely parts for NH_3 release are highlighted in blue. This figure is based upon figures in [2, 76]

A full characterization of the nitrogenase cycle will require that the electronic and magnetic properties of the metal centers be characterized, and the binding mode of substrates, along with intermediates and inhibitors, be determined.

X-ray Crystallography

X-ray crystallography is a light scattering (diffraction) technique in which elastic scattering of light (with a wavelength in the x-ray region) produces "reflections" that are detected and used to determine the structure of the material analyzed.

Light in the x-ray region of the electromagnetic spectrum is ideal for determining structures because the wavelength of x-rays is comparable to the distances between atoms. For instance, most interatomic distances for covalently bonded atoms are in the 10^{-10} m (Ångstrom) range (for instance, a C-H covalent bond is approximately 1Å and a C-C single bond is approximately 1.5Å) making the interaction of light at these wavelengths optimal for studying structures.

Crystals are periodic structures composed of repeating units in a 3-D lattice. A crystal can diffract incoming radiation in a regular manner when Bragg's Law is satisfied (see below). Crystals give sample density and periodicity to effectively amplify the signal through the reflections created from the lattice structure.

Protein Crystallization

Crystallization is a phase dependent process, by which crystals are formed when supersaturation is achieved dependent upon optimized parameters, including concentration, pH, temperature, and various other parameters [77, 78] (see figure I). The three stages of crystallization growth are nucleation, crystal growth, and cessation of growth [79]. This process is energetically favorable because as the proteins nucleate and crystallize, they shed part of their hydration shell, increasing the overall entropy and therefore a more negative free energy [2, 80]. There are various methods for achieving supersaturation such as microbatch, vapor diffusion, dialysis, and free interface diffusion (see figure 12) [77].

In practice, protein crystallization is achieved based upon crystallization screens during which a wide variety of crystallization conditions, protein concentrations, methods, and temperatures are tested. Crystal growth depends on many factors such as sample

concentration, temperature, pH, precipitants chosen, buffer, additives, detergents, and various other parameters [79].

Figure 12: Schematic illustration of protein crystallization phase diagram. Crystals are formed in the supersaturation zone when the protein concentration is above the solubility curve. Crystallization methods are represented: a) microbatch, b) vapor diffusion, c) dialysis, d) free-interface diffusion. This figure was prepared based upon figure 1 of [77]

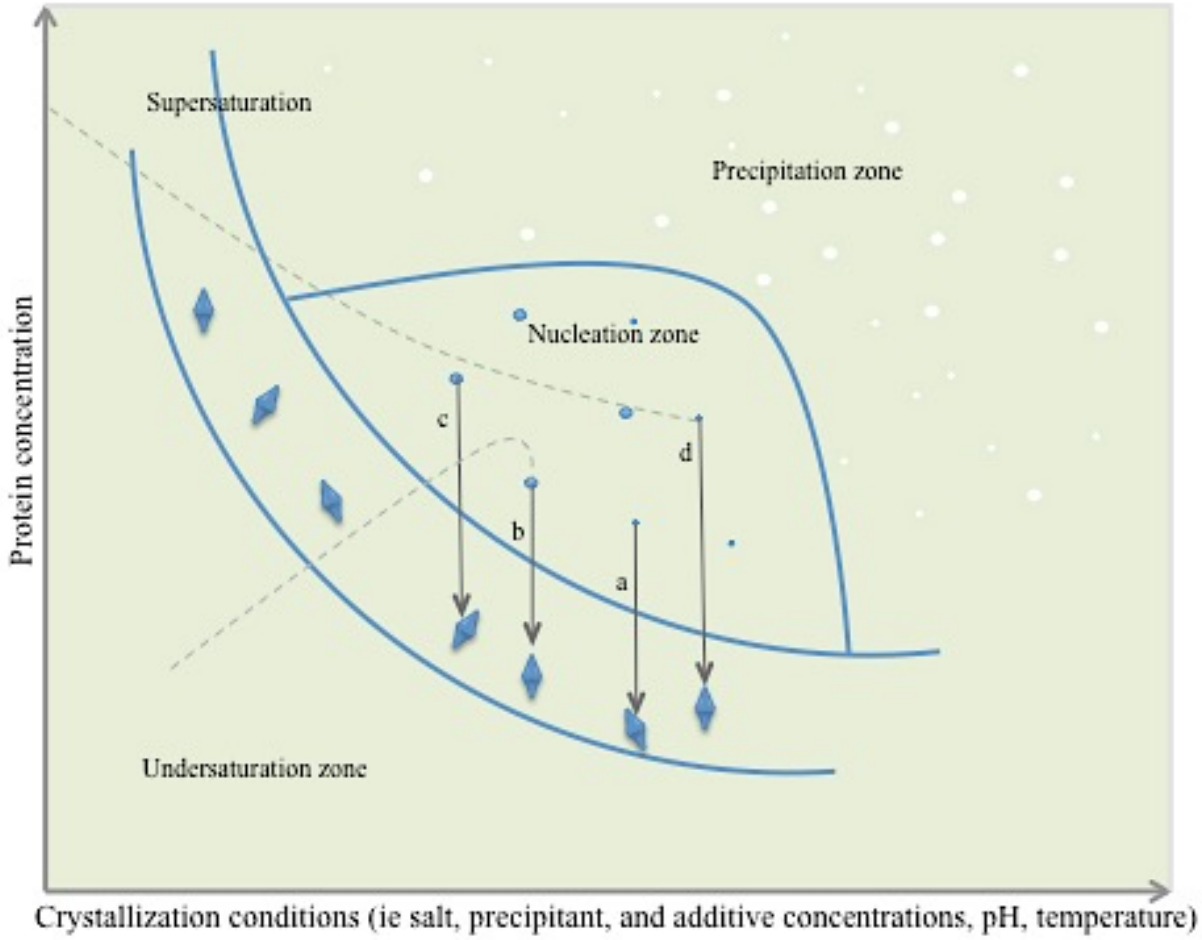

Bragg's Law

Bragg's law gives a mathematical description of the interaction of coherent light with material in a lattice that is spaced in a way to give optimal constructive interference of light dependent upon the angle of incidence of the incoming light (see figure 13) [81].

Bragg's law is: $n\lambda = 2d \sin\theta$

n is a positive integer

λ is the wavelength of incoming radiation

d is the lattice space distance

and θ is the angle between the lattice and the incoming light

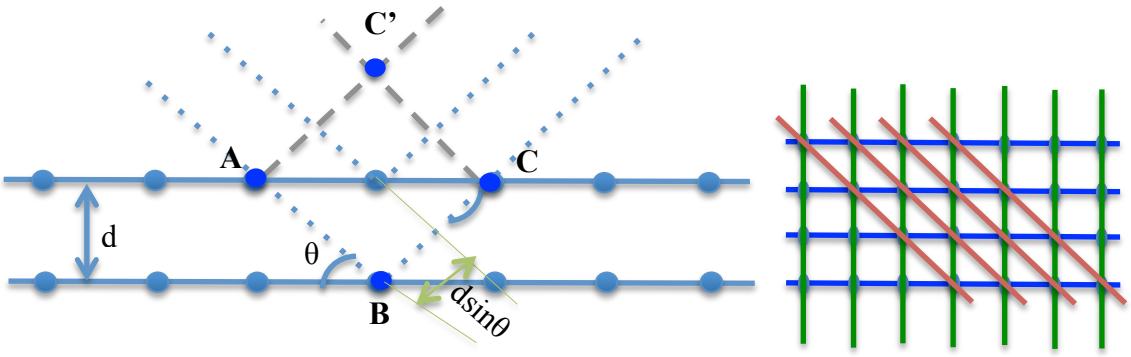

Figure 13: Scattering of X-rays in a lattice with d-spacing
At left is a schematic demonstrating Bragg's law, with the incoming beams scattering and only providing positive interference if they obey Bragg's law. At right is a drawing of a lattice with three d-spacing options highlighted.

Ewald's Sphere and Reciprocal space

Due to the nature of light diffraction, the diffraction pattern produced is not representative of real space, but represents "reciprocal space". Ewald's sphere is employed in this analysis. Ewald's sphere is a geometric construct that relates the wavevector of the incoming and refracted light, the diffraction angle of the refracted light, and the reciprocal lattice of the crystal.

An Ewald's construction can be used to relate the planes in a crystal lattice to the reflections present in a diffraction pattern (see figure 14). By combining Bragg's law and

the Ewald construction, we can determine the position for reflection spots on a detector if we know the cell dimensions. The diffraction pattern (without consideration of spot intensities) contains information of the unit cell dimensions, and the spot intensities contain information about the distribution and identity of the atoms in the unit cell.

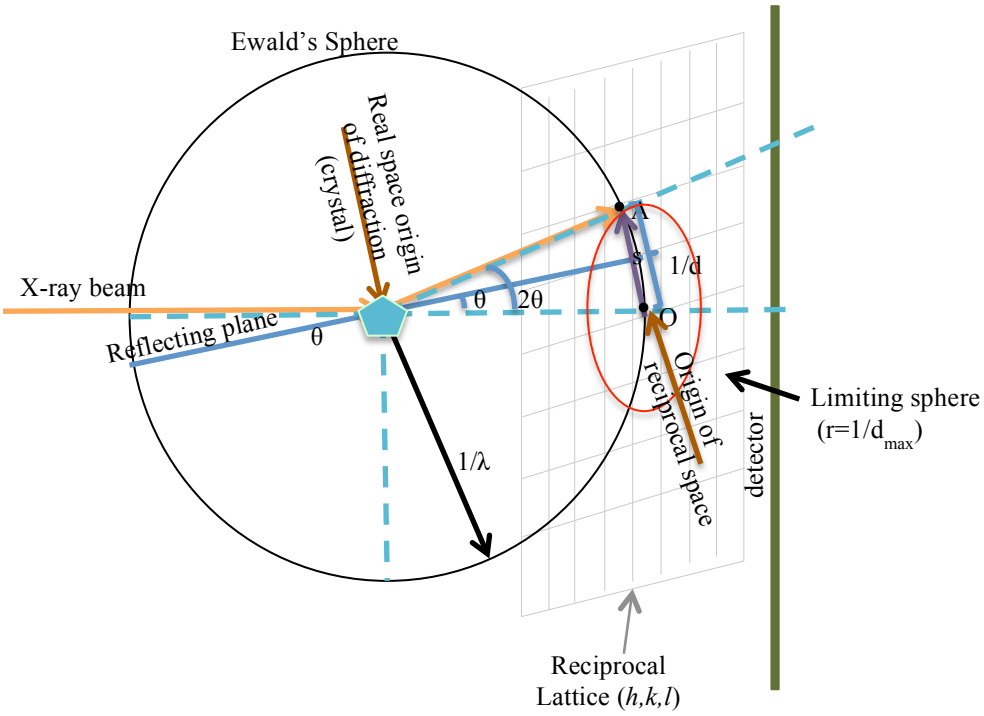

Figure 14: Ewald Construction. Created based upon figure in [82]

By looking at the elements of Ewald's sphere and comparing it to Bragg's law, we can determine that the distance of the reflection from the origin in reciprocal space is equal to:

$$\frac{1}{d} = \frac{2\sin\theta}{\lambda}$$

Considering the elements of Bragg's law in reciprocal space, we can define the vector s has a length of:

$$|s| = 2r\sin\theta$$

with r being the radius of the Ewald's sphere, 1/λ, reflecting the position of spot from higher resolution reflections being farther away from the origin.

Structure Factors, Atomic scattering factors, and Electron density

The structure factor is a mathematical description of the amplitude and phase of light scattering. It provides a description of how the atomic arrangement in a crystal will influence the intensity of the scattered x-ray beam [81, 83]. The structure factor can be written:

$$F_{hkl} = |F_{hkl}|e^{i\varphi_{hkl}}$$

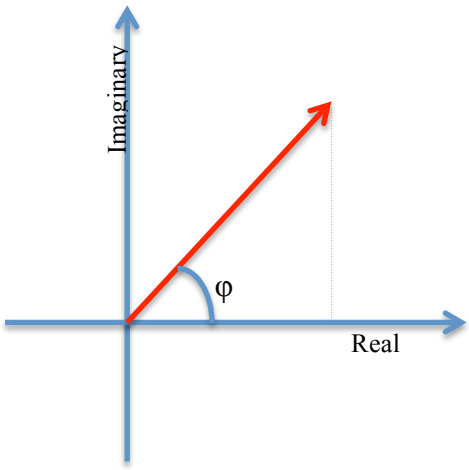

for which the first term, $|F_{hkl}|$, represents the amplitude and the second term, $e^{i\varphi_{hkl}}$, represents the phase of the reflection.

The intensity of spots is dependendt upon the contents (electron density) of the unit cell, and proportional to the square of the amplitude:

$$I \propto |F_{hkl}|^2$$

Using the Argand diagram (left), the structure can be represented as a vector plotted on axes representing the real and imaginary components [84].

The structure factor can also be written as the sum of all electron density in the unit cell:

$$F_{hkl} = V \iiint \rho_{xyz}\, e^{2\pi i(hx+ky+lz)} dxdydz$$

This representation considers the electron density over the whole cell unit without accounting for distinct atoms and their individual scattering.

In order to consider individual atoms, the structure factor can be written as a sum of all N atoms in the unit cell, including angle dependent scattering amplitudes (i.e., atomic scattering factors:

$$F_{hkl} = \sum_{i}^{N} f_i\, e^{2\pi i(hx_i+ky_i+lz_i)} e^{-B_i \frac{\sin^2\theta}{\lambda}}$$

f_i represents the atomic scattering factor for each atom in the unit cell

B_i represents the Debye-Waller factor (also referred to as the "B-factor" or "temperature factor") which considers attenuation of x-ray scattering caused by thermal motion [84].

The Fourier transform of the structure factor defines the electron density:

$$\rho_{x,y,z} = \frac{1}{V} \sum_{h=-\infty}^{\infty} \sum_{k} \sum_{l} F_{h,k,l}\, e^{-2\pi i(hx+ky+lz)}$$

The phase problem

In crystallography, the diffraction pattern contains information about the unit cell and the distribution of atoms in the unit cell.

Each spot in a diffraction pattern corresponds to a point in the reciprocal lattice, and represents a wave with amplitude and a phase. Unfortunately, the spots in a diffraction pattern only have a position and intensity, but do not include the phase information, and so much information regarding the structure is lost through the experiment.

In order to overcome this problem, several methods are commonly employed; molecular replacement (MR), multi-wavelength anomalous dispersion (MAD), and single-wavelength anomalous dispersion (SAD).

Anomalous Scattering

Anomalous scattering is the scattering of light at an absorption edge. The amount of energy absorbed by an atom is dependent upon its atomic number, and thus heavy atoms display easily detectable anomalous scattering near their absorption edge (see figure 16 for examples) [85].

The total scattering factor of an atom is:

$$f(\lambda) = f^0 + f'(\lambda) + if''(\lambda)$$

The normal scattering factor, f^0, is independent of wavelength and provides "normal" diffraction. The anomalous scattering factors, f' and f'', are the real and imaginary parts of the scattering factor, and are wavelength dependent. The $f^0 + f'$ term represents real, dispersive scattering, and the f'' term of the scattering factor represent imaginary, absorptive scattering. [81, 84]

X-ray photons interact with the electrons of atoms, and produce an oscillation of the electrons, resulting in the emission of radiation with the same frequency as the incident beam. Coherent scattering, the basis for normal diffraction experiments, produces a set of reflections from the lattice planes. The intensities of reflections from the h,k,l lattice plane are identical to those of -h, -k, -l, resulting in the structure factors having identical amplitudes, with opposite phase angles. This relationship is described in Friedel's law:

$$|F(h,k,l)| = |F(-h,-k,-l)|$$

Friedel's law can be broken when the incident X-ray beam is close to the absorption edge of an atom in the structure. Interaction at the absorption edge causes a phase shift of the emitted radiation, breaking the phase relationship between the incident and emitted radiation. Energies near the radiation edge produce anomalous scattering as a significant part of the total scattering. This produces an atomic scattering factor that is composed of a real, dispersive term ($f^0 + f'(\lambda)$) and an imaginary, absorptive term ($if''(\lambda)$). As a result, Friedel's law is broken, and the scattering pairs contain an anomalous difference, $\Delta_{anomalous}$:

$$\Delta_{anomalous} = |F(h,k,l)| - |F(-h,-k,-l)|$$

This is demonstrated in figure 15.

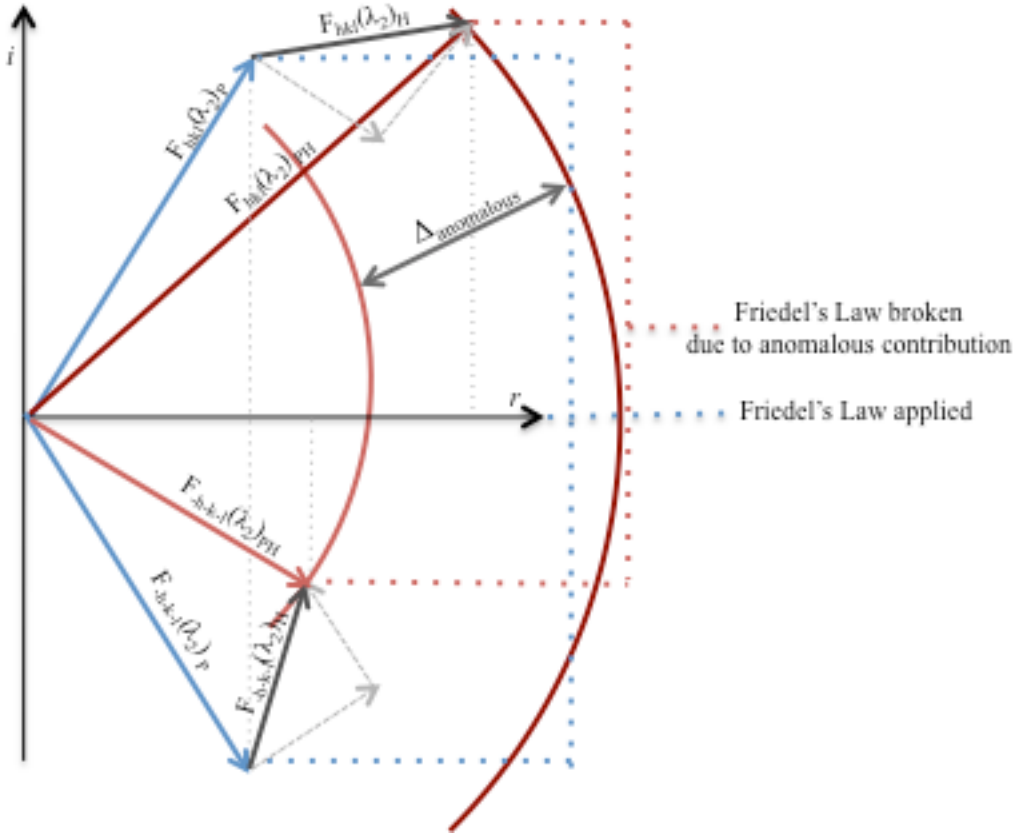

Figure 15: Friedel's Law. The Symmetry of Friedel's pairs for wavelength independent scattering (f^0) is shown in blue (i.e. for a protein containing no heavy atoms). Anomalous contribution to the scattering from a heavy atom is shown in red (darker red for $|F(h,k,l)|$ and lighter red for $|F(-h,-k,-l)|$) with the heavy atom component for anomalous scattering shown in black (in dashed grey arrows are the f^0+f' and f'' contributions from the heavy atom scattering, notice the +90° phase difference between these two components). $\Delta_{anomalous}$ is shown as the difference between the red and dark red curves demonstrating the difference in the magnitudes of the vectors.

The anomalous scattering factors, f' and f'', are the wavelength-dependent real and imaginary parts of the scattering correction. The *i* preceding *f"* is indicative of there being a +90 degree phase shift between *f"* and the real component of *f*. Their relationship is described in the Kramers-Kronig relationship:

$$f'(\lambda) = \frac{2}{\pi}\int_0^\infty \frac{\lambda' f''(\lambda')}{(\lambda^2 - \lambda'^2)}\, d\lambda'$$

The f'' portion of the scattering factor can be determined experimentally using fluorescence or absorbance measurements (theoretical measurements are available, but during experimentation, measurements must be taken to consider the protein environment),

and *f'* can then be determined through application of the Kramers-Kronig relationship. (see figure 16 and table 1 for *f'* and *f''* for Se, S, Fe, Mo)

Anomalous scattering of light atoms, such as C, N, or O, is not analyzed using x-ray crystallography because the energies required are not attainable within the energy range accessible, and thus experimental anomalous scattering is done with heavy atoms (i.e. Se, Fe, Mo, Hg, etc.). Anomalous scattering by heavy atoms in crystal samples is the basis for Multiple Anomalous Diffraction (MAD) and Single Anomalous Diffraction (SAD) experiments for phasing to determine unknown structures.

Analysis of anomalous scattering data collected for a protein crystal structure allows for determination of the phase angles for the heavy atoms in the sample. By using this information, the "substructure" of the heavy atoms can be used to determine the phasing of the entire protein structure [2]. This phasing is applied in MAD and SAD experiments. MAD employs, as indicated by the name, multiple wavelengths for collecting data, including data collected at the absorption edge of a heavy atom, whereas with SAD, a single wavelength at the absorption edge is used for phasing. This technique requires the presence of heavy atoms, which may include natural sites (as found in metalloenzymes), soaking/co-crystallization in a solution including heavy atoms, or incorporation of a heavy atom (for instance by introducing mutations within the protein to incorporate selenocysteine or selenomethionine).

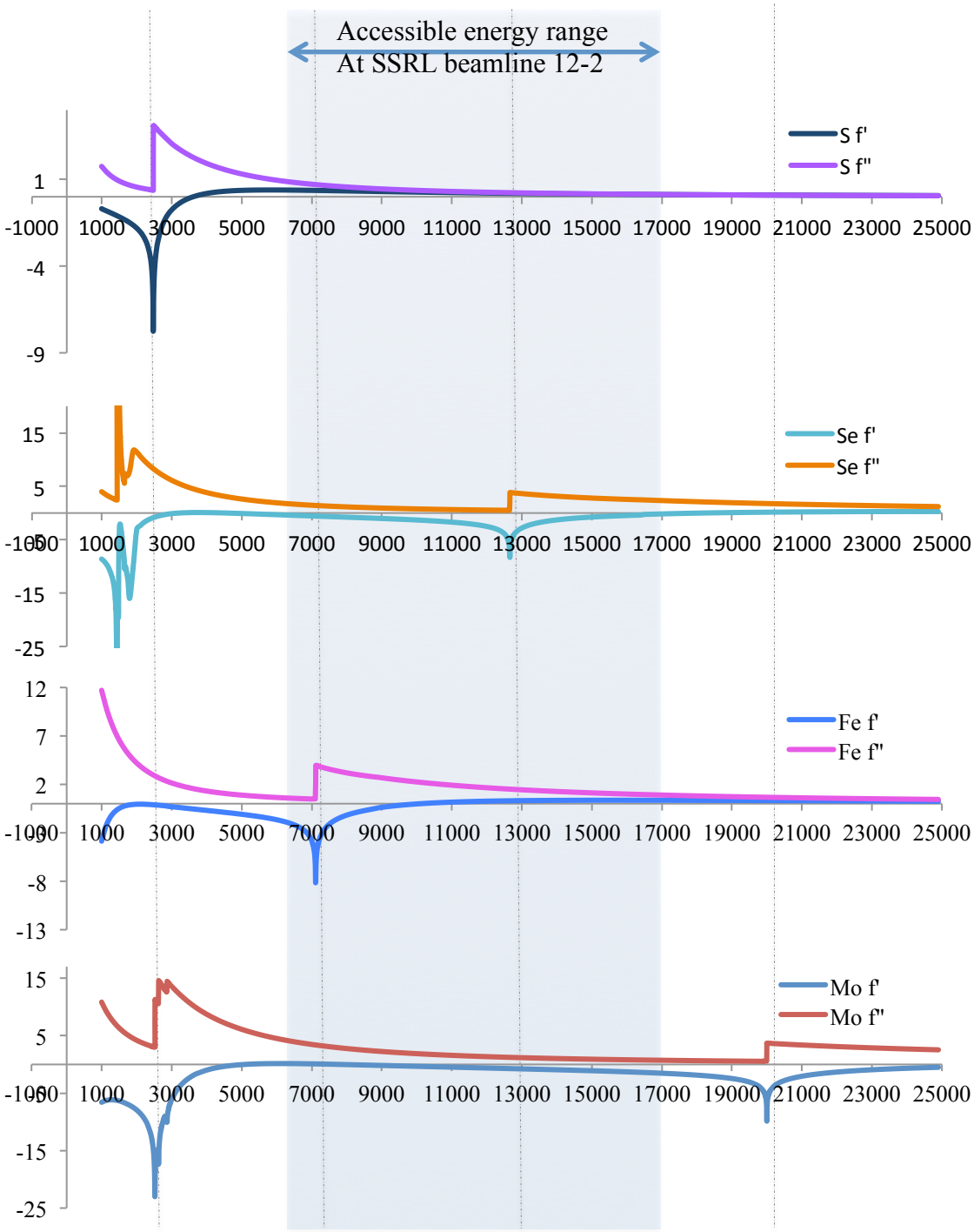

Figure 16: *f'* and *f"* values for S, Se, Fe, Mo (top to bottom) plotted vs energy (eV) from 1000 to 25000. In grey is the accessible energy range at the SSRL beamline 12-2. The values of f' and f" used in this figure are theoretical values, and are from [86]

Table 1: X-ray absorption edges for Se, S, Fe, and Mo.
1a: lists the edge name, the keV corresponding to the absorption edge, and the Å equivalent to the energy
1b: lists the *f''* contribution for each element, Se, S, Fe, and Mo at the absorption edge for each of the corresponding elements.
All values in tables 17a and 17b are from [86]

1a

X-ray Absorption edges *			
element	edge	keV	Å
Se	K-edge	12.6578	0.9795
S	K-edge	2.4720	5.0155
Fe	K-edge	7.1120	1.7433
Mo	K-edge	19.9995	0.6199
	L-I edge	2.8655	4.3268

*All absorption edges listed are theoretical, and do not take into consideration molecular environments that may alter experimental values

1b

f″ contribution, e^-				
	Se K-edge	S K-edge	Fe K-edge	Mo K-edge
element	12567.8 eV	2472 eV	7112 eV	19999.5 eV
Se	**3.8464 (12660)**	8.1604 (2500)	1.3868 (7200)	1.7753 (20000)
S	0.2333 (12700)	**4.1043** (2475)	0.6853 (7200)	0.0944 (20000)
Fe	1.4915 (12700)	2.9072 (2500)	**3.9501** (7115)	0.6613 (20000)
Mo	1.2256 (12700)	3.0643 (2473)	3.3166 (7200)	**3.6976** (20000)
*in parentheses are the actual energies for these *f″* values values are from: [86]				

In addition to providing data for phasing, due to the characteristic *f''* signal, anomalous maps can also be used to quantify occupancies of heavy atoms if a fixed signal (i.e. internal standard) is available in the protein. In the MoFe-protein, there are 32 Fe atoms which all have an occupancy of 1 (assuming 100% occupancy of the metalloclusters) due to the FeS-clusters present (the P-cluster [8Fe:7S], the FeMo-cofactor [7Fe:9S:Mo:C], and Fe16). Replacement of a sulfur in the FeMo-cofactor with a selenium can then be analyzed to identify the efficiency of replacement of the sulfur by selenium using the anomalous signal produced by the Se, and applying the Fe *f''* contribution and the S *f''* contribution at this energy as internal standards (see table 1a and 1b for these values). B-factors must be taken into consideration as well as sphere radius of integration for these calculations [2, 37].

Molecular replacement (MR) is another method for determining the phases for a structure. It uses the phases from a previously determined, homologous structure and applies them to the diffraction data collected. MR compares a determined structure with an experimentally-determined Paterson map, an interatomic vector map produced by squaring the structure factor amplitudes while setting the phases to zero [87]. The Patterson function, P(x), is a Fourier transform of the intensities, setting all phases to zero, and may be expressed as:

$$P(x) = \frac{1}{V}\sum_{h} |F(h)|^2 \, e^{-2\pi i h x}$$

Patterson maps for the known and unknown structures then go through a series of rotational and translations functions to match them as closely as possible. Alignment of the two Patterson maps allows for the phase angles from the known structure to be applied to the collected data, providing information for solving the structure. The Patterson function does not describe the positions of atoms in a structure, but rather the vectors between all pairs of atoms. Thus, proteins with similar structures also have similar Patterson maps [2].

EPR and ESEEM theory

Electron Paramagnetic Resonance (EPR)

EPR is dependent upon the interaction of a paramagnetic electron (unpaired) with an applied magnetic field to provide information regarding the chemical environment. The electronic configuration within materials determines their structure and reactivity, and so, employing a technique that provides information regarding the electronic state, and changes to it, is of great use in the study of materials used in chemical reactions.

Biological EPR is an important technique for characterizing metallocenters. EPR can be used to identify the chemical make-up, oxidation state, coordination sphere, atomic distances, and electronic states within these metallocenters.

Electrons have a spin quantum number, s= ½, and a magnetic moment, with magnetic components of m_s= +/- ½. In the presence of an external magnetic field, B_0, the magnetic moment of an electron will align itself parallel (-1/2) or antiparallel (+1/2) to the magnetic field (see Figure 17).

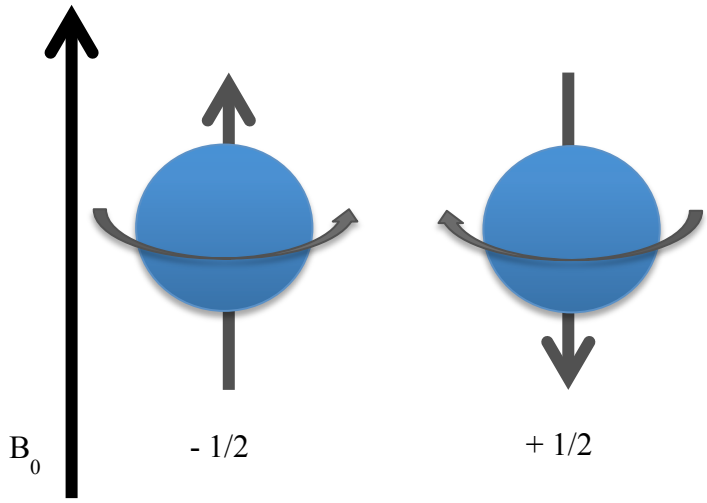

Figure 17: Electron spin magnetic moment alignment with an external magnetic field, B_0. Figure adapted from [3]

The spin Hamiltonian for a single unpaired electron is:

$$H_S = \mu_\beta B_0 \cdot g_e \cdot S$$

Elements of the spin Hamiltonian are: μ_β is the Bohr magneton, B_0 is the strength of the magnetic field, g_e is the Landé g-value for a free electron, and S is the spin quantum number.

The alignment of the magnetic moment with the magnetic field correlates to a specific energy, due to the Zeeman effect (see figure 18) [3, 88]. According to Plank's law, electromagnetic radiation will be absorbed if the energy difference between two states is related to the frequency of the radiation. The resonance condition required for inducing Zeeman splitting is:

$$\Delta E = h\nu = g_e \mu_\beta B_0$$

Where g_e is the electron g-factor (g_e is 2.0023 for a free electron).

The g value is also called the dimensionless magnetic moment, and is a dimensionless value that describes the magnetic moment and gyromagnetic ratio of a particle.

E is the energy, B_0 is the magnetic field strength, h is Planck's constant, and μ_e is the Bohr magneton.

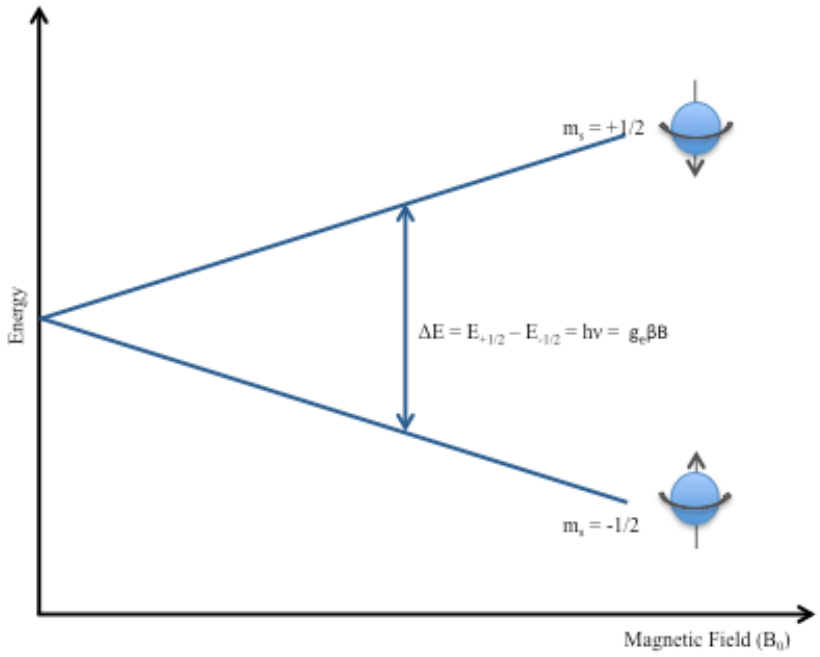

Figure 18: Zeeman splitting occurs due to magnetic field separation of electron spin energies as a function of B_0 Figure adapted from [2, 3]

Absorption of this energy causes a transition in the electron from the lower energy state to the higher one (see figure 18). EPR radiation is in the gigahertz range (microwave radiation).

When an electron interacts with one or more positively charged nuclei (see figure 19), it experiences an internal magnetic field in addition to the applied external magnetic field, B_0. This can be represented as a "shift" in the g-value proportionality constant, expressed as:

$$h\nu = (g_e + \Delta g)\beta B$$

or,

$$h\nu = (g)\beta B$$

where

$$g = (g_e + \Delta g)$$

Δg gives us chemical information about the molecular structure. [89]

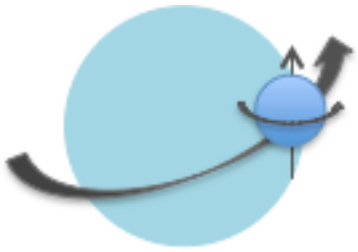

Figure 19: Spin-orbit coupling. When an electron is rotating around a nucleus in a molecule, its total angular momentum results from the addition of orbital angular momentum (*L*) with the intrinsic spin angular momentum (*S*). Figure adapted from [3]

The g-value

The g-value for an electron contains information about the electronic environment. Deviation from the value of a free electron is characteristic of the electron interactions with its environment, e.g. , splitting of the g-value into the principal g-values, g_x, g_y, and g_z, due to anisotropy of the environment, or splitting of the signal from interactions with other electrons and nuclei provides information about the molecular environment in which the unpaired electron resides. Analysis of these changes allows for determination of the magnetic and electronic state of the sample.

The g-value is a tensor, described by a 3 x 3 matrix, that includes three orientational parameters describing the orientation of the paramagnetic center with respect to the magnetic field [88] :

$$\begin{bmatrix} g_{xx} & g_{xy} & g_{xz} \\ g_{yx} & g_{yy} & g_{yz} \\ g_{zx} & g_{zy} & g_{zz} \end{bmatrix}$$

Orbitals are directionally dependent, resulting in anisotropy of the g-value tensor. In oriented samples, such as in single-crystal EPR, the g-factor of the EPR spectrum changes as the sample is rotated due to g-value anisotropy. However, in solution samples, the anisotropy from orbital orientation is averaged out, resulting in the diagonalization of the 3x3 matrix can be due to symmetry of the matrix elements ($g_{xy} = g_{yx}$, $g_{zx} = g_{xz}$, etc.), minimalizing the matrix to the principal g-values:

$$\begin{bmatrix} g_{xx} & & \\ & g_{yy} & \\ & & g_{zz} \end{bmatrix}$$

In non-oriented samples, the principal g-values (from here on written simply as g_x, g_y, and g_z) dominate the spectrum, and reflect the environment of the magnetic moment (see figure 20).

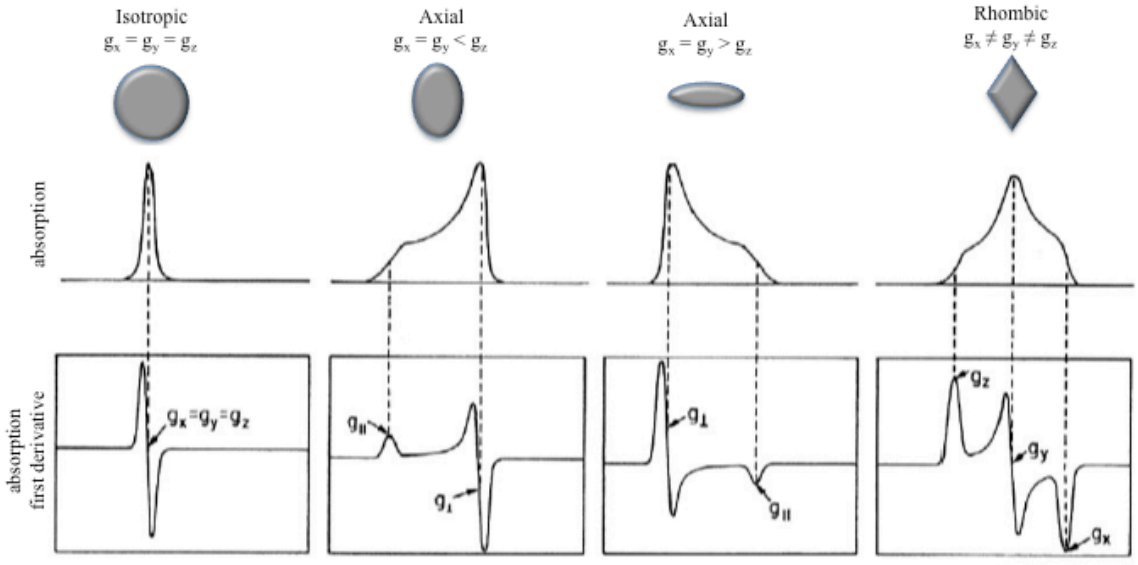

Figure 20: Line Shape and g-value anisotropy. At the top are the different g-tensor shapes, in the middle are the absorption curves for each g-tensor; at the bottom are first derivative spectra for each class g-tensor of anisotropy. Adapted from [3].

Continuous wave EPR (cw-EPR)

In cw-EPR experiments, the frequency is held constant while the magnetic field is varied. EPR energies employed are listed in Table 2, with the most common being X-band (8-12 GHz). Many smaller features are commonly lost in cw-EPR experiments, due to unresolvable, overlapping spectral peaks.

EPR Spectrometer Frequencies	
L band	1-2 GHz
S band	2-4 GHz
C band	4-8 GHz
X band	8-12 GHz
K Band	18-26.5 GHz
Q band	30-50 GHz
U band	40-60 GHz
V band	50-75 GHz
E band	60-90 GHz
W band	75-110 GHz
F band	90-140 GHz
D band	110-170 GHz

Table 2: EPR spectrometer bands and the corresponding frequency ranges.

In practice, features in an EPR spectrum can be complicated due to several common effects [89]:

a) g-anisotropy: the orientation of a non-spherical molecule affects the Zeeman energy, resulting in three principal g-values: g_x, g_y, and g_z (see figure V).
b) zero-field splitting: interactions between the observed and surrounding electrons causes splitting of the signal due to the magnetic field produced by the electrons.
c) hyperfine splitting: interactions between the observed electrons and magnetic nuclei create further splitting of the signal.

Zero-field Splitting

Systems with n unpaired electrons have a spin, $S = n/2$, and systems with more than one electron have spin multiplicity, resulting in a greater number of spin energy levels:

$$M_s = 2S + 1$$

and the spin-Hamiltonian becomes:

$$H_s = \beta B \cdot g \cdot S + S \cdot D \cdot S$$

where D is the zero-field interaction parameter (see figure 21).

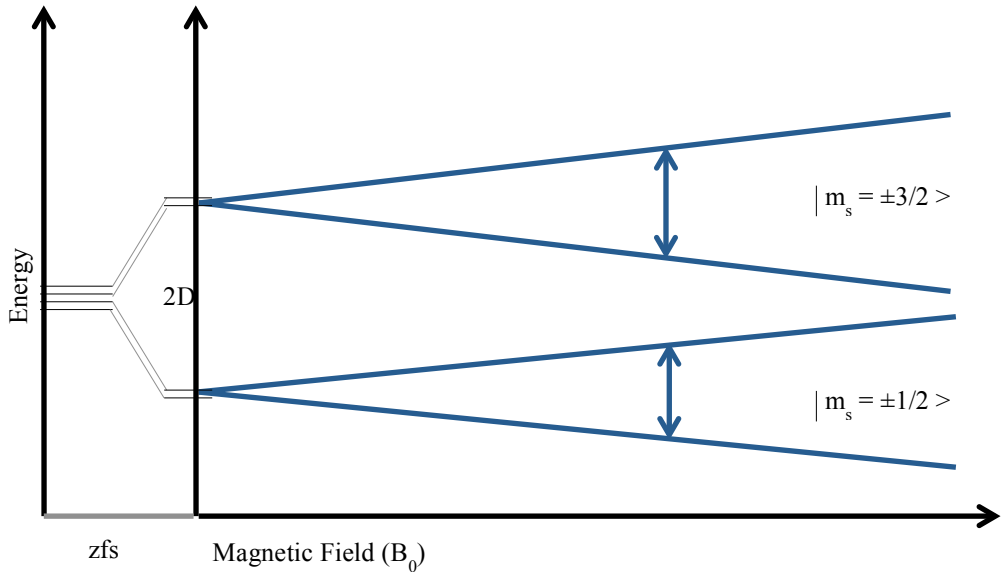

Figure 21: Zero-field Splitting for a 3/2 spin system. This produces two energy levels when there is no external magnetic field, and results in four energy levels in the presence of an external magnetic field, B_0. Figure adapted from [3].

Unpaired electrons in systems with a spin multiplicity S > 1/2 are subject to a magnetic field from electron-electron interactions that results in splitting of the signal equivalent to the value of M_s (i.e., a system with spin 3/2 results in splitting into 4 peaks).The splitting due to electron-electron interactions is called zero-field splitting, because this splitting occurs even in the absence of an external magnetic field.

Spin systems can be broken down into Kramers systems (half-integer systems, S= 1/2, 3/2, 5/2, etc.) and non-Kramer's systems (integer systems, S = 1, 2, 3, etc.) [3] Spectra of Kramer's systems display peaks with distinct splitting, producing doublets of peaks,

although the transitions are of different levels due to EPR selection rules, $\Delta|m_s| = 1$. Each Kramer's pair has a specific *g*-value, and can be described as an effective g-value:

$$h\nu = g^{eff}\beta B$$

The zero-field interaction parameter, *D*, can be anisotropic, having three values, D_x, D_y, D_z, which are not independent, but are related by:

$$D_x{}^2 + D_y{}^2 + D_z{}^2 = 1$$

so the terms can be redefined to produce two independent terms:

$$D = \frac{3D_z}{2}$$

$$E = \frac{D_x - D_y}{2}$$

These terms can then be used to define the rhombicity, η, of the electron distribution due to orbital directionality and shape:

$$\eta = {}^{E}/_{D} \quad (0 \leq \eta \leq {}^{1}/_{3})$$

Non-Kramer's systems are rarely identified in biological systems, and are difficult to detect in X-band radiation because their splitting is often greater than the X-band energy (although higher energy wavebands can be used). Transitions between the doublet energy levels are greater than ±1, making them forbidden, and producing very weak signals. [3]

Hyperfine Splitting

Hyperfine splitting is caused by interaction of the unpaired electron with a magnetic nucleus. This interaction causes a splitting of the g-values, which is anisotropic, as in the case of Zeeman-splitting. The Hamiltonian becomes:

$$H_s = \beta B \cdot g \cdot S + S \cdot S \cdot I$$

and the resonance condition can then be written as:

$$h\nu = g\beta B_0 + hAm_I$$

for which A is the hyperfine coupling constant (in Gauss), and m_I is the magnetic quantum number for the nucleus (there are $2I + 1$ possible values of m_I; this corresponds to the hyperfine splitting of the Zeeman transition into $2I + 1$ lines of equal intensity), see figure 23 for a diagram showing hyperfine splitting in a $m_s = 1/2$ and $m_I = 1/2$ system.

Pulsed EPR

Pulsed EPR techniques focus spectral features using short pulses of microwave radiation while maintaining a constant magnetic field strength. Short pulses of microwave radiation are applied to induce transitions between energy levels, with the magnetic moment eventually returning to the initial state. This behavior is referred to as relaxation, and can be split into two components: spin-lattice relaxation and spin-spin relaxation. Spin-lattice relaxation (T_1) refers to the dissipation of energy from unpaired electrons to the surrounding molecules via vibrational, rotational, or translational energy. Rapid spin-lattice relaxation is essential for maintaining a population difference of the spin-state. Spin-spin relaxation (T_2), or cross relaxation, is the transfer of energy from an electron in a higher energy state to electrons or magnetic nuclei in lower energy states, without transfer to the lattice. The experimental pulse sequence chosen generates a spin echo (shown in figure Y), which shows an exponential decay determined by the spin-lattice and spin-spin relaxation behavior related to the hyperfine interactions of the system of interest. The spin echo intensity is measured as a function of time, and the Fourier transform of the modulated echo provides information about the electron-nuclear coupling [90].

Electron Spin Echo Envelope Modulation (ESEEM)

ESEEM is a commonly used pulsed EPR technique that allows for detection of hyperfine couplings of nuclear-electron spin interactions [3]. Measuring hyperfine interactions can provide detailed information about electron spin density distribution, distances, and angles. These aspects make ESEEM especially useful when studying metal-ligand interactions, such as those occurring in metalloproteins.

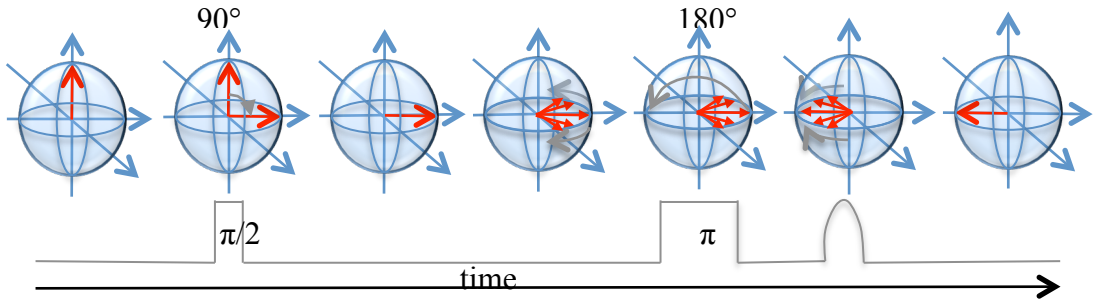

Figure 22: Two-pulse EPR experiment to produce a spin echo. This pulse sequence uses two different pulses, one that is π/2 and causes the magnetic moment to rotate by 90°, followed by a brief relaxation period, and a π pulse that rotates the magnetic moment by 180°. This causes the spin magnetic moment to relax back to the initial state in a focused manner, thus achieving a sharper spectral peak.

Analyzing pulsed EPR data requires that the spin Hamiltonian be expanded:

$$H_S = \beta_e B \cdot g_e \cdot S - \beta_n B \cdot g_n \cdot I + S \cdot A \cdot I + S \cdot D \cdot S$$

where β_e and β_n are the electron and nuclear magnetons, g_e and g_n are the electron and nuclear g-tensors, and A is the anisotropic hyperfine tensor for the electron-nuclear interaction. $\beta_e B \cdot g_e \cdot S$ is the electronic Zeeman interaction, $\beta_n B \cdot g_n \cdot I$ is the nuclear Zeeman interaction, $S \cdot A \cdot I$ is the hyperfine interaction, and $S \cdot D \cdot S$ is the zero-field interaction. The energies can be expressed as:

$$E(m_s m_l) = g_e \beta_e m_s - g_n \beta_n B m_l + h A m_s m_l$$

The modulation effect in ESEEM derives from mixing of allowed and semi-forbidden transitions between the energy levels in an electron-nuclear coupled system, thereby providing detection of weak nuclear-electron couplings (See Figure 23).

Hyperfine Sublevel Correlation (HYCORE) is a two-dimensional ESEEM experiment. By placing the data in two-dimensions, HYSCORE allows for very complicated spectra to become more easily interpreted. [3]

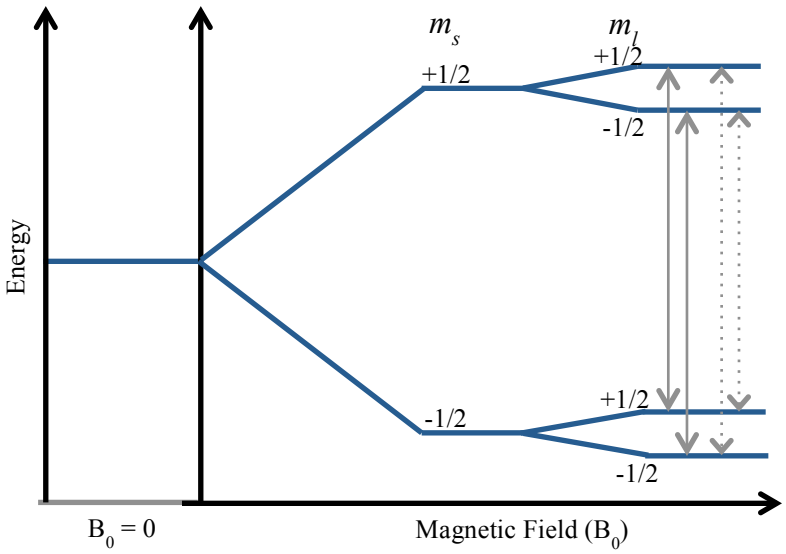

Figure 23: Energy level scheme for a m_s=1/2 and m_l=1/2 system
Solid lines indicate allowed transitions, and dotted lines represent semi-forbidden transitions. The energy difference between the doublets of each electron spin level represent the energy required for pulses that mix the transition levels.
Figure modified from figure 1 of [1]

Focus of this Study

Understanding the mechanism by which the FeMo-cofactor binds to and reduces N_2 requires the characterization of substrate binding modes and intermediates. Due to the transient nature of N_2 binding, characterization of inhibitor bound states is an excellent alternative for identifying binding sites and modes. Nitrogenase has a wide variety of substrates and inhibitors including CO, HCN, SCN^-, and N_3^- [91, 92]. Ligand binding characterization at the FeMo-cofactor has relied mainly upon amino acid mutations in the region near the cofactor to alter substrate reduction properties [93-95].

Spectroscopic characterization of ligand binding requires detailed electronic and magnetic characterization of the FeMo-cofactor, and without these parameters, these experiments are riddled with uncertainty due to the complex electronic state and three-fold-symmetry. Structural characterization is a requirement for identification of the exact location of substrate binding, but the requirement for multiple electron transfer reactions from the Fe-protein to the MoFe-protein makes structural characterization of substrate binding quite challenging.

The goal of this work was to identify how and where ligands bind at the FeMo-cofactor using X-ray crystallography. Sample preparation for accomplishing a ligand-bound state is a difficult hurdle due to the requirement of the Fe-protein and ATP in all conditions to reduce the FeMo-cofactor in order to bind ligands. This required optimization of crystallization conditions for obtaining high quality crystals from activity assay samples and characterization of optimal inhibitor binding for sample preparation.

A second goal of this work was to characterize the FeMo-cofactor after alteration due to site-specific labeling with selenium, replacing a single belt-sulfur. EPR and ESEEM were chosen for this analysis because of the possibility to identify spin-coupling effects between the irons and the selenium in the cofactor. This provides a basis for further characterization of the electronic state of the FeMo-cofactor due to the loss of three-fold symmetry and the

ability to selectively alter the active site without diminishing its capacity to catalyze reactions.

Cell growth

Azotobacter vinelandii was grown in modified Burke's medium (pH 7.5) bubbled with air [96]. Pre-culture medium was inoculated with Azotobacter glycerol stocks (1:1 v/v cell solution (OD=3-4) with 80% aqueous glycerol), and the 50 and 500 mL preculture contained 10 mM NH_4Cl as the nitrogen source. Precultures were grown at 30° C shaking at 180 rpm for aeration. Main cultures (60 L) were complemented with 1.3 mM NH_4Cl resulting in short-term repression of nitrogenase gene expression, reversible upon ammonium depletion (based upon optimization in [2]). The main culture was grown in a 60 L fermentor at 30° C with stirring of 180 rpm and air bubbled through media at 50 L/min. Cells were harvested by centrifugation at an optical density (OD_{600nm}) of 2.0.

Cell Growth Medium

Component		Concentration	
Sucrose		20	g/L
$FeSO_4$ $7H_2O$		0.2	mM
Na_2MoO_4 $2H_2O$		3	μM
$MgSO_4$		1.67	mM
$CaCl_2$		0.9	mM
KH_2PO_4/K_2HPO_4, pH 7.5		10	mM
NH_4Cl	pre-culture	10.5	mM
	final-culture	1.3	mM

* the final-culture cell growth is done in a 60L fermentor, with constant stirring, so 1/2 mL of PEG 1000 is added as an anti-foaming agent

Nitrogenase Component Proteins Purification

All protein-handling steps were performed anaerobically. The protein purification was modified from [2, 97, 98] (see figure 24 for a schematic overview of the purification). Buffers were degassed using Ar-gas (vacuum-Ar purge cycles) followed by addition of 5 mM $Na_2S_2O_4$ at pH 7.5. Cells were ruptured in a high-pressure homogenizer (Emulsiflex

C5, Avestin) under Ar atmosphere. The cell lysate was centrifuged at 18,900 x g (14,000rpm, JA-14 rotor) for 30 min and the supernatant was loaded onto a HiTrap Q anion exchange column (GE Healthcare) pre-equilibrated with 50 mM Tris/HCl, 100mM NaCl buffer at pH 7.5. MoFe protein was eluted with a linear NaCl gradient at approximately 350 mM, and Fe protein was eluted at approximately 475 mM. After collection, each protein sample was concentrated and loaded onto a size exclusion column (S200, 26/60, GE Healthcare) equilibrated with 50 mM Tris/Cl (pH=7.5), 200 mM NaCl, buffer. Pure MoFe protein was concentrated to ~60 mg mL^{-1} using an Amicon concentrator (100,000 kDa MWCO, Millipore Ultracell) under 5 bar Ar pressure. Fe Protein was concentrated to ~50 mg mL^{-1} using an Amicon concentrator (30 kDa MWCO, Millipore Ultracell) under 5 bar Ar pressure. Nitrogenase activity was assayed by monitoring acetylene reduction (described in the acetylene reduction assay section).

Protein

Protein Purification Buffers

Ion Exchange Chromatography			
Loading buffer		Elution Buffer	
Component	Concentration	Component	Concentration
Tris/HCl, pH 7.5	50 mM	Tris/HCl, pH 7.5	50 mM
NaCl	100 mM	NaCl	1 M
$Na_2S_2O_4$	5 mM	$Na_2S_2O_4$	5 mM

Size Exclusion Chromatography	
Running Buffer	
Component	Concentration
Tris/HCl, pH 7.5	50 mM
NaCl	200 mM
$Na_2S_2O_4$	5 mM

Protein concentrations were determined using UV-vis absorbance at 410 nm, based upon absorption by the metalloclusters. The extinction coefficients used were 76$mM^{-1}cm^{-1}$ for Av1 and 9.4 $mM^{-1}cm^{-1}$ for Av2.

Figure 24: Overview of nitrogenase protein purification scheme (based upon figure 32 of [2]).

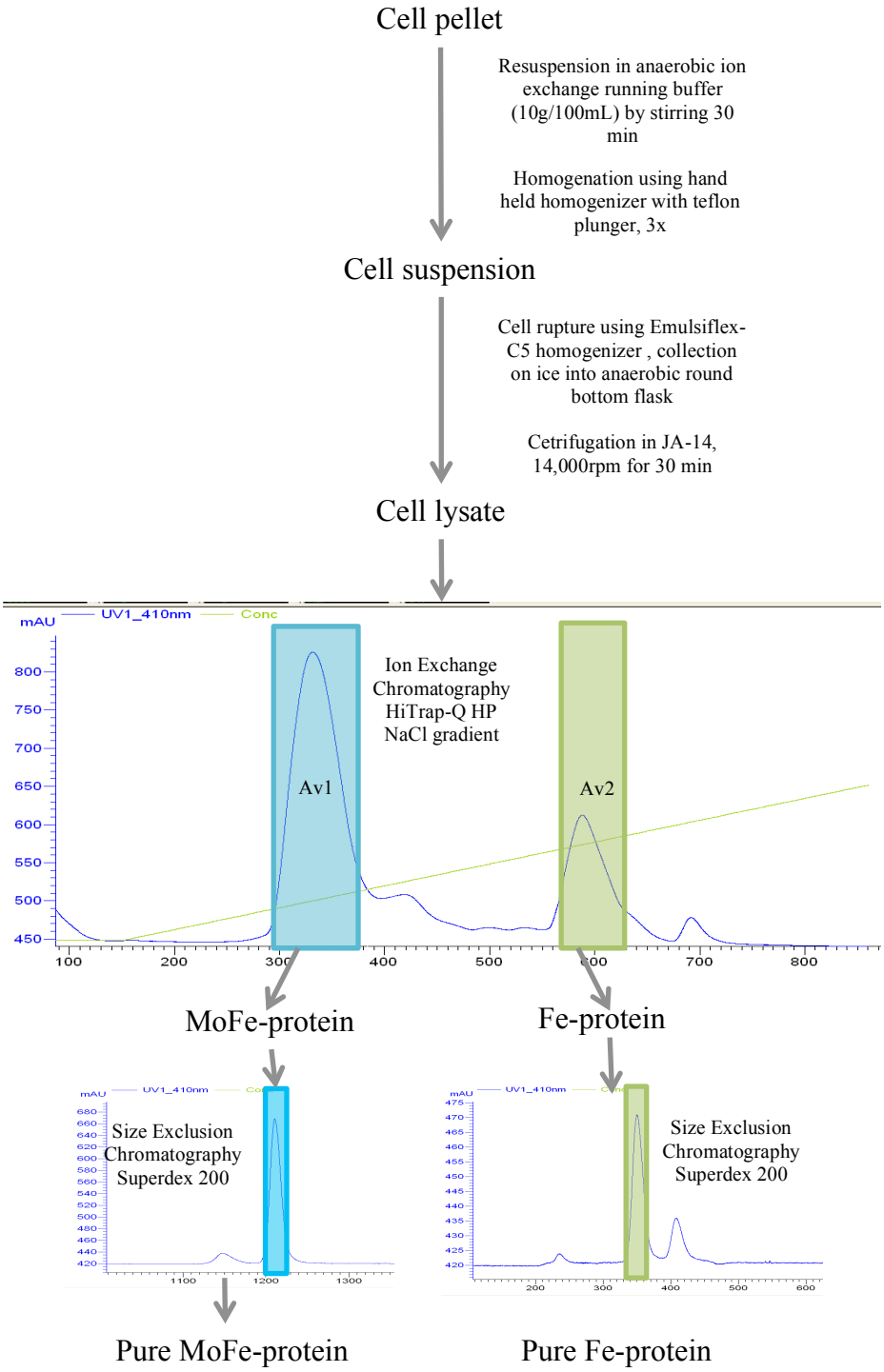

Acetylene Reduction Assay

Nitrogenase activity was determined by monitoring the reduction of acetylene to ethylene in the headspace (9 mL) of reaction mixtures (1 mL) that consisted of 20 mM creatine phosphate, 5 mM ATP, 5 mM $MgCl_2$, 25 units mL^{-1} phosphocreatine kinase, and 25 mM $Na_2S_2O_4$, in 50 mM Tris/Cl (pH 7.5) buffer [99, 100]. All reaction mixtures were made anaerobic (Schlenk line technique) and kept under an Ar-atmosphere. 1 mL of the headspace was replaced by 1 mL acetylene, followed by incubation for 5 minutes at 30^o C. The reaction was initiated by addition of the nitrogenase component proteins (Av2:Av1=2:1, active site ratio: 1:1, 0.25 mg Av1 / 0.27 mg Av2 per assay) and terminated at specific time points by the addition of 1 mL 3M citric acid. Ethylene and acetylene in the assay headspace were measured by gas chromatography (activated alumina 60/80 mesh column, flame ionization detector), with the column oven set at 110°C, and the detector set at 150°C. Peak integration was done using the Peak Simple program (SRI Instruments). Calibration curves were constructed using defined amounts of acetylene in the headspace of protein-free assay mixtures.

N_2 Reduction Assay.

N_2 reduction was monitored by determining ammonia formation, based on a modification of the previously described fluorescence method using an *o*-phthalaldehyde mercaptoethanol reagent [101, 102]. The 1.0 ml assay contained 20 mM creatine phosphate, 5 mM ATP, 5 mM $MgCl_2$, 25 units/mL phosphocreatine kinase, and 25 mM $Na_2S_2O_4$, in MOPS buffer (pH=7.5). The headspace (9 mL) of the assay vial was flushed with N_2 before incubation for 5 min at 30°C. Reactions were initiated by addition of the nitrogenase component proteins (Av2:Av1=2:1, active site ratio: 1:1), and terminated at specific time points by the addition of 300 μL 0.5M EDTA (pH=8.0). The liquid chromatography step in the previously described method was replaced by filtering the assay mixture (Amicon Ultra 3kDa centrifugal filter) and collecting the filtrate, subsequently used for fluorescence measurement. The fluorescence reaction mixture was composed of 20 mM phthalic dicarboxyaldehyde, 3.5 mM 2-mercaptoethanol, 5% v/v ethanol, and 200 mM potassium phosphate (pH 7.3). Fluorescence samples were prepared

by adding 25 uL of sample to 1 mL of the fluorescence reaction mixture, mixed by inverting the solution several times, and allowed to react in the dark for 30 minutes. Fluorescence measurements were performed using a Flexstation 3 plate reader ($\lambda_{excitation}$ = 410 nm, $\lambda_{emission}$ = 472 nm) with SoftMax Pro Microplate Data Acquisition & Analysis Software (Molecular Devices). A calibration curve was generated using NH_4Cl standards from 0.1-10 mM.

Proton Reduction Assay.

Dihydrogen from proton reduction was measured by gas chromatography (molecular sieve 5A-80/100 column) equipped with a thermal-conductivity detector. The assay was identical to the acetylene reduction with the acetylene omitted. Ar was used as the reference/carrier gas. Calibration curves were prepared using 10% H_2 (balance Ar) as a standard by replacing 1 mL of the head space of a standard assay with the standard and injecting 30-50 uL of the head space into the gas chromatogram.

CH_4 production based on KSeCN and KSCN.

Methane, one product of KSeCN and KSCN reduction, was determined by gas chromatography in the headspace of the assay as described above for the acetylene assay. The assay mixture was identical to the acetylene assay except that the acetylene was omitted and KSeCN or KSCN (0.05, 0.1, 0.2, 0.5, 1, 2, 5 mM), as a substrate, was added. Calibration curves were determined with pure methane gas.

Se2B-Labeling of Av1.

Av1-Se2B was prepared based on the above described proton reduction activity assay protocol in the presence of 25 mM KSeCN, providing conditions commensurate with full inhibition of acetylene to ethylene reduction. Av1-Se2B was isolated from the assay mixtures by ultrafiltration using a 100kDa cut-off membrane and washed two times (dilution ratio of 1:100 each) with 200 mM NaCl, 50 mM Tris/Cl buffer pH=7.5 containing 5 mM $Na_2S_2O_4$ to remove excess KSeCN. The protein was further purified by size-exclusion chromatography (Superdex-200, 450mL, 50 mM Tris/Cl buffer pH=7.5

containing 200 mM NaCl and 5 mM $Na_2S_2O_4$). The final protein concentration was adjusted to 30 mg/mL.

Freeze quench sample preparation.

Av1-Se freeze quenched samples were obtained by applying the above described acetylene reduction activity assays, with replacement of wild-type Av1 with Av1-Se2B. Termination of protein activity at distinct time points (correlating with numbers of acetylene reduced per active site of: 2, 46, 341, 921, 1785, 2141, and 5361) was achieved by rapid freezing the activity assay mixtures in liquid nitrogen. The samples were subsequently processed at 3^{o}C. Av1 was isolated by ultrafiltration using 100 kDa cut-off membranes and twice was washed with 200 mM NaCl, 50 mM Tris/Cl pH=7.5, 5 mM $Na_2S_2O_4$ buffer to remove other assay components. The final protein concentration was adjusted to 30 mg/mL and 21°C for crystallization.

CO-inhibition sample preparation

For the preparation of CO-inhibited samples, CO-inhibited activity assays were prepared by saturating the assay mixture with CO, and initiated by addition of Av1 and Av2 (the concentrations of Av1 and Av2 were doubled to provide enough material for crystallization and activity analysis.). After incubating the CO-inhibited assay mixtures for 10 min after protein addition, the assays were combined and concentrated under a CO overpressure of 15 psi in an Amicon ultrafiltration cell with a molecular weight cut-off of 100,000 Da. All subsequent protein-handling steps were carried out under a CO atmosphere. Av1-CO and Av1-Se-CO were prepared in the same way, with the appropriate initial protein sample used (Av1 or Av1-Se2B). Complete CO-inhibition of acetylene reduction was demonstrated by the absence of ethylene production in the assay headspace when both CO and acetylene were present in the headspace.

Reactivation of the CO-inhibited samples

A) A portion of the concentrated CO-inhibited mixture, used to obtain the CO-inhibited structure, was flushed with Ar followed by transfer into a fresh assay mixture containing

the original Av2 assay concentration as well as 1 mL acetylene in the headspace. The MoFe-protein concentration was re-adjusted to its original value by diluting it with 150 mM NaCl, 50 mM Tris/Cl buffer (pH 7.5). Recovery of activity was followed by the production of ethylene in the headspace. The assay mixture was concentrated under Ar and subsequently used for crystallization.

B) CO-inhibited MoFe-protein crystals were harvested and dissolved in 150 mM NaCl, 50 mM Tris/Cl buffer (pH 7.5). The MoFe-protein concentration was re-adjusted to its original assay concentration and transferred into a fresh assay mixture as described in A). Recovery of activity was followed by the production of ethylene in the headspace.

MoFe-protein Crystallization

All Av1 (MoFe-protein) samples (Av1, Av1_CO, Av1_Se2B, Av1_Se freeze-quench, Av1_Se_CO) were crystallized based on the sitting drop vapor diffusion method at 21° C in an anaerobic chamber containing a 95% Ar / 5% H_2 atmosphere. The reservoir solution contained 24-28% PEG 8000 (v/v), 0.75-0.85 M NaCl, 0.1 M imidazole/malate (pH 7.5), 1% glycerol (v/v), 0.5 % 2,2,2-trifluoroethanol (v/v) and 2.5 mM $Na_2S_2O_4$. Samples with CO-inhibition were crystallized with reservoir solutions saturated with CO. Seeding was used to accelerate the crystallization process and to optimize crystal shape. Crystallization drops containing SeCN and/or CO became cloudy upon exposure to the chamber environment (95% Ar/5% H_2), and so crystal looping was difficult, and required quick handling. Cryo-protection was achieved by transferring crystals into a 5 uL drop of reservoir solution containing 8-12 % MPD (v/v). Crystals were looped, and after cryprotection, frozen immediately in liquid nitrogen. These crystallization conditions were based on conditions found in [2, 37].

Co-crystallization with KSCN, NaI, NaBr, or KSeCN.

All co-crystallized MoFe protein samples were crystallized in conditions identical to those described in MoFe-protein Crystallization, but with 10 mM concentration of the desired anion (5 mM and 20 mM were also tested). Crystallization drops became cloudy upon

exposure to the chamber environment (95% Ar/5% H_2), and so crystal looping was difficult, and required quick handling.

Data Collection

Diffraction data were collected at 7100 keV (1.746257 Å, experimentally determined f'' peak position of the Fe-K edge) 12400 (0.999872 Å), and 12662 eV (0.97918 Å, experimentally determined f'' peak position of the Se-K edge) at the Stanford Synchrotron Radiation Lightsource (SSRL) beamline 12-2 equipped with a Dectris Pilatus 6M detector.

Structure Solution and Refinement.

Data were indexed, integrated and scaled using iMosflm, XDS and Scala [103-105]. Phase information were obtained by molecular replacement using the 1.0 Å resolution structure (PDB: 3U7Q) as a model (see figure 25). Structural refinement and rebuilding was carried out in REFMAC5 and COOT [106, 107]. Se-anomalous electron density maps were calculated based on the data collected at 12662 eV, and S-anomalous electron density maps were calculated based on data collected at 7100 eV, using a combination of CAD and FFT embedded in the CCP4 program suite [108].

Figure 25: Flow Chart for Molecular Replacement

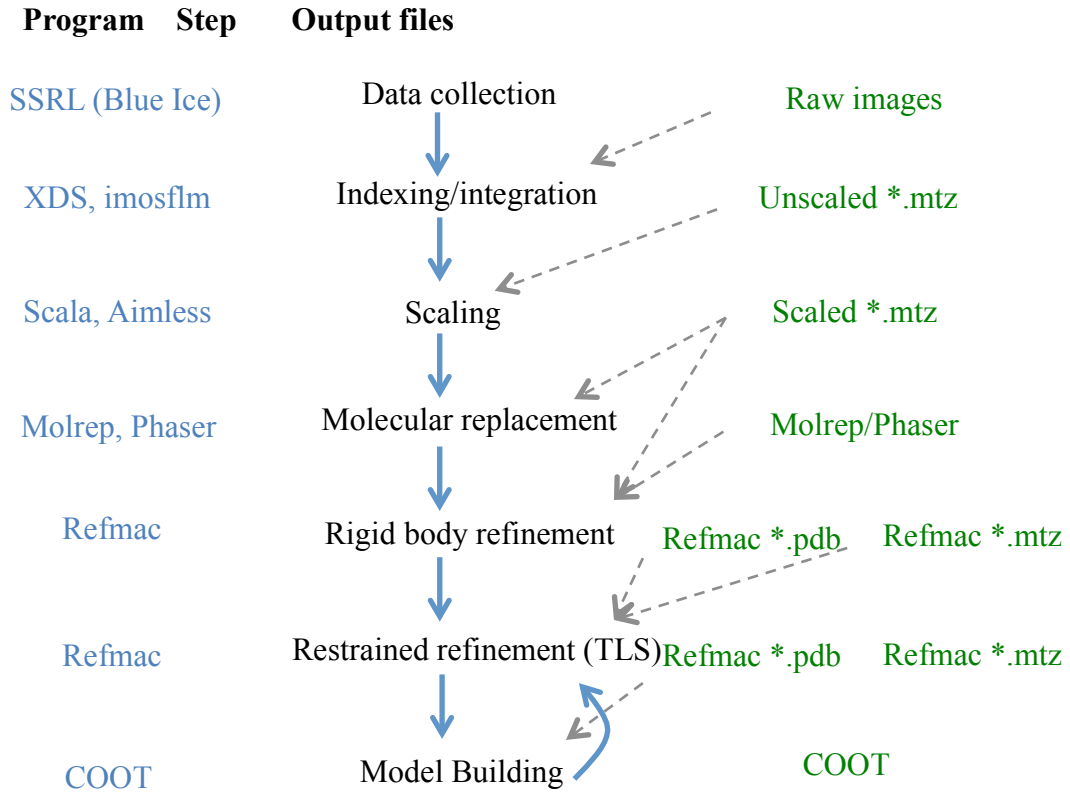

Quantification of Se/Fe/S anomalous electron densities (*f*''12662eV(Se)=3.84e; *f*''12662eV(Fe)=1.50e; *f*''12662eV(S)=0.24e) based on the refined structural models was performed using a MAPMAN-dependent script, allowing a free choice of radius of integration and B-factor cut-off [28, 37, 109]. All protein and active site structures were rendered in PYMOL.

* All crystallographic data was collected and refined with Dr. Thomas Spatzal

CW-EPR Spectroscopy

All cw-EPR data was collected with, and analyzed in collaboration with the group of Dr. Stephan Weber (Albert-Ludwigs-Universität Freiburg, Germany) by Lorenz Heidinger and Dr. Erik Schleicher.

Samples were prepared as described in Av1_Se2B labeling, followed by an additional purification step using size-exclusion chromatography (Superdex-200 column material), then concentrated to ~70-100 mg/mL by ultrafiltration with a 100 kDa cutoff membrane. Samples were prepared with both natural abundance selenium KSeCN, and $K^{77}SeCN$, synthesized from 99% enriched ^{77}Se (Cambridge Isotope Laboratories, Inc) and KCN (prepared by J. Rittle). Protein was then transferred to an EPR tube (both X-band and Q-band tubes were filled) in an anaerobic chamber (95% Ar/5% H_2 atmosphere), and frozen in liquid nitrogen.

All data was recorded using a cw- X-band EPR-spectrometer (ELEXSYS E500, 10" ER073 Electromagnet, Super High Q resonator cavity; Bruker Biospin GmbH) equipped with a continuous-flow liquid helium cryostat (ER 4112HV; Oxford Instruments). Spectra were recorded at temperatures of 4-10 K and microwave power of 10 mW. Microwave frequencies were all ~9.37 GHz, modulation amplitude 6 G, modulation frequency 100 kHz, and receiver gain 47 dB.

Analysis of the distribution of rhombicity in the EPR spectra required application of a Tikhonov regularization. Each cw spectra for the kernel was calculated by using the Easyspin algorithm, "pepper" [110].

ESEEM spectroscopy

All ESEEM data was collected with and analyzed in collaboration with the group of Dr. Stephan Weber (Albert-Ludwigs-Universität Freiburg, Germany) by Lorenz Heidinger and Dr. Erik Schleicher.

Samples for ESEEM were identical to samples prepared for cw-EPR measurements.

All 3-pulsed ESEEM data was recorded using a pulsed EPR-spectrometer (ELEXSYS E580, 3W Q-band solid state amplifier, Q-band ENDOR Resonator EN 5107D2; Bruker Biospin GmbH) equipped with a continuous-flow liquid helium Q-band Cryostat (CF935; Oxford Instruments). Spectra were recorded at temperatures of 4.5 K and microwave frequency 33.8116 GHz, with the magnetic field swept from 440 mT to 1340 mT (220 data points). The $\pi/2$ pulses were set 16 ns and four-step phase cycling was applied. All 3-pulse ESEEM experiments were recorded with a detection bandwidth of 20 MHz and repetition time of 50 μs. The initial T-value was set to 120 ns with 12 ns stepping. The data was processed by subtracting a bi-exponential decay using a hamming window function and a zero-filling factor of 3 before Fourier-transformation.

Results

Structural Characterization CO-inhibited MoFe-protein

Crystallographic analysis of a CO-inhibited nitrogenase MoFe-protein required identification of conditions capable of fully inhibiting the enzyme (except for proton reduction), and to ensure that the CO remained bound to the FeMo-cofactor. This was accomplished through protein handling under a CO atmosphere during each step in crystallization sample preparation, and preparing crystallization conditions saturated with CO.

Through optimization of protein handling and crystallization conditions with CO, we were able to isolate the CO-inhibited MoFe-protein and crystallize it to obtain a 1.50 Å resolution structure, revealing a single CO bound in a μ_2-bridging mode, and displacing a belt sulfur atom, S2B (see figure 26).

Analysis of the CO-inhibited structure revealed that the CO sits at a distance of 1.86 Å from Fe2 and Fe6, with the structure slightly "bending" with the Fe2-Fe6 distance changing from 2.6 Å to 2.5 Å, and a 6° tilt along the Fe1-C-Mo axis towards the CO (figure 26 C).

Complete S2B displacement was determined using anomalous difference Fourier maps calculated with data collected at 7100eV; this energy was chosen as S has a f" contribution of ~0.7 e-, and this energy is below the K-edge for Fe, ensuring a substantial anomalous signal from S (see figure 26 b). CO electron density was determined based upon comparison to all other C and O electron density in the protein structure (i.e. as internal standards), applying integration spheres of radius 1 Å, and exclusion of atoms with a B-factor >25 (see figure 27). This analysis showed good agreement with the S2B site being occupied with a single CO bound with the C binding to Fe2 and Fe6.

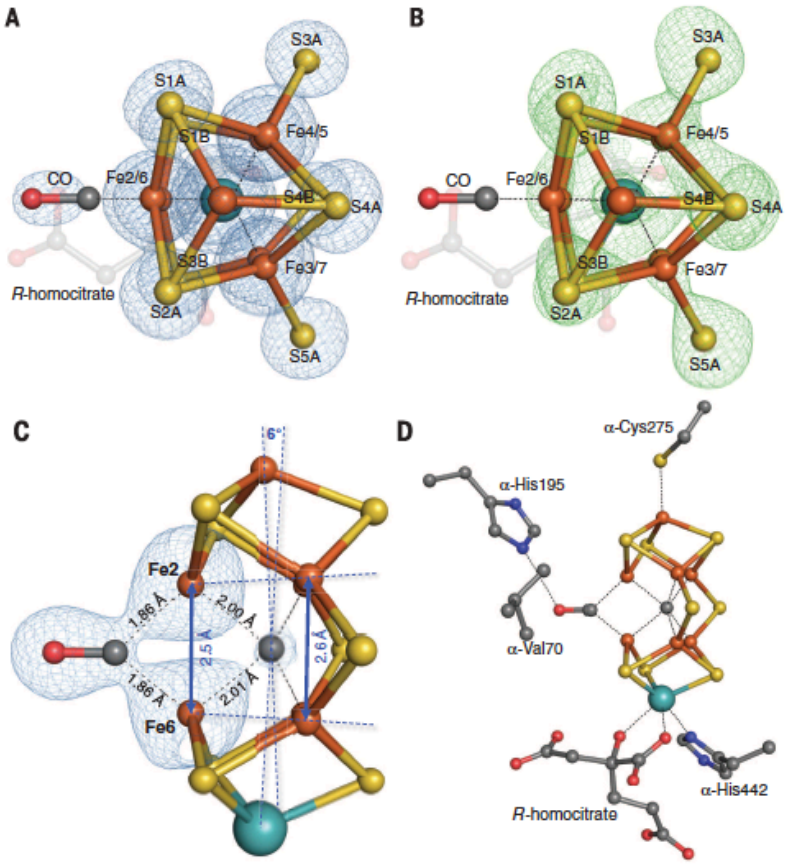

Figure 26: CO-inhibited MoFe-protein: Refined structure of the CO-bound FeMo-cofactor at a resolution of 1.50 Å. Irons are shown in orange, sulfur in yellow, molybdenum in cyan, nitrogen in blue, carbon in grey, and oxygen in red. (this figure is from [109])

A) view along the Fe1-C-Mo axis of the FeMo-cofactor The $2F_{obs}$-F_{calc} map is contoured at 4.0 σ and shown as blue mesh.

B) same orientation as A), superimposed with the 7100 eV anomalous density map, shown as a green mesh, at a resolution of 2.1 Å and contoured at 4.0 σ showing the absence of S anomalous scattering at the S2B site, indicating replacement by CO.

C) side view of the FeMo-cofactor highlighting the CO-binding geometry. The electron density map, in blue mesh, surrounding CO-Fe2-Fe6-C is contoured at 1.5 σ.

D) Same orientation as in C), highlighting the ligand environment of the FeMo-cofactor. The catalytically relevant side chains, α-Val70 and α-His195, are both in close proximity to the bound CO.

Table 3: X-ray data Collection Statistics for the Av1_CO structure at a resolution of 1.50 Å (table is from [109])

Av1-CO		
Data collection statistics	**High resolution**	**Anomalous (sulfur)**
Wavelength (Å)	0.99987	1.74626
Resolution range (Å)	49.56 – 1.57 (1.66 – 1.57)	38.77 – 2.1 (2.21 – 2.10)
Unique reflections	271,948 (37,922)	118,541 (16,880)
Completeness (%)	95.4 (91.2)	97.5 (95.5)
Multiplicity	6.0 (5.4)	6.5 (6.1)
Space group	$P2_1$	$P2_1$
Unit cell parameters		
a, b, c	81.23, 130.75, 107.07	81.23, 130.71, 107.06
α, β, γ	90.0, 110.67, 90.0	90.0, 110.64, 90.0
R_{merge}	0.118 (0.667)	0.041 (0.111)
$R_{p.i.m.}$	0.051 (0.282)	0.017 (0.048)
I / σ(I)	10.0 (2.3)	33.1 (13.9)
Data processing statistics		
R_{cryst} (%)	13.91	14.27
R_{free} (%)	15.54	16.26
r.m.s.d. bond lengths (Å)	0.011	0.011
r.m.s.d. bond angles (°)	1.721	1.640
Average B-factor ($Å^2$)	13.67	13.29
Ramachandran: allowed (outliers) (%)	99.4 (0.6)	99.35 (0.65)

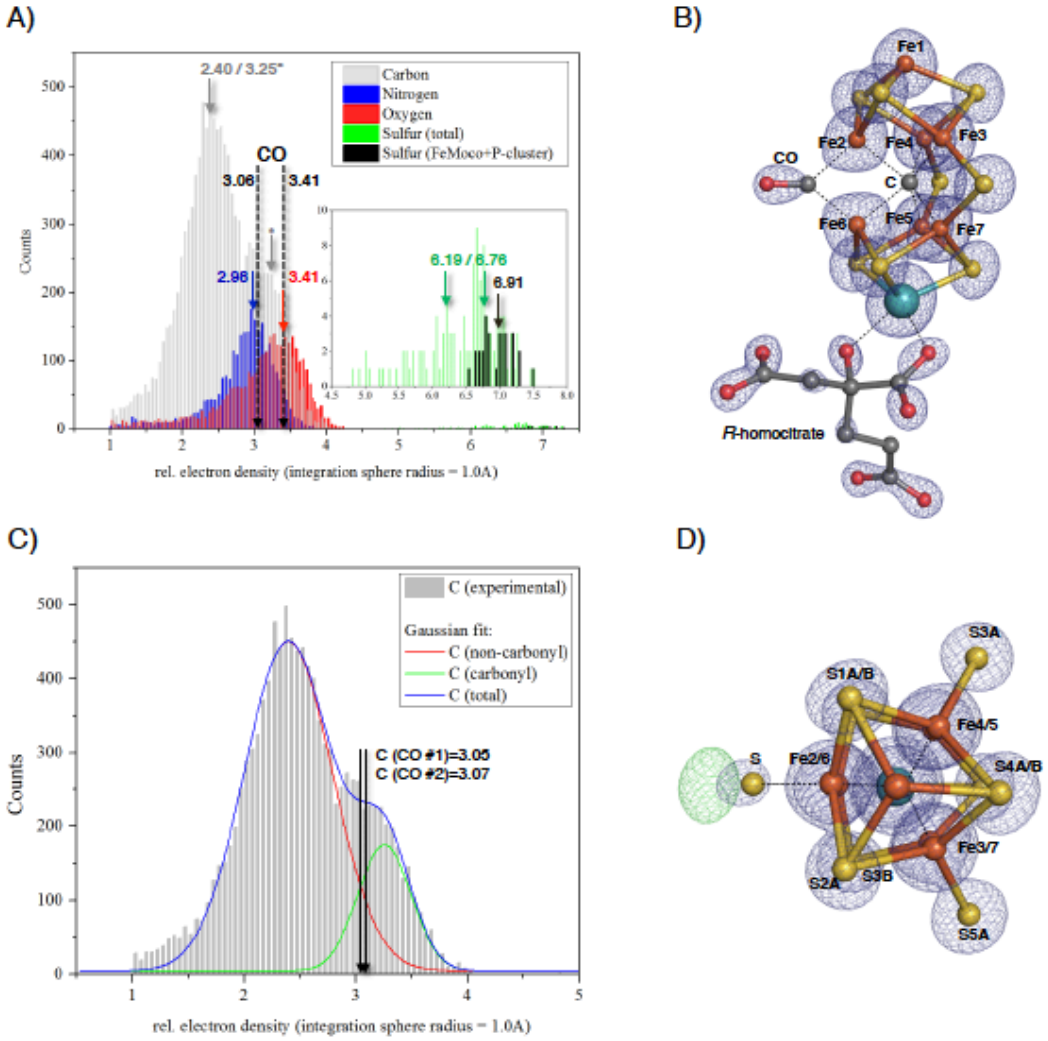

Figure 27: Electron density analysis of carbon monoxide displacement of sulfur at the S2B site. (this figure is from [109])

A) Average electron densities for carbon, nitrogen, oxygen, and sulfur determined by applying a 1 Å radius integration sphere to each atom of (atoms with a B-factor >25 $Å^2$ were excluded from the analysis). Obtained values are plotted against the number of observations and plotted as histograms. Peak positions represent average electron density for each king of atom, and represent Gaussian fits to the data. The CO electron density is in agreement with the average values for carbon (carbonyl-C) and oxygen.

B) Side view of the CO-inhibited FeMo-cofactor superimposed with the electron density ($2F_{obs}$-F_{calc}) contoured at 4.0 σ (shown as blue mesh). The CO electron density is equivalent to that seen in the carbonyl-bonds in the R-homocitrate ligand.

C) Electron density histogram for carbonyl and non-carbonyl carbons. At 1.50 Å resolution, the higher electron density for carbonyl bonds can be discriminated from non-carbonyl carbons. Two histograms can be fit for the two carbon classes, and comparison made with the CO ligand. The CO carbon is in agreement with the electron density for carbonyl carbons in the molecule. Deviation from the peak can be explained by proximity to Fe2 and Fe6

D) Electron density ($2F_{obs}$-F_{calc}), in blue mesh, and difference electron density (F_{obs}-F_{calc}) , in green mesh, map of the CO-inhibited FeMo-cofactor contoured at 4.0 σ. Strong positive difference density peak is indicated at the position of the oxygen atom of CO in green mesh.

Reactivation of the CO-inhibited MoFe-protein

After characterizing the CO-inhibited state, we sought to identify if the protein had been irreversibly modified, or if reactivation was possible. In order to do this, two approaches were taken: CO-inhibited crystals were dissolved in a complete assay mixture with added Fe-protein, and CO-inhibited MoFe protein was isolated from CO-saturated assay and then added back to CO-free assays containing acetylene. For both activity measurements, ethylene production was measured, and showed that the CO-inhibition was reversible with near-quantitative recovery (94 ± 4 %) of normal activity (table 4). Reactivated CO-inhibited MoFe-protein was isolated from the activity mixture and crystallized, yielding a 1.43 Å resolution structure. The reactivated structure revealed that the S2B sulfur was regained at full occupancy (figure 28), leaving the FeMo-cofactor in the resting state.

Sample	Specific Acetylene Reduction Activity	
	nmol C_2H_4/min/mg Av1	Percent (%)
Av1	1930 ± 90	100 ± 5
Av1-CO inhibited	< 2 ± 2	< 0.1 ± 0.1
Av1-reactivated	1820 ± 80	94 ± 4

Table 4: Comparison of acetylene reduction activity for Av1, CO-inhibition of Av1, and reactivation of Av1-CO. Errors represent standard deviations based upon three measurements. (this figure is from [109])

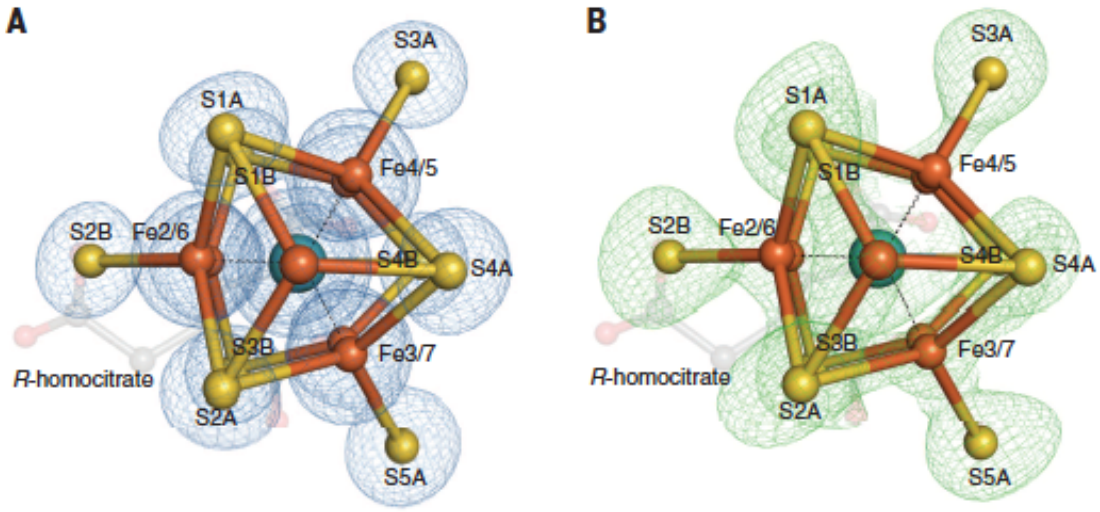

Figure 28: Reactivated MoFe-protein. Refined structure of the reactivated FeMo-cofactor at a resolution of 1.43 Å. Color scheme is according to Figure CO. (this figure is from [109])

A) view along the Fe1-C-Mo axis of the FeMo-cofactor The $2F_{obs}$-F_{calc} map is contoured at 4.0 σ and shown as blue mesh. Electron density at the S2B site is in agreement with a sulfur at this site.

B) same orientation as A), superimposed with the 7100 eV anomalous density map, shown as a green mesh, at a resolution of 2.15 Å and contoured at 4.0 σ showing the presence of S anomalous density at the S2B site.

Table 5: X-ray Data collection Statitstics for the Reactivated CO-inhibited Nitrogenase at a resolution of 1.43 Å. (this table is from [109])

Av1-reactivated **Data collection statistics**	**High resolution**	**Anomalous (sulfur)**
Wavelength (Å)	0.99987	1.74626
Resolution range (Å)	39.76 – 1.50 (1.58 – 1.50)	38.69 – 2.15 (2.27 – 2.15)
Unique reflections	321,467 (46,413)	107,219 (14,923)
Completeness (%)	96.9 (95.9)	94.6 (90.2)
Multiplicity	7.0 (7.0)	6.8 (6.8)
Space group	$P2_1$	$P2_1$
Unit cell parameters		
a, b, c	80.94, 130.79, 107.00	81.05, 130.86, 107.07
α, β, γ	90.0, 110.58, 90.0	90.0, 110.56, 90.0
R_{merge}	0.121 (0.647)	0.068 (0.107)
$R_{p.i.m.}$	0.049 (0.260)	0.028 (0.044)
I / σ(I)	11.0 (2.8)	20.7 (13.8)
Data processing statistics		
R_{cryst} (%)	13.05	13.49
R_{free} (%)	15.42	15.64
r.m.s.d. bond lengths (Å)	0.010	0.010
r.m.s.d. bond angles (°)	1.683	1.566
Average B-factor ($Å^2$)	9.42	11.55
Ramachandran: allowed (outliers) (%)	99.52 (0.48)	99.52 (0.48)

Site-specific Labeling and Migration of Se in the FeMo-cofactor

Characterization of KSeCN inhibitory properties

$SeCN^-$ was identified as a potent inhibitor and weak substrate of nitrogenase based upon previously identified inhibitory and substrate properties of SCN^- [111]. The inhibitory properties of $SeCN^-$ and SCN^- were characterized, finding the inhibition constant, K_i, for $SeCN^-$ to be thirty times lower than that of SCN^-, with K_i values of 410 ± 30 μM and 12.7 ± 1.2 mM respectively (see figure 29, and 30a). Additionally, $SeCN^-$ was identified as a weak substrate by methane production, also a product observed from reduction of thiocyanate (see figure 31) [111] and cyanide [112]. Proton reduction activity was retained in the presence of $SeCN^-$, although at a decreased level (figure 30b).

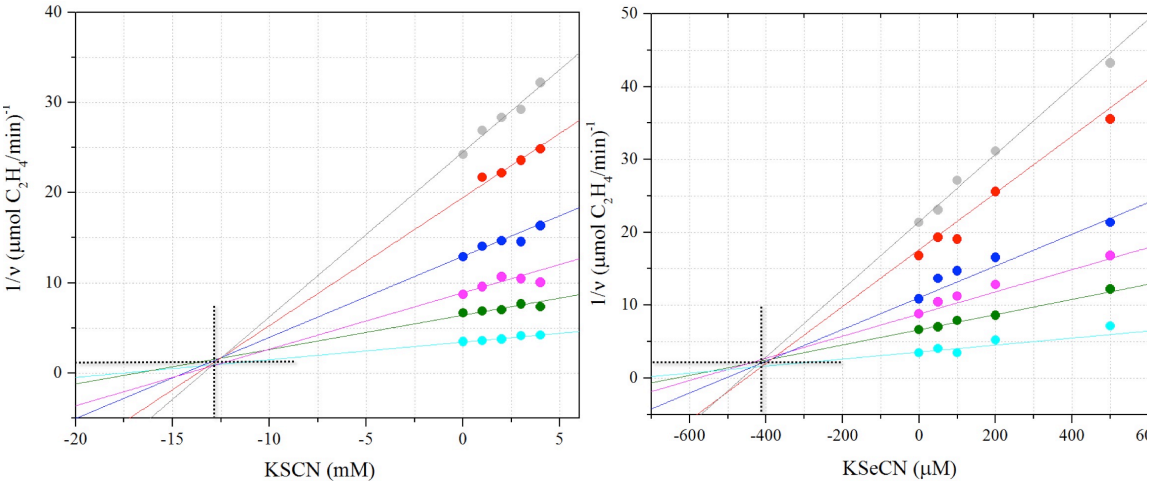

Figure 29: Inhibition constant characterization for acetylene reduction by KSeCN and KSCN
Inhibitory properties of KSeCN and KSCN were determined using a modified acetylene reduction assay. Concentrations for substrate (C_2H_2) were below saturation and concentrations for inhibitors (KSCN, KSeCN) were at low inhibition to allow for analysis. Dixon plots were prepared by plotting 1/v versus inhibitor concentration. K_i was determined from the intersection point derived from unrestrained linear fits of data points.
A) Dixon plot for KSCN, showing a K_i of 12.7 ± 1.2 mM KSCN. Concentrations of C_2H_2 were varied as follows: 20 (grey), 30 (red), 40 (blue), 60 (magenta), 100 (green), and 500 (teal) μL per 9 ml total headspace volume. Concentrations of KSCN were: 0, 1, 2, 3, 4 mM.
B) Dixon plot for KSeCN, showing a K_i of 410 ± 30 uM KSeCN. Concentrations of C_2H_2 were varied as follows: 20 (grey), 30 (red), 40 (blue), 60 (magenta), 100 (green), and 500 (teal) μL. Concentrations of KSeCN were: 0, 50, 100, 200, 500 μM.
Error bars represent standard deviations from three measurements. (this figure is from [113])

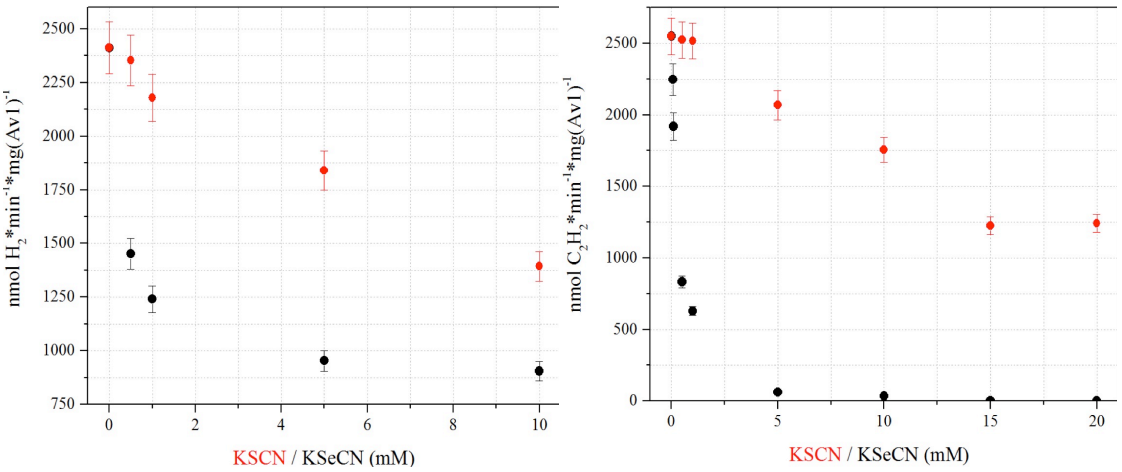

Figure 30: Nitrogenase activity in the presence of KSeCN or KSCN

A) Acetylene reduction activity in the presence of KSeCN (black) or KSCN (red) at varied concentrations: 50 µM, 75 µM, 100 µM, 500 µM, 1 mM, 5 mM, 10 mM, 15 mM, and 20 mM.

B) Proton reduction activity as a function of KSeCN (black) or KSCN (red) concentrations (0, 0.5, 1, 5, 10 mM). Green bars represent ratios between H_2 production in the presence of KSeCN versus KSCN. H_2 production in the presence of 10 mM KSeCN is approximately 65% when compared to 10 mM KSCN, and approximately 38% in comparison to the KSCN/KSeCN free reduction activity.

Error bars represent standard deviations from three measurements. (this figure is from [113])

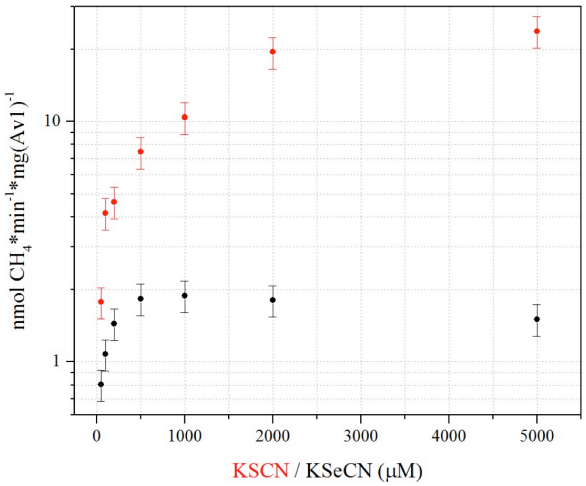

Figure 31: Methane production based upon KSeCN and KSCN as substrates

Methane production was determined based on 0.05, 0.1, 0.2, 0.5, 1, 2, 5 mM KSCN (red) or KSeCN (black) as substrates. Maximum CH_4 production from KSeCN was obtained at a concentration of 1 mM, whereas CH_4 production from KSCN does not reach maximum within the tested range. Green bars represent ratios between CH_4 production in the presence of KSeCN versus KSCN. Error bars represent standard deviations from three measurements. (this figure is from [113])

Site-specific Se-incorporation into the FeMo-cofactor

Investigation into a 1.60 Å structure of the $SeCN^-$ inhibited MoFe-protein led to identification of site-specific catalysis-dependent Se insertion into the S2B site of the FeMo-cofactor (Av1_Se2B) (see figure 32), as was seen with CO (see figure Se2B). Quantitative Se displacement of the S2B sulfur was characterized by analysis of the anomalous difference density map at the Se-K edge *f"* peak at 12662 eV, using the Fe atoms of the FeMo-cofactor and P-cluster as internal references. The overall geometry of the FeMo-cofactor in Av1_Se2B did not show any perturbation at this resolution, reflecting the small increase in the ionic radius of Se (3.8%) as compared to S [114].

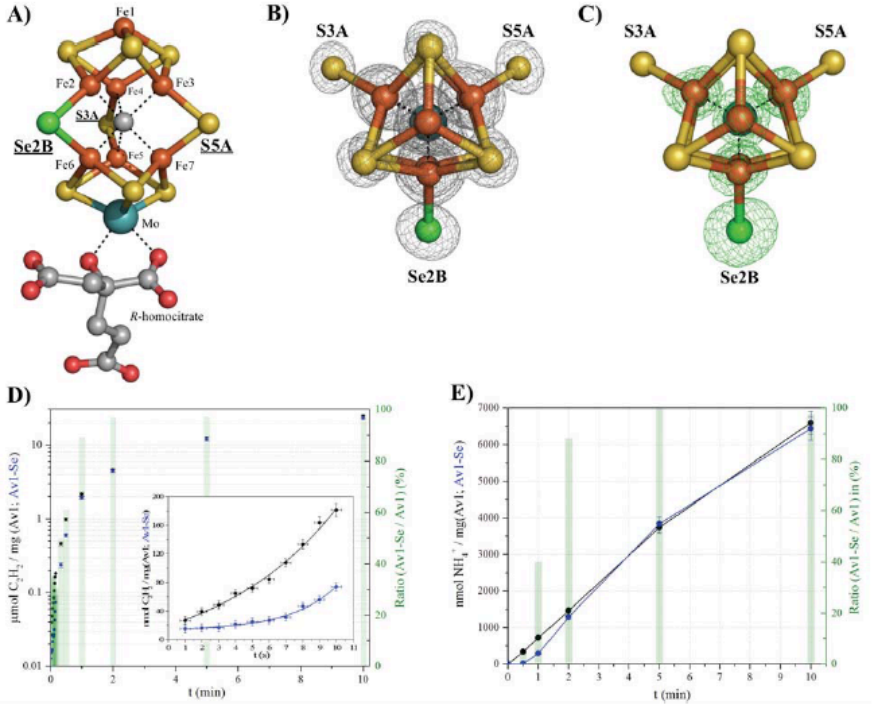

Figure 32: Site-Selective Se-incorporation into the FeMo-cofactor

A) Side view of the Se-incorporated FeMo-cofactor (FeMoSeco [7Fe:8S:Se:Mo:C]-*R*-homocitrate) within Av1_Se2B at a resolution of 1.60 Å highlighting the S2B sulfur replacement by Se.

B) View along the Fe1-C-Mo axis of FeMoSeco. The electron density ($2F_{obs}$-F_{calc}) map, shown as a grey mesh, is contoured at 5.0 σ. Electron density of the incorporated Se is significantly higher than that at the S3A and S5A sites, correlating with the higher electron density of Se.

C) FeMoSeco in the same orientation as B) superimposed with the anomalous difference Fourier map calculated at 12662 eV, shown as a green mesh, at a resolution of 1.60 Å and contoured at 5.0 σ showing the anomalous Se density at the S2B site arising from the presence of a Se. Fe atoms are shown in orange, S in yellow, Se in green, Mo in cyan, C in grey, and O in red.

D) Acetylene reduction assay of wt-Av1 (black) compared with Av1_Se (blue). Inset: product formation during the first 10 s shows a comparative lag for acetylene reduction by Av1_Se

E) Ammonia formation from reduction of N_2 determined for Av1_wt (black) as compared with Av1_Se. Error bars represent standard deviations from three measurements.
(this figure is from [113])

Av1_Se2B Substrate Reduction Activity

Upon establishing that the S2B sulfur was displaced by a Se, analysis of the activity of the Se-labeled MoFe-protein Av1-Se2B) was tested to ensure that the enzyme had not been irreversibly inhibited or significantly altered. When compared to native MoFe-protein, the Av1-Se2B retained substrate (acetylene, proton and dinitrogen) reduction activity. Analysis of the substrate reduction activity revealed a longer initial lag phase than with the wild type protein (figure 32 d,e)

Se-migration in the FeMo-cofactor

Characterization of Av1-Se2B after acetylene reduction demonstrated that the site-specifically inserted Se was not simply ejected from the FeMo-cofactor, as had been hypothesized with the Av1-CO, but had partially migrated to the other two belt-sulfur sites, S3A and S5A. This led to development of a method to freeze-quench (fq) acetylene reduction assays in order to trace the Se-label at specific time points for crystallographic investigation.

Crystallographic characterization of seven fq MoFe-protein samples (Av1-Se-fq) at time points corresponding to 2 to 5360 acetylene reduced per FeMo-cofactor (designated Av1-Se-fq-2 to Av1-Se-fq-5360). The structures, at resolutions of 1.32 – 1.66 Å, represent the first example of time-dependent structural snapshots of the nitrogenase active site during turnover (figure 33). The structures demonstrate a relationship between enzyme catalysis and migration from the Se at the S2B site into the S5A and S3A belt sulfur sites.

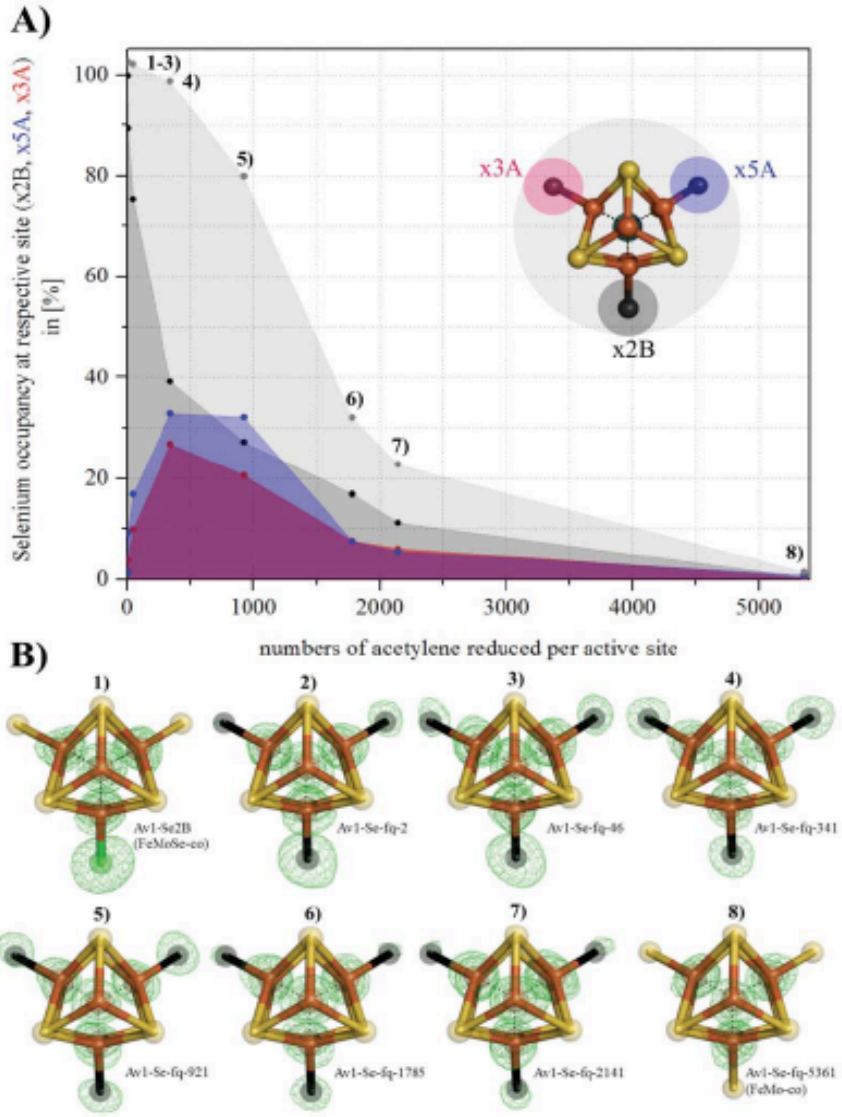

Figure 33: Catalysis dependent Se migration in the FeMo-cofactor

A) Se-occupancy in the active site as a function of numbers of acetylene reduced per cofactor. Se occupancy of S2B shown in dark grey, S5A in blue, and S3A in red. The sum of Se-occupancy (Se2B + Se3A + Se5A) is shown in light grey.

B) Structural models of Se-incorporated FeMo-cofactor during turnover. 1) FeMoSe-cofactor resting state in Av1_Se2B. 2-8) Cofactor structures obtained at seven time points according to the number of acetylene reduced per active site: 2, 46, 341, 921, 1785, 2141, and 5361. Crystal-structure resolutions (in the order 1-8): 1.60 Å, 1.50 Å, 1.45 Å, 1.32 Å, 1.64 Å, 1.66 Å, 1.65 Å, and 1.48 Å respectively. Anomalous Fourier difference maps calculated at 12662 eV and contoured at 5.0 σ, shown as green mesh, allowed for quantification of Se-occupancy. Color scheme is according to figure Se2B.

(this figure is from [113]).

CO-inhibition of Av1_Se2B

The previously characterized CO inhibited FeMo-cofactor identified replacement of the S2B sulfur with CO [109]. This led us to characterize the structure of the CO-inhibited Av1_Se2B (Av1_Se_CO) in order to determine the location of the displaced Se2B atom. The Av1_Se_CO structure was refined to a resolution of 1.53 Å, and revealed that the Se2B atom was ca. 90% replaced by a μ_2-bridging CO (see figure 34), as in the Av1_CO structure [109] (see figure 26). Additionally, the Se was not expelled from the FeMo-cofactor, but migrated to the S3A and S5A belt sulfur sites with ca 88% overall retention (the S3A site had a Se-occupancy of ~35% and the S5A site had a Se-occupancy of ~44%) (see figure 34).

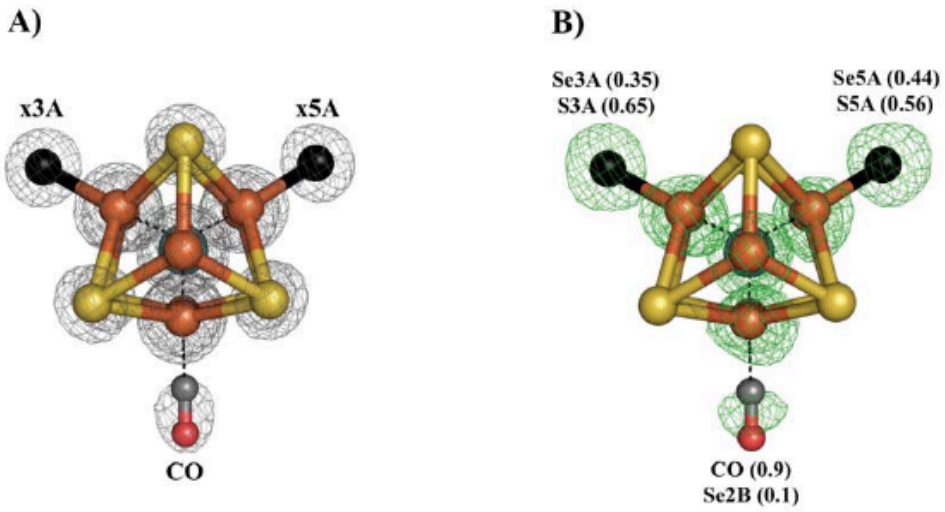

Figure 34: Se-migration upon CO binding to Av1_Se2B
Structure of Av1_Se_CO at a resolution of 1.53 Å, highlighting the Se-migration from the S2B site to the S3A and S5A sites.

A) View along the Fe1-C-Mo axis of the active site. The electron density ($2F_{obs}$-F_{calc}) map, shown as a grey mesh, is contoured at 5.0 σ. Electron density of the bound CO is significantly lower than that at the S3A and S5A sites.

B) Same orientation as A) superimposed with the anomalous difference Fourier map calculated at 12662 eV, shown as a green mesh, at a resolution of 1.53 Å and contoured at 5.0 σ showing the anomalous Se density at the S3A and S5A sites arising from the presence of Se, and very low anomalous density at the S2B site, indicative of the CO bound. Numbers in parentheses represent the occupancy of the specified group.

(this figure is from [113])

Investigation into the potential Sulfur-binding Site

Upon identification of the S2B sulfur being displaced by CO, the question of where the sulfur had migrated to arose [109]. Upon careful inspection of the 7100 eV anomalous different Fourier map, a potential sulfur binding site (pSBS) was identified. The pSBS is positioned ~22 Å away from the S2B site in the FeMo-cofactor, and is located at the interface between the α- and β- subunits forming a pocket formed by side chain residues of α-Arg93, α-Thr104, α-Thr111, α-Met111, β-Asn65, β-Trp428, β-Phe450, and β-Arg453 (fig 35). The pocket has a positive surface charge, which would be amenable to accommodation of an anionic species such as HS^- or S^{2-}. Additionally, this site is connected to the FeMo-cofactor through a discontinuous water channel.

Further investigation into the pSBS led us to experimentally test if this site is a generic anionic binding site, or if it is specific to binding a sulfur species. Co-crystallization with varied concentrations (5-20 mM) NaI and NaBr did not result in I^- or Br^- species present in the pSBS, with inspection of the electron density map ($2F_{calc}$-F_{obs}) for increased electron density reflective of an I^- species, and of the anomalous Fourier difference density map at 13481 eV for Br^-. Co-crystallization with SCN^- resulted in increased electron density and the presence of anomalous density from the anomalous Fourier difference density at 7100 eV, indicating that a SCN^- was bound at this site, but due to the similar anomalous scattering factor and ubiquitous presence of Cl^- species, could not be defined as one or the other, although modeling of SCN- at this site is in good agreement with the electron density (see figure 36). Analysis of the $SeCN^-$ inhibited Av1_Se2B structure, as well as a MoFe-protein sample co-crystallized with KSeCN, revealed a low occupancy (varying between 0-20%, dependent upon $SeCN^-$ concentration, 10-25mM) anomalous density in the 12662 eV anomalous Fourier difference density map, although at this low occupancy conclusive analysis is not possible.

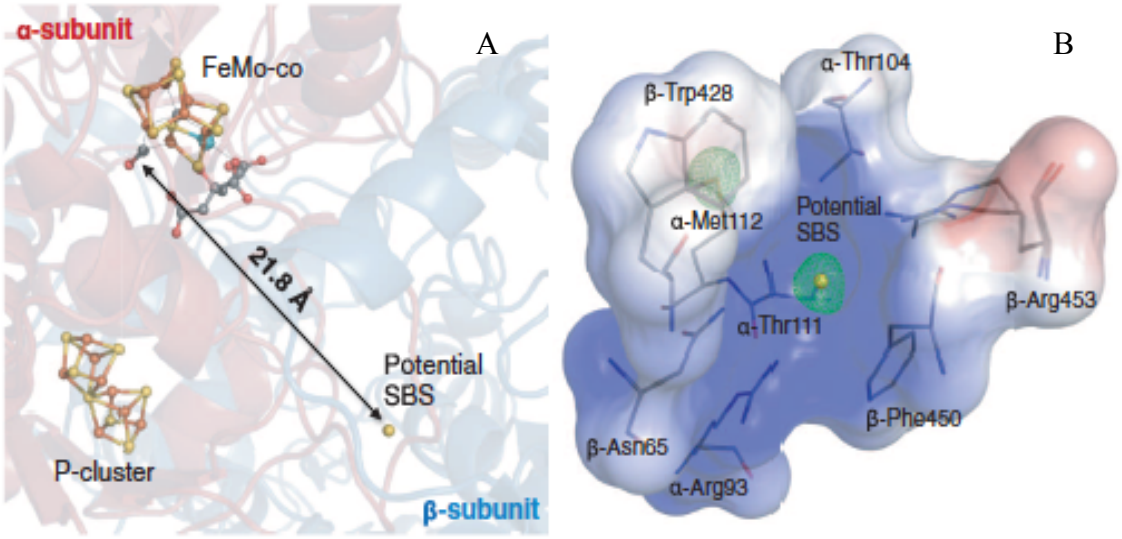

Figure 35: Potential Sulfur-binding site (pSBS) in the CO-inhibited MoFe-protein

A) Location of the potentially bound sulfur in a cavity at the interface between the α- and β- subunits. The pSBS is located 22 Å from the S2B site of the FeMo-cofactor.

B) Enlarged representation of the pSBS cavity. Positive surface charge is represented in blue, negative in red. The 7100 eV anomalous density map at a resolution of 2.1 Å is represented as a green mesh and contoured at 4.0 σ, showing the presence of an anomalous density in the pSBS. The side chain sulfur of α-Met112 acts as an internal standard for full occupancy.

(this figure is from [109])

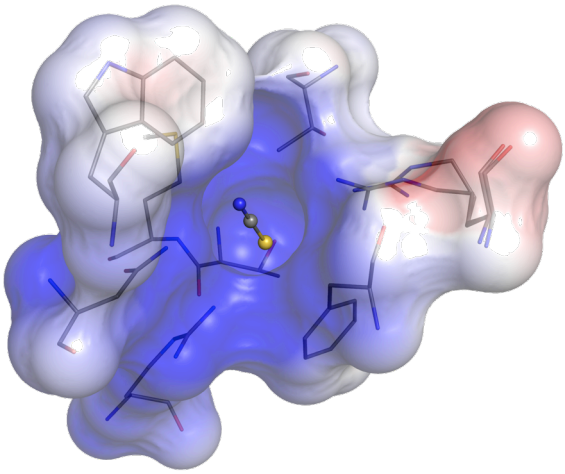

Figure 35: Potential Sulfur Binding site from crystals co-crystallized with 10 mM SCN^-

The pSBS pocket is shown here with a SCN- ligand fit to the electron density and the 12662 eV anomalous Fourier difference density. The position of the S from SCN- is approximately at the same site as the proposed sulfur species identified in the pSBS of the CO-inhibited MoFe structure (see figure pSBS).

Table 6: Data collection and refinement statistics for the SCN^- co-crystallized (10mM) MoFe-protein (Av1-SCN). Values in parentheses represent the highest resolution shell.

Av1-SCN **Data collection statistics**	**High resolution**	**Anomalous**
Wavelength (Å)	0.99987	1.74626
Resolution Range (Å)	38.64 - 1.28 (1.35 - 1.28)	40.08 - 2.05 (2.16 - 2.05)
Unique reflections	4997130 (622666)	119405 (14482)
Completeness (%)	95.9 (84.5)	94.7 (82.9)
Multiplicity	6.6 (5.9)	6.4 (5.6)
Space group	$P2_1$	$P2_1$
Unit cell parameters		
a, b, c	77.34, 130.84, 107.00	77.34, 130.84, 107.00
α, β, γ	90.0, 108.94, 90.0	90.0, 108.94, 90.0
R_{merge}	0.094 (0.732)	0.055 (0.090)
$R_{p.i.m}$	0.039 (0.322)	0.023 (0.040)
I/σ(I)	11.9 (2.2)	24.3 (14.1)
Data processing statistics		
R_{cryst} (%)	12.87	15.03
R_{free} (%)	15.54	17.12
r.m.s.d. bond length (Å)	0.015	0.012
r.m.s.d. bond angles (°)	1.772	1.661

CW-EPR of Av1_Se2B: X-band EPR

Isolation of a site-specific alteration of the FeMo-cofactor with incorporation of selenium led to an investigation of the altered active site by EPR. X-band cw-EPR of the resting state wt-Av1 showed the as-expected rhombic signal expected for the 3/2 spin state, with the lower Kramer's doublet dominating the spectrum with fictitious principal g-values of [g_x, g_y, g_z] = [4.31, 3.65, 2.01] (see figure EPR A) [2, 37]. X-band cw- EPR of resting state Av1_Se2B and isotopically labeled Av1_^{77}Se2B showed significant splitting of the g-values remaining the same. The natural abundance vs isotopically labeled samples show similar splitting with differences in peak intensities.

For the lower Kramer's doublet, the fictitious g-values are dominated by the rhombicity (λ = E/D) [citation]. To obtain the distribution of rhombicity, a Tikhonov regularization was applied, giving rise to quite good peak fitting (shown in figure 37 A, B, C in green, with experimentally recorded spectra in blue). Analysis of the E-values gave a single peak for the wild-type Av1, but gave ~5 peaks indicating a distribution of E-values for the selenium incorporated samples (see insets for figure 37). Applying different λ-values while keeping the g-values constant in the cw-EPR spectra regularization indicate that the spectra are dominated by the rhombicity of the whole cluster, indicating that the zero-field splitting parameters are significant in the Se-incorporated FeMo-cofactor. Interpretation of the meaning of this analysis is difficult, and will require more experiments analyzing the influence of Se in the FeMo-cofactor.

*All EPR experiments and analysis were done in collaboration with the research group of Prof. Dr. Stephan Weber (Albert-Ludwigs-Universität Freiburg, Germany) by Lorenz Heidinger and Dr. Erik Schleicher.

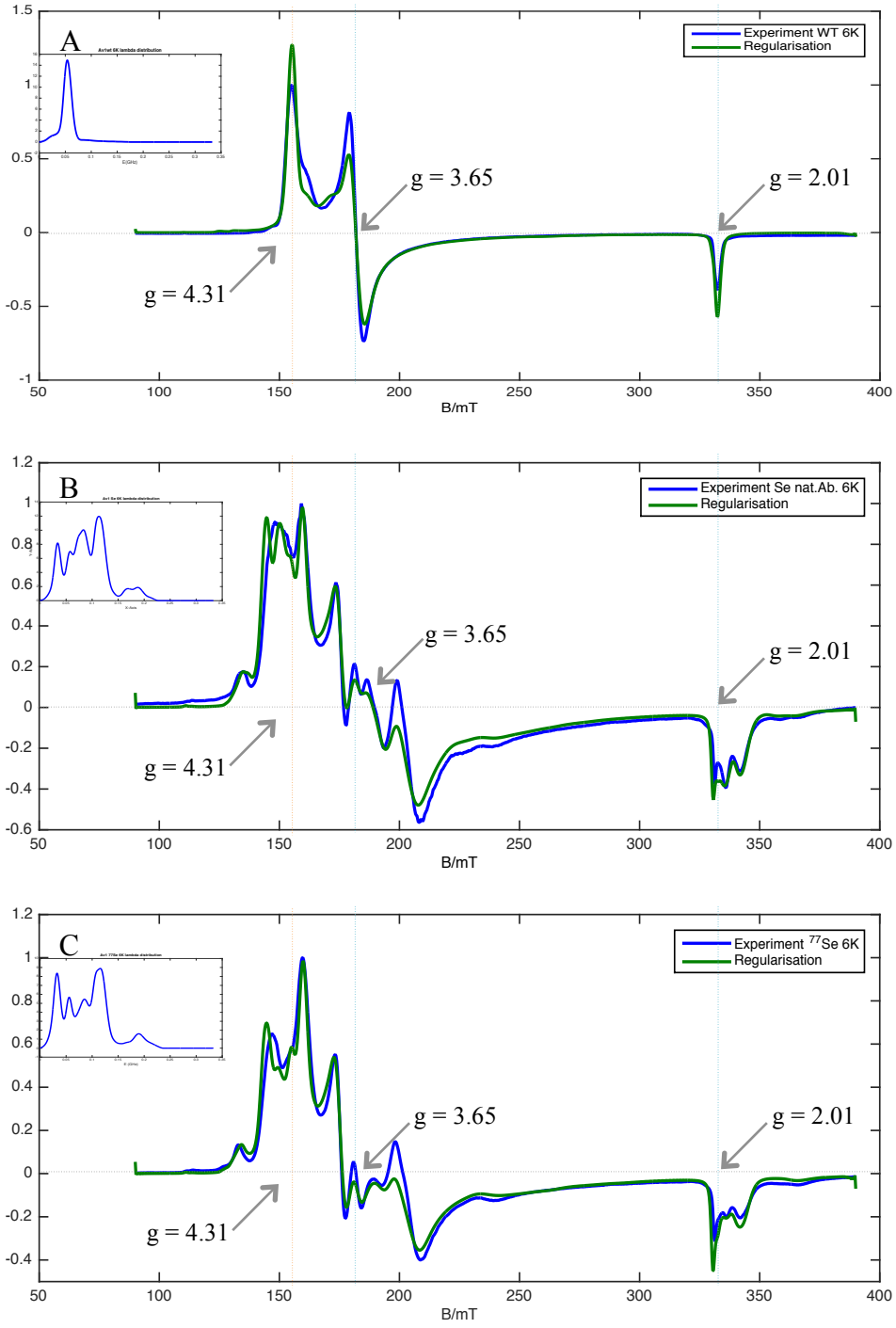

Figure 37: X-band cw-EPR spectra of: A) Av1 (wild type), B) Av1_Se2B, C) Av1_^{77}Se2B taken at 6K. The expected g-values for Av1 (wild type) are shown. Insets show the E-value determination showing a number of peaks for λ-values fit for the two Se-incorporated samples.

3-Pulse ESEEM of site-specifically Se-incorporated MoFe-protein

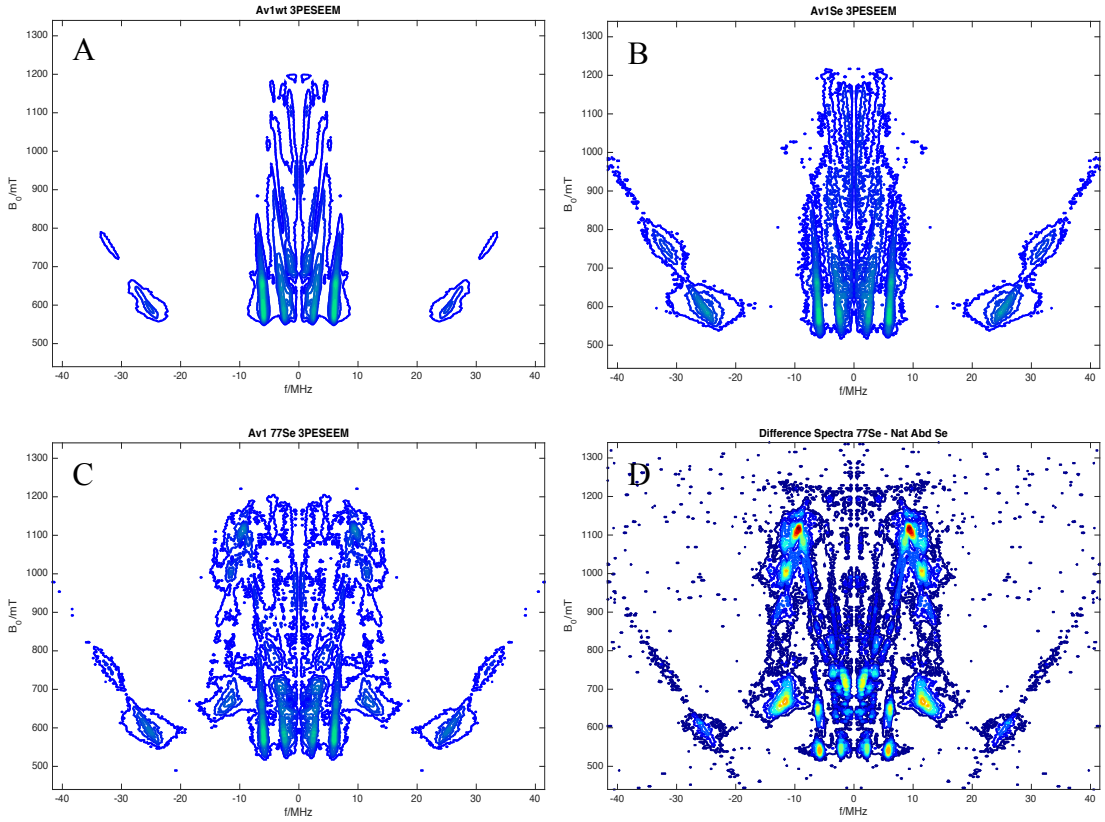

Figure 38: 3-Pulsed ESEEM of: A) Av1_wt, B) Av1_Se2B (natural abundance), C) Av1_^{77}Se2B (isotopically labeled), and D) Difference spectrum for the 3P-ESEEM of Av1_Se2B – Av1_^{77}Se2B. The difference spectrum in D) shows the hyper-fine coupling between the ^{77}Se (I = 1/2) and, presumably, electrons coupled to FeMo-cofactor.

Analysis of 3-pulsed ESEEM experiments demonstrate the presence of hyperfine coupling when isotopically labeled ^{77}Se is site-specifically incorporated into the FeMo-cofactor. Comparison of the wild-type and selenium-labeled samples shows similar frequencies. Signals at frequencies below 8 MHz correspond to nitrogens in the sample, and above 20 MHz correspond to protons present.

A peak located at ~12 MHz (B_0 = 660 mT) seen in the Av1_^{77}Se2B spectrum is expected to have originated from the presence of ^{77}Se, and analysis of the difference spectrum shows a blue/green area corresponding with this peak, indicative of hyperfine coupling derived from ^{77}Se (as it is not present in the natural abundance Av1_Se2B spectrum, it is expected

that it corresponds with the I = ½ nucleus) (see figure 38 a-c for plotted spectra and d for difference spectrum).

*All ESEEM experiments and analysis were done in collaboration with the research group of Prof. Dr. Stephan Weber (Albert-Ludwigs-Universität Freiburg, Germany) by Lorenz Heidinger and Dr. Erik Schleisser.

Structural Characterization CO-inhibited and Reactivated MoFe-protein

Determination of ligand binding to the FeMo-cofactor has been an arduous process due to requirements including reduction of the FeMo-cofactor by 2- to 4- electrons delivered by the Fe-protein [41], and the ubiquitous reduction of protons, indicative of transient intermediate states. Trapping intermediate substrate bound states is additionally difficult due to the requirement of both the Fe- and MoFe- proteins, making samples not only heterogeneous with regard to proteins present, but also making the electronic states of the metals in the proteins likely mixed. The resulting distribution of intermediates makes both structural and spectroscopic investigations non-trivial.

Due to these difficulties, inhibitors are potentially powerful tools for stably trapping ligand bound states that can provide insight into the substrate binding and reduction mechanism. Structural characterization of the FeMo-cofactor with a bound substrate/inhibitor provides direct insight into previously unknown information regarding the ligand binding site and mode. Carbon monoxide (CO) is a potent non-competitive inhibitor for all substrates, except protons [59, 115], and is especially attractive because it is isoelectronic to N_2, is a reversible inhibitor, and only binds to partially reduced MoFe-protein generated under turnover conditions. Although noncompetitive inhibitors are traditionally considered to bind at distinct sites from the native substrate, the complexity of catalysis by nitrogenase, including multiple oxidation states and potential binding modes, makes this distinction less relevant [61]. Recent investigations have shown that CO is also a weak substrate, which during reduction undergoes C-C bond formation to form hydrocarbons, in a reaction reminiscent of Fischer-Tropsch synthesis [116, 117]. CO binding has been investigated using spectroscopic techniques, most notably EPR and IR spectroscopies, which have revealed a variety of CO-bound species dependent upon the partial pressure of CO present [61, 63, 66, 115, 118-120]. Despite the numerous studies that have been carried out, a structurally explicit characterization of any CO-bound state has not been accomplished previously.

Based upon this background, we have developed a method for preparing CO-inhibited samples and prepared crystal samples optimized for X-ray crystallographic analysis. Optimization of CO-inhibited sample preparation and crystallization led to the refinement of a structure of 1.50 Å resolution. Analysis of the electron density ($2F_{obs}$-F_{calc}) and the anomalous different density map calculated at 7100 eV (this energy was chosen because it is below the K-edge for Fe, and S has a comparably significant anomalous contribution at this energy) demonstrated that the CO bound to the FeMo-cofactor in a μ_2-bridging mode, displacing the S2B belt-sulfur, and causing the FeMo-cofactor to lose its intrinsic three-fold symmetry (see figure 26). This is the first experimental evidence that the FeMo-cofactor undergoes structural changes during catalysis.

Considering the complete displacement of the S2B sulfur, we assessed whether the CO-inhibited protein was irreversibly inactivated or could be reactivated. Reactivation was accomplished by placing the CO-inhibited protein in activity assays containing acetylene, and activity was measured through the production of ethylene. Reactivation was possible with both CO-inhibited protein crystals, and with CO-inhibited MoFe-protein isolated from CO-saturated activity assays. Re-isolation and crystallization of the reactivated MoFe-protein resulted is a 1.43 Å resolution structure that displayed complete return of a sulfur in the S2B site. The ability to reactivate the protein and the return of the ejected sulfur indicates that the CO-bound state is a relevant catalytic species.

The crystallographic structures of the CO-bound, and reactivated, FeMo-cofactor has important implications for the mechanism of substrate reduction by nitrogenase. The CO-binding site is adjacent to two side chains that were previously shown to alter substrate reduction activity; α-His195 is 2.8 Å away (NE2–OC distance) and α-Val70 is 3.4 Å (closest methyl–OC distance). An α-His195 mutation to α-Gln195 resulted in the loss of N_2 reduction activity, and mutations to the α-Val70 to α-Ala70 and α-Gly70 enabled reduction of longer hydrocarbon substrates and indicated the involvement of Fe6 in substrate reduction [94, 121-124]. In the structure of the CO-inhibited MoFe-protein α-

His195 is in hydrogen bonding distant to the oxygen of CO, and α-Val70 directly flanks the binding site (Figure 26D)

Displacement of the S2B sulfur could be facilitated by protonation from α-His195, yielding a HS^- or H_2S species, which would generate a better leaving group than S^{2-}. Dissociation of a sulfur atom opens the possibility for binding at the iron atoms, which are shielded while the belt sulfur is present [92], and provides a reactive site for substrates to bind and be reduced. This also represents a change to the view of the FeMo-cofactor as being structurally inert, and protonation of the belt-sulfur atom could partially account for the required electron donation required for substrate binding.

The CO-bound FeMo-cofactor not only loses the three-fold symmetry due to displacement of the belt-sulfur, but the Fe1-Mo-C axis is no longer aligned, creating an additional asymmetry (figure 26). These adjustments to the structure suggest that the interstitial carbon [125, 126] may act to stabilize the FeMo-cofactor during structural rearrangements and substitutions without loss of structural integrity.

The experimental sample preparation used in these experiments is distinct from that reported in previous spectroscopic studies, precluding assignment of our structure to previous spectroscopic states identified not possible. It is important to note that many of the previously identified states undergo dynamic interchanges, including photoinduced transitions between states [119]. Like the structure presented here, the spectroscopically identified “lo-CO” state has been proposed to involve one molecule of CO bound to the active site in a bridging mode [64, 120]. A state with two CO bound to Fe2 and Fe6 could correspond to the “high-CO” form [66, 118] and might represent an intermediate relevant to the C–C coupling reaction.

The CO-bound and reactivated MoFe-protein structures determined in this crystallographic study demonstrate the structural flexibility of the FeMo-cofactor and provide a detailed view of a ligand bound to the nitrogenase active site. The observations that CO is

isoelectric to N_2, is a potent yet reversible inhibitor of substrate reduction without impeding proton reduction to dihydrogen, and is bound in close proximity to previously determined catalytically important residues emphasize the relevance of the CO-bound structure toward understanding dinitrogen binding and reduction. This sheds light on N_2 activation based on a diiron edge of the FeMo-cofactor and in this respect resembles the Haber-Bosch catalyst that also uses an iron surface to break the N–N triple bond. The demonstrated structural accessibility of CO-bound MoFe-protein opens the door for comparable studies on a variety of inhibitors and substrates, with the goal of understanding the detailed molecular mechanism of dinitrogen reduction by nitrogenase.

Site-specific Se-incorporation and Migration in the FeMo-cofactor

Following the CO-inhibition study, which produced structures of the CO-inhibited and reactivated FeMo-cofactor [109], we applied an alternative approach to analyze ligand binding by site specifically introducing a reporter into the FeMo-cofactor. Due to the reversible displacement of the S2B sulfur by CO [109], its replacement by other substrates/inhibitors was investigated. Potential candidates for inhibitors included Se containing compounds due to its application as a structural surrogate for S in [Fe:S] clusters [114, 127], and its unique crystallographic and spectroscopic properties.

We identified the new inhibitor, $SeCN^-$, and characterized its kinetic properties as an inhibitor and weak substrate in comparison to an analogous, previously identified, inhibitor and substrate, SCN^- [111]. The K_i for $SeCN^-$ was determined to be thirty times lower than SCN^- (410 ± 30 μM vs 12.7 ± 1.2 mM) (figure 29), and crystallographic analysis demonstrated site-specific insertion of a Se from $SeCN^-$ into the S2B site, the site at which CO was shown to bind [109]. The determination that Se, from $SeCN^-$, and CO both bind at this site, displacing a sulfur, highlights the likely role of the Fe2-Fe6 edge as a primary interaction site for substrates and inhibitors. The differences in chemical properties of CO and $SeCN^-$ indicate that this is not simply a specific binding site for a single class of inhibitors or substrates. Our findings substantiate previous evidence that identified the side chains flanking this site as catalytically important through mutagenesis studies [128, 129].

Following the site-specific labeling of the MoFe-protein, we investigated the activity of the Se-incorporated protein and the structural changes induced. Assays measuring substrate reduction by Av1_Se2B (of acetylene, dinitrogen, and protons) showed comparable activity to the wild type protein, with a slight lag phase during the first ten seconds for acetylene reduction (see figure 32), confirming that the incorporated Se had not irreversibly inactivate the enzyme. The slight lag observed at early time points may be due to the difference in producing a labile Se atom as compared to a S atom. Isolation of samples from acetylene reduction assays demonstrated that the Se at the S2B site migrated to the other belt sulfur sites during turnover. This provided the starting point for a time-dependent

analysis of the active site during acetylene turnover. Time dependent analysis of the Se-labeled MoFe-protein required the development of crystallographic sample preparation involving freeze-quench of acetylene reduction assays at specific time points. The resulting crystallographic structures indicate a catalytically dependent migration from the S2B site to the S3A and S5A sites. Early time points imply a preferential migration to the S5A site (figure 33), but whether this is reflective of an ordered sequence or a more complex mechanism cannot be determined from this data. The migration of Se through the S2B, S3A, and S5A sites indicates that these sulfur atoms can interchange and exchange with exogenous ligands during catalysis. These results suggest that substrates may also migrate to different sites of the trigonal six-iron prism during catalysis, exchanging binding positions with the belt-sulfurs. Additionally, complete loss of Se, and replacement with S, is accomplished after a sufficient number of catalytic cycles (Figure 33), although the source of sulfur cannot be determined in these experiments due to multiple sulfur species present, including dithionite and the nitrogenase proteins. The observation that the Se in the S2B site can migrate to the S3A and S5A sites, and ultimately be chased from the FeMo-cofactor during acetylene reduction, indicates that all three belt-sulfur positions are labilized during catalysis. In contrast, no migration was observed during proton reduction.

Elaborating upon our previous study structurally characterizing the CO-inhibited MoFe-protein [109], we sought to similarly CO-inhibit the Av1_S2B protein. The structure of the CO-inhibited Av1_Se2B provided the potential to identify both the reactivity at the S2B site, and the location of the displaced chalcogen. The structure identified that the Se was ca 90% replaced by a CO in a binding geometry nearly identical to that observed in the CO-inhibited Av1 structure [109]. Unexpectedly, the Se at the S2B site was not expelled from the FeMo-cofactor, but had migrated to the S3A and S5A sites (10% remained at the S2B site, 35% migrated to the S3A site, and 44% at the S5A site) (see figure 34). This result supports our findings from the Se-migration during acetylene reduction activity, further indicating that the FeMo-cofactor undergoes structural rearrangements upon binding substrates/inhibitors. Migration from the S2B site into the S3A and S5A sites also indicates that path of net loss of sulfur from the FeMo-cofactor is through either one or both of these

belt-sulfur positions, not simply through simple expulsion as previously indicated [109].

Our results indicate that the resting state structure of the FeMo-cofactor does not represent the catalytic state, and that key features for the substrate interaction (other than protons) require structural changes. Development of a detailed understanding of nitrogenase catalysis must consider cofactor rearrangements during turnover. Furthermore, the ability to site-specifically incorporated selenium into the FeMo-cofactor provides a novel route to probe the substrate reduction mechanism of nitrogenase by exploiting the unique spectroscopic and crystallographic properties of selenium.

Investigation into the potential Sulfur-Binding Site (pSBS)

Upon identification of a potential sulfur species bound in a pocket located at the interface between the α- and β- subunits of the MoFe-protein in the Av1-CO structure [109], we sought to further characterize the binding properties of this pocket. Due to the similar anomalous scattering properties of S and Cl at 7100 eV (0.70 e^- for S and 0.88 e^- for Cl [86], the identity of the anomalous density identified in the Av1-CO structure at the pSBS was not certain. In an attempt to identify this species, we co-crystallized the MoFe-protein with several different anionic species.

In order to determine if this pocket binds sulfur species, we co-crystallized it with SCN^-, and analyzed the electron density ($2F_{obs}$-F_{calc}) map and the anomalous density difference map at 7100 eV. We observed electron density present at this site that indicates the presence of an SCN^- anion (see figure 36), but the mechanistic relevance cannot be fully determined based upon crystallographic data due to the same issues identified in the Av1-CO structure.

Addressing the possibility that this pocket, which has a positive surface charge (see figure 35), is a simple anionic binding pocket, we co-crystallized it with varying concentrations of NaI and NaBr which resulted in no increased electron density from Br^- or I^- at this site, indicating that it is not an indiscriminate anionic binding pocket.

Additionally, we approached our analysis by co-crystallization with KSeCN and analysis of the Av1_Se2B structure. The data for both indicate a low-occupancy selenium (0-20% dependent upon $SeCN^-$ concentration, 10-25 mM) at this site. Unfortunately, the analysis is complicated by the background signal and the electron density observed cannot be fully characterized due to the assigned low occupancy.

The presence of electron density at this site under conditions in which the MoFe-protein is inhibited with CO or SeCN-, and with co-crystallization with SCN-, indicates that this site

may bind sulfur species, but due to the lack of concrete evidence, it cannot be determined whether it is catalytically relevant at this time.

EPR and ESEEM of Av1_Se2B and Av1_^{77}Se2B

Crystallographic characterization of the site-specific insertion of Se into the FeMo-cofactor provides a pathway to characterize this species using spectroscopic techniques. Firstly, the site-specific incorporation effectively "breaks" the three-fold symmetry of the FeMo-cofactor, and provides a structurally specific identification for spectral analysis, and secondly, selenium has a stable isotope, ^{77}Se, that has a nuclear spin of 1/2, making it appropriate for application of resonance techniques.

Nitrogenase has been studied using a variety of spectroscopic techniques including FTIR, EPR, ENDOR, and Mössbauer spectroscopies [38, 57, 63, 66, 130-134]. The three-fold symmetry of the FeMo-cofactor, its complex and poorly understood electronic and magnetic properties, and a mechanism that requires multiple association-dissociation cycles between the two component proteins have made analysis of spectroscopic data quite complicated. Sample preparation alone has proven to be difficult due to the requirement for both component proteins often resulting in samples with mixed species.

By utilizing the site-specificity of the Se-labeling scheme, we have prepared a sample in which we have structurally identified where our label is, and can exploit that to identify changes to the spectrum with comparison to the wild-type MoFe-protein.

In the cw-EPR spectra of the Se-labeled proteins, we see splitting of each g-value (see figure 37) indicative of a zero-field splitting distribution. An analysis of the rhombicity (λ), of the resting-state FeMo-cofactor, resulted in a single peak for the wild-type protein, but analysis of the Se-labeled FeMo-cofactor resulted in five or more peaks. Regularization of the spectra recorded with the applied λ values resulted in good agreement with the spectra, indicating that the rhombicity of the FeMo-cofactor dominates the spectra, implying that zero-field splitting distribution is present in the Se-incorporated samples. This provides a

first look at the effect of Se-incorporation into the FeMo-cofactor, and towards a more detailed analysis of the magnetic and electronic structure.

3-Pulse ESEEM was applied to the Se-incorporated (natural abundance and ^{77}Se isotopically labeled) and wild-type MoFe-protein and was compared with the wild type. Analysis of the spectra show differences between all three samples, with peaks appearing in the Se-labeled sample not apparent in the wild-type spectrum, which is indicative of the zero-field splitting distribution (see figure 38). Analysis of the ^{77}Se labeled sample, and of a difference spectrum comparing the natural abundance Se and ^{77}Se samples highlights peaks at the frequency for ^{77}Se which can be assigned to hyper-fine coupling between the ^{77}Se nucleus unpaired electrons, presumably associated with the FeMo-cofactor.

These EPR and ESEEM spectral data provide the first examples of these experiments on a Se-incorporated FeMo-cofactor. Analysis of the data is preliminary, and requires further examination with varied parameters and samples, but is promising for revealing more information about the complex magnetic and electronic structure of the FeMo-cofactor, which will further this field in unraveling the mechanism of nitrogenase.

References

1. Hoff, A.J., *Advanced EPR: Applications in Biology and Biochemistry*. 1989: Elsevier.
2. Spatzal, T., *Structural, electronic and magnetic characterization of the nitrogenase active site FeMo-cofactor and crystallization of the ketol-acid reductoisomerase from Azotobacter vinelandii*, in *Institut für Organische Chemie und Biochemie*. 2012, Universität Freiburg. p. 180.
3. Duin, E. *Electron Paramganetic Resonance Theory*. [cited 2016 6 January]; course lecture]. Available from: https://www.auburn.edu/~duinedu/epr/1_theory.pdf.
4. Bernhard, A., *The Nitrogen Cycle: Processes, Players, and Human Impact.* Nature Education Knowledge, 2010. **3**(10).
5. Smith, B.E., R.L. Richards, and W.E. Newton, *Catalysts for Nitrogen Fixation: Nitrogenases, Relevant Chemical Models and Commercial Processes*. 2013: Springer Netherlands.
6. McQuarrie, D.A. and J.D. Simon, *Physical Chemistry: A Molecular Approach*. 1997: University Science Books.
7. Strous, M., et al., *Missing lithotroph identified as new planctomycete.* Nature, 1999. **400**(6743): p. 446-449.
8. Fowler, D., et al., *The global nitrogen cycle in the twenty-first century.* Philosophical Transactions of the Royal Society B-Biological Sciences, 2013. **368**(1621): p. 13.
9. Erisman, J.W., et al., *How a century of ammonia synthesis changed the world.* Nature Geoscience, 2008. **1**(10): p. 636-639.
10. Rudnick, P., et al., *Regulation of nitrogen fixation by ammonium in diazotrophic species of proteobacteria.* Soil Biology & Biochemistry, 1997. **29**(5-6): p. 831-841.
11. Hales, B.J., et al., *Isolation of a new vanadium-containing nitrogenase from Azotobacter vinelandii.* Biochemistry, 1986. **25**: p. 7251-7255.
12. Bishop, P.E. and R.D. Joerger, *Genetics and molecular biology of alternative nitrogen fixation systems.* Annu. Rev. Plant Physiol. Plant Mol. Biol., 1990. **41**(109): p. 109-125.
13. Setubal, J.C., et al., *Genome Sequence of Azotobacter vinelandii, an Obligate Aerobe Specialized To Support Diverse Anaerobic Metabolic Processes.* Journal of Bacteriology, 2009. **191**(14): p. 4534-4545.
14. Poole, R.K. and S. Hill, *Respiratory protection of nitrogenase activity in Azotobacter vinelandii - Roles of the terminal oxidases.* Bioscience Reports, 1997. **17**(3): p. 303-317.
15. Hamilton, T.L., et al., *Transcriptional Profiling of Nitrogen Fixation in Azotobacter vinelandii.* Journal of Bacteriology, 2011. **193**(17): p. 4477-4486.
16. Georgiadis, M.M., et al., *Crystallographic structure of the nitrogenase iron protein from Azotobacter vinelandii.* Science, 1992. **257**: p. 1653-1659.

17. Leipe, D.D., et al., *Classification and evolution of P-loop GTPases and related ATPases.* Journal of Molecular Biology, 2002. **317**(1): p. 41-72.
18. Schindelin, H., et al., *Structure of ADP-AlF_4^- stabilized nitrogenase complex and its implications for signal transduction.* Nature, 1997. **387**: p. 370-376.
19. Schindelin, N., et al., *Structure of ADP center dot AIF(4)(-)-stabilized nitrogenase complex and its implications for signal transduction.* Nature, 1997. **387**(6631): p. 370-376.
20. Schlessman, J.L., et al., *Conformational variability in structures of the nitrogenase iron proteins from Azotobacter vinelandii and Clostridium pasteurianum.* J. Mol. Biol., 1998. **280**: p. 669-685.
21. Georgiadis, M.M., et al., *Crystallographic Structure of the Nitrogenase Iron Protein from Azotobacter-Vinelandii.* Science, 1992. **257**(5077): p. 1653-1659.
22. Hu, Y., et al., *Nitrogenase Fe-protein: A molybdate/homocitrate insertase.* Proc. Natl. Acad. Sci. USA, 2006. **103**: p. 17125-17130.
23. Sweeney, W.V. and J.C. Rabinowitz, *PROTEINS CONTAINING 4FE-4S CLUSTERS - AN OVERVIEW.* Annual Review of Biochemistry, 1980. **49**: p. 139-161.
24. Angove, H.C., et al., *An all-ferrous state of the Fe protein of nitrogenase: Interaction with nucleotides and electron transfer to the MoFe-protein.* J. Biol. Chem., 1998. **273**: p. 26330-26337.
25. Angove, H.C., et al., *Mössbauer and EPR evidence for an all-ferrous Fe_4S_4 cluster with S=4 in the Fe protein of nitrogenase.* J. Am. Chem. Soc., 1997. **119**: p. 8730-8731.
26. Tan, M.L., et al., *Protein dynamics and the all-ferrous Fe4S4 cluster in the nitrogenase iron protein.* Protein Science, 2016. **25**(1): p. 12-18.
27. Kim, J. and D.C. Rees, *Crystallographic structure and functional implications of the nitrogenase molybdenum-iron protein from Azotobacter vinelandii.* Nature, 1992. **360**: p. 553-560.
28. Einsle, O., et al., *Nitrogenase MoFe-protein at 1.16Å resolution: A central ligand in the FeMo-cofactor.* Science, 2002. **297**: p. 1696-1700.
29. Spatzal, T., et al., *Evidence for interstitial carbon in nitrogenase FeMo cofactor.* Science, 2011. **334**: p. 940
30. May, H.D., D.R. Dean, and W.E. Newton, *Altered nitrogenase MoFe proteins from Azotobacter vinelandii. Analysis of MoFe proteins having amino acid substitutions for the coserved cysteine residues within the b-subunit.* Biochem. J., 1991. **277**: p. 457-464.
31. Lowe, D.J., K. Fisher, and R.N.F. Thorneley, *Klebsiella pneumonia Nitrogenase: Pre-Steady-State Absorbance Changes Show That Redox Changes Occur in the MoFe Protein That Depend on Substrate and Component Protein Ratio; A Role for P-centres in Reducing Dinitrogen?* Biochem. J., 1993. **292**: p. 93-98.
32. Peters, J.W., et al., *Redox-dependent structural changes in the nitrogenase P-cluster.* Biochemistry, 1997. **36**: p. 1181-1187.
33. Lanzilotta, W.N., et al., *Evidence for coupled electron and proton transfer in the [8Fe-7S]cluster of nitrogenase.* Biochemistry, 1998. **37**: p. 11376-11384.

34. Pierik, A.J., et al., *Redox properties and EPR spectroscopy of the P clusters of Azotobacter vinelandii MoFe protein.* Eur. J. Biochem., 1993. **212**: p. 51-61.
35. Kim, J.S. and D.C. Rees, *Structural Models for the Metal Centers in the Nitrogenase Molybdenum-Iron Protein.* Science, 1992. **257**(5077): p. 1677-1682.
36. Einsle, O., et al., *Nitrogenase MoFe-protein at 1.16 angstrom resolution: A central ligand in the FeMo-cofactor.* Science, 2002. **297**(5587): p. 1696-1700.
37. Spatzal, T., et al., *Evidence for Interstitial Carbon in Nitrogenase FeMo Cofactor.* Science, 2011. **334**(6058): p. 940-940.
38. Lancaster, K.M., et al., *X-ray emission spectroscopy evidences a central carbon in the nitrogenase iron-molybdenum cofactor.* Science, 2011. **334**(6058): p. 974-977.
39. Wiig, J.A., et al., *Radical SAM-dependent carbon insertion into the nitrogenase M-cluster.* Science, 2012. **337**(6102): p. 1672-1675.
40. Lovell, T., et al., *Structural, spectroscopic and redox consequences of a central ligand in the FeMoco of nitrogenase: a density functional theoretical study.* J. Am. Chem. Soc., 2003. **125**: p. 8377-8383.
41. Burgess, B.K. and D.J. Lowe, *Mechanism of molybdenum nitrogenase.* Chem. Rev., 1996. **96**: p. 2983-3011.
42. Hoffman, B.M., et al., *Nitrogenase: A draft mechanism.* Acc. Chem. Res., 2013. **46**(2): p. 587-595.
43. Spatzal, T., O. Einsle, and S.L.A. Andrade, *Analysis of the Magnetic Properties of Nitrogenase FeMo Cofactor by Single-Crystal EPR Spectroscopy.* Angewandte Chemie-International Edition, 2013. **52**(38): p. 10116-10119.
44. Cramer, S.P., et al., *The molybdenum site of nitrogenase. 2. A comparative study of Mo-Fe proteins and the iron-molybdenum cofactor by x-ray absorption spectroscopy.* J. Am. Chem. Soc., 1978. **100**: p. 3814-3819.
45. Lee, H.-I., B.J. Hales, and B.M. Hoffman, *Metal-ion valencies of the FeMo cofactor in CO-inhibited and resting state nitrogenase by ^{57}Fe Q-band ENDOR.* J. Am. Chem. Soc., 1997. **119**: p. 11395-11400.
46. Yoo, S.J., et al., *Mössbauer study of the MoFe protein of nitrogenase from Azotobacter vinelandii using selective ^{57}Fe enrichment of the M-centers.* J. Am. Chem. Soc., 2000. **122**: p. 4926-4936.
47. Harris, T.V. and R.K. Szilagyi, *Comparative Assessment of the Composition and Charge State of Nitrogenase FeMo-Cofactor.* Inorganic Chemistry, 2011. **50**(11): p. 4811-4824.
48. Cramer, S.P., et al., J. Am. Chem. Soc., 1978. **100**: p. 3398-3407.
49. Bjornsson, R., et al., *Identification of a spin-coupled Mo(III) in the nitrogenase iron-molybdenum cofactor.* Chemical Science, 2014. **5**(8): p. 3096-3103.
50. Spatzal, T., et al., *Nitrogenase FeMoco investigated by spatially resolved anomalous dispersion refinement.* Nat Commun, 2016. **7**.
51. Lukoyanov, D., et al., *Unification of reaction pathway and kinetic scheme for N-2 reduction catalyzed by nitrogenase.* Proceedings of the National Academy of Sciences of the United States of America, 2012. **109**(15): p. 5583-5587.

52. Danyal, K., et al., *Electron Transfer within Nitrogenase: Evidence for a Deficit-Spending Mechanism.* Biochemistry, 2011. **50**(43): p. 9255-9263.
53. Lukoyanov, D., et al., *Is Mo Involved in Hydride Binding by the Four-Electron Reduced (E-4) Intermediate of the Nitrogenase MoFe Protein?* Journal of the American Chemical Society, 2010. **132**(8): p. 2526-+.
54. Igarashi, R.Y., et al., *Trapping H- bound to the nitrogenase FeMo-Cofactor active site during H_2 evolution: Characterization by ENDOR spectroscopy.* J. Amer. Chem. Soc., 2005. **127**(17): p. 6231-6241.
55. Huynh, B.H., et al., *Nitrogenase XII: Mössbauer studies of the MoFe protein from Clostridium Pasteurianum W5.* Biochim. Biophys. Acta, 1980. **623**: p. 124-138.
56. Burgess, B.K. and D.J. Lowe, *Mechanism of molybdenum nitrogenase.* Chemical Reviews, 1996. **96**(7): p. 2983-3011.
57. Newton, W.E., et al., *Mössbauer spectroscopy applied to the oxidized and semi-reduced states of the iron-molybdenum cofactor of nitrogenase.* Biochem. Biophys. Res. Commun., 1989. **162**: p. 882-891.
58. Lind, C.J. and P.W. Wilson, *Mechanism of biological nitrogen fixation. VIII. Carbon monoxide as an inhibitor for nitrogen fixation by red clover.* Journal of the American Chemical Society, 1941. **63**: p. 3511-3514.
59. Hwang, J.C., C.H. Chen, and R.H. Burris, *Inhibition of nitrogenase-catalyzed reactions.* Biochim. Biophys. Acta, 1973. **292**(256-270).
60. Cameron, L.M. and B.J. Hales, *Investigation and CO binding and release from Mo-nitrogenase during catalytic turnover.* Biochemistry, 1998. **37**: p. 9449-9456.
61. Davis, L.C., et al., *Iron-sulfur clusters in the molybdenum-iron protein component of nitrogenase. Electron paramagnetic resonance of the carbon monoxide inhibited state.* Biochem., 1979. **18**: p. 4860-4869.
62. Pollock, R.C., et al., *Investigation of Co Bound to Inhibited Forms of Nitrogenase Mofe Protein by C-13 Endor.* Journal of the American Chemical Society, 1995. **117**(33): p. 8686-8687.
63. George, S.J., et al., *Time-resolved binding of carbon monoxide to nitrogenase monitored by stopped-flow infrared spectroscopy.* J. Am. Chem. Soc., 1997. **119**: p. 6450-6451.
64. Lee, H.I., et al., *CO binding to the FeMo cofactor of CO-inhibited nitrogenase: (CO)-C-13 and H-1 Q-band ENDOR investigation.* Journal of the American Chemical Society, 1997. **119**(42): p. 10121-10126.
65. Christie, P.D., et al., *Identification of the CO-binding cluster in nitrogenase MoFe protein by ENDOR of ^{57}Fe isotopomers.* J. Am. Chem. Soc., 1996. **118**: p. 8707-8709.
66. Yan, L.F., et al., *Photolysis of Hi-CO Nitrogenase - Observation of a Plethora of Distinct CO Species Using Infrared Spectroscopy.* European Journal of Inorganic Chemistry, 2011(13): p. 2064-2074.

67. George, S.J., et al., *EXAFS and NRVS Reveal a Conformational Distortion of the FeMo-cofactor in the MoFe Nitrogenase Propargyl Alcohol Complex.* Journal of Inorganic Biochemistry, 2012. **112**: p. 85-92.
68. Scott, A.D., et al., *Structural Characterization of CO-Inhibited Mo-Nitrogenase by Combined Application of Nuclear Resonance Vibrational Spectroscopy, Extended X-ray Absorption Fine Structure, and Density Functional Theory: New Insights into the Effects of CO Binding and the Role of the Interstitial Atom.* Journal of the American Chemical Society, 2014. **136**(45): p. 15942-15954.
69. Lowe, D.J. and R.N.F. Thorneley, *The mechanism of Klebsiella pneumoniae nitrogenase action: The determination of rate constants required for the simulation of the kinetics of N_2 reduction and H_2 evolution.* Biochemical J, 1984. **224**: p. 895-901.
70. Thorneley, R. and D.J. Lowe, *Nitrogenase of Klebsiella pneumonia: Kinetics of the dissociation of oxidized iron protein from molybdenum-iron protein: Identification of the rate-limiting step for substrate reduction.* Biochem. J., 1983. **215**: p. 393-403.
71. Thorneley, R.N.F. and D.J. Lowe, *The Mechanism of Klebsiella-Pneumoniae Nitrogenase Action - Simulation of the Dependences of H-2-Evolution Rate on Component-Protein Concentration and Ratio and Sodium Dithionite Concentration.* Biochemical Journal, 1984. **224**(3): p. 903-909.
72. Thorneley, R.N.F. and D.J. Lowe, *THE MECHANISM OF KLEBSIELLA-PNEUMONIAE NITROGENASE ACTION - PRE-STEADY-STATE KINETICS OF AN ENZYME-BOUND INTERMEDIATE IN N-2 REDUCTION AND OF NH3 FORMATION.* Biochemical Journal, 1984. **224**(3): p. 887-894.
73. Thorneley, R.N.F. and D.J. Lowe, *Nitrogenase: substrate binding and activation.* J. Biol. Inorg. Chem., 1996. **1**: p. 576-580.
74. Howard, J.B. and D.C. Rees, *Nitrogenase: A nucleotide-dependent molecular switch.* Annu. Rev. Biochem., 1994. **63**: p. 235-264.
75. Thorneley, R.N.F. and D.J. Lowe, *Kinetics and mechanism of the nitrogenase enzyme system*, in *Molybdenum Enzymes*, T.G. Spiro, Editor. 1985, John Wiley & Sons, Inc. p. 221-284.
76. Rees, D.C., et al., *Structural basis of biological nitrogen fixation.* Philosophical Transactions of the Royal Society a-Mathematical Physical and Engineering Sciences, 2005. **363**(1829): p. 971-984.
77. Chayen, N.E., *Turning protein crystallisation from an art into a science.* Current Opinion in Structural Biology, 2004. **14**(5): p. 577-583.
78. Ataka, M., *PROTEIN CRYSTAL-GROWTH - AN APPROACH BASED ON PHASE-DIAGRAM DETERMINATION.* Phase Transitions, 1993. **45**(2-3): p. 205-219.
79. Russo Krauss, I., et al., *An Overview of Biological Macromolecule Crystallization.* International Journal of Molecular Sciences, 2013. **14**(6): p. 11643-11691.
80. Drenth, J. and C. Haas, *PROTEIN CRYSTALS AND THEIR STABILITY.* Journal of Crystal Growth, 1992. **122**(1-4): p. 107-109.

81. Rhodes, G., *Crystallography Made Crystal Clear: A Guide for Users of Macromolecular Models*. 2010: Elsevier Science.
82. Debreczeni, J.É. *Data processing*. [pdf, online] 2011; Available from: http://www.ccp4.ac.uk/schools/China-2011/talks/JED-Data_processing.pdf.
83. Weaver, M.L., *The Structure Factor*. 2011.
84. Blow, D., *Outline of Crystallography for Biologists*. 2002: OUP Oxford.
85. Hendrickson, W.A., *DETERMINATION OF MACROMOLECULAR STRUCTURES FROM ANOMALOUS DIFFRACTION OF SYNCHROTRON RADIATION.* Science, 1991. **254**(5028): p. 51-58.
86. Merritt, E.A., *X-ray Absorption Edges*. 1996-2010: Biomolecular Structure Center at UW.
87. Patterson, A.L., *A Fourier series method for the determination of the components of interatomic distances in crystals.* Physical Review, 1934. **46**(5): p. 0372-0376.
88. Hagen, W.R., *Biomolecular EPR Spectroscopy*. 2008: CRC Press.
89. Hagen, W.R., *Metallomic EPR spectroscopy.* Metallomics, 2009. **1**(5): p. 384-391.
90. Mims, W.B., *ENVELOPE MODULATION IN SPIN-ECHO EXPERIMENTS.* Physical Review B-Solid State, 1972. **5**(7): p. 2409-&.
91. Rivera-Ortiz, J.M. and R.H. Burris, *Interactions among substrates and inhibitors of nitrogenase.* J Bacteriol, 1975. **123**(2): p. 537-45.
92. Howard, J.B. and D.C. Rees, *How many metals does it take to fix N_2? A mechanistic overview of biological nitrogen fixation.* Proc. Natl. Acad. Sci. USA, 2006. **103**: p. 17088-17093.
93. Dilworth, M.J., et al., *Effects on substrate reduction of substitution of histidine-195 by glutamine in the a-subunit of the MoFe protein of Azotobacter vinelandii nitrogenase.* Biochemistry, 1998. **37**: p. 17495-17505.
94. Benton, P.M.C., et al., *Localization of a substrate binding site on the FeMo-cofactor in nitrogenase: Trapping propargyl alcohol with an alpha-70-substituted MoFe protein.* Biochemistry, 2003. **42**(30): p. 9102-9109.
95. Mayer, S.M., W.G. Niehaus, and D.R. Dean, *Reduction of short chain alkynes by a nitrogenase alpha-70(Ala)-substituted MoFe protein.* Journal of the Chemical Society-Dalton Transactions, 2002(5): p. 802-807.
96. Lipman, J.G., *Experiments on the Transformation and Fixation of Nitrogen by Bacteria.* Annual Report, New Jersey State Agricultural Experiment Stations, 1903. **24**: p. 217-285.
97. Shah, V.K. and W.J. Brill, *Nitrogenase. IV. Simple method of purification to homogeneity of nitrogenase components from Azotobacter vinelandii.* Biochim. Biophys. Acta, 1973. **305**: p. 445-54.
98. Burgess, B.K., D.B. Jacobs, and E.I. Steifel, *Large scale purification of high activity Azotobacter vinelandii nitrogenase.* Biochim. Biophys. Acta, 1980. **614**: p. 196-209.
99. Yang, K.-Y., et al., *Turnover-dependent inactivation of the nitrogenase MoFe-protein at high pH.* Biochem., 2014. **53**: p. 333-343.

100. Wolle, D., et al., *Ionic interactions in the nitrogenase complex. Properties of Fe-protein containing substitutions for Arg-100.* J. Biol. Chem., 1992. **267**: p. 3667-3673.
101. Barney, B.M., et al., *Trapping a hydrazine reduction intermediate on the nitrogenase active site.* Biochemistry, 2005. **44**(22): p. 8030-8037.
102. Corbin, J.L., *Liquid chromatographic-fluorescence determination of ammonia from nitrogenase reactions: a 2-min assay.* Appl Environ Microbiol, 1984. **47**(5): p. 1027-30.
103. Leslie, A.G., *The integration of macromolecular diffraction data.* Acta Crystallogr D Biol Crystallogr, 2006. **62**(Pt 1): p. 48-57.
104. Evans, P., *Scaling and assessment of data quality.* Acta Crystallogr., 2006. **D62**: p. 72-82.
105. Kabsch, W., *XDS.* Acta Crystallogr., 2010. **D66**: p. 125-132.
106. Emsley, P., et al., *Features and development of Coot.* Acta Crystallogr., 2010. **D66**: p. 486-501.
107. Murshudov, G.N., A.A. Vagin, and E.J. Dodson, *Refinement of macromolecular structures by the maximum-likelihood method.* Acta Crystallogr., 1997. **D53**: p. 240-255.
108. Winn, M.D., et al., *Overview of the CCP4 suite and current developments.* Acta Crystallogr D Biol Crystallogr, 2011. **67**(Pt 4): p. 235-42.
109. Spatzal, T., et al., *Ligand binding to the FeMo-cofactor: structures of CO-bound and reactivated nitrogenase.* Science, 2014. **345**(6204): p. 1620-3.
110. Stefan Stoll, A.S., *EasySpin, a comprehensive software package for spectral simulation and analysis in EPR.* J. Magn. Reson., 2006. **178**(1): p. 42-55.
111. Rasche, M.E. and L.C. Seefeldt, *Reduction of thiocyanate, cyanate and carbon disulfide by nitrogenase: kinetic characterization and EPR spectroscopic analysis.* Biochem., 1997. **36**: p. 8574-8585.
112. Li, J.G., B.K. Burgess, and J.L. Corbin, *Nitrogenase Reactivity - Cyanide as Substrate and Inhibitor.* Biochemistry, 1982. **21**(18): p. 4393-4402.
113. Thomas Spatzal, K.A.P., James B Howard, Douglas C Rees, *Catalysis-dependent selenium incorporation and migration in the nitrogenase active site iron-molybdenum cofactor.* eLife, 2015. **4**(e11620).
114. Zheng, B., et al., *Selenium as a Structural Surrogate of Sulfur: Template-Assisted Assembly of Five Types of Tungsten-Iron-Sulfur/Selenium Clusters and the Structural Fate of Chalcogenide Reactants.* Journal of the American Chemical Society, 2012. **134**(14): p. 6479-6490.
115. Cameron, L.M. and B.J. Hales, *Investigation of CO binding and release from Mo-nitrogenase during catalytic turnover.* Biochemistry, 1998. **37**(26): p. 9449-9456.
116. Lee, C.C., Y.L. Hu, and M.W. Ribbe, *Vanadium Nitrogenase Reduces CO.* Science, 2010. **329**(5992): p. 642-642.
117. Hu, Y.L., C.C. Lee, and M.W. Ribbe, *Extending the Carbon Chain: Hydrocarbon Formation Catalyzed by Vanadium/Molybdenum Nitrogenases.* Science, 2011. **333**(6043): p. 753-755.

118. Lee, H.-I., et al., *CO binding to the FeMo cofactor of CO-inhibited nitrogenase: ^{13}CO and ^{1}H Q-band ENDOR investigation.* J. Am. Chem. Soc., 1997. **119**: p. 10121-10126.
119. Maskos, Z. and B.J. Hales, *Photo-lability of CO bound to Mo-nitrogenase from Azotobacter vinelandii.* J. Inorg. Biochem., 2003. **93**(1-2): p. 11-17.
120. Pollock, R.C., et al., *Investigation of CO bound to inhibited forms of nitrogenase MoFe protein by ^{13}C ENDOR.* J. Am. Chem. Soc., 1995. **117**: p. 8686-8687.
121. Kim, C.H., W.E. Newton, and D.R. Dean, *Role of the Mofe Protein Alpha-Subunit Histidine-195 Residue in Femo-Cofactor Binding and Nitrogenase Catalysis.* Biochemistry, 1995. **34**(9): p. 2798-2808.
122. Dos Santos, P.C., et al., *Alkyne substrate interaction within the nitrogenase MoFe protein.* Journal of Inorganic Biochemistry, 2007. **101**(11-12): p. 1642-1648.
123. Scott, D.J., et al., *Role for the nitrogenase MoFe protein a-subunit in FeMo-cofactor binding and catalysis.* Nature, 1990. **343**: p. 188-190.
124. Christiansen, J., et al., *Isolation and characterization of an acetylene resistant nitrogenase.* J. Biol. Chem., 2000. **275**: p. 11459-11464.
125. Rittle, J. and J.C. Peters, *Fe-N-2/CO complexes that model a possible role for the interstitial C atom of FeMo-cofactor (FeMoco).* Proceedings of the National Academy of Sciences of the United States of America, 2013. **110**(40): p. 15898-15903.
126. Dance, I., *Elucidating the coordination chemistry and mechanism of biological nitrogen fixation.* Chemistry-an Asian Journal, 2007. **2**(8): p. 936-946.
127. Meyer, J., et al., *Replacement of Sulfur by Selenium in Iron-Sulfur Proteins.* Advances in Inorganic Chemistry, 1992. **38**: p. 73-115.
128. Sarma, R., et al., *Insights into substrate binding at FeMo-cofactor in nitrogenase from the structure of an alpha-70(Ile) MoFe protein variant.* Journal of Inorganic Biochemistry, 2010. **104**(4): p. 385-389.
129. Kim, C.-H., W.E. Newton, and D.R. Dean, *Role of the MoFe protein a-subunit histidine-195 residue in FeMo-cofactor binding and nitrogenase catalysis.* Biochemistry, 1995. **34**: p. 2798-2808.
130. Lancaster, K.M., et al., *X-ray Spectroscopic Observation of an Interstitial Carbide in NifEN-Bound FeMoco Precursor.* Journal of the American Chemical Society, 2013. **135**(2): p. 610-612.
131. Yan, L.F., et al., *IR-Monitored Photolysis of CO-Inhibited Nitrogenase: A Major EPR-Silent Species with Coupled Terminal CO Ligands.* Chemistry-a European Journal, 2012. **18**(51): p. 16349-16357.
132. Doan, P.E., et al., *Fe-57 ENDOR Spectroscopy and 'Electron Inventory' Analysis of the Nitrogenase E-4 Intermediate Suggest the Metal-Ion Core of FeMo-Cofactor Cycles Through Only One Redox Couple.* Journal of the American Chemical Society, 2011. **133**(43): p. 17329-17340.
133. Tolland, J.D. and R.N.F. Thorneley, *Stopped-flow Fourier transform infrared spectroscopy allows continuous monitoring of azide reduction, carbon*

monoxide inhibition, and ATP hydrolysis by nitrogenase. Biochemistry, 2005. **44**(27): p. 9520-9527.
134. Spee, J.H., et al., *Redox properties and electron paramagnetic resonance spectroscopy of the transition state complex of Azotobacter vinelandii nitrogenase.* FEBS Letters, 1998. **432**: p. 55-58.

Acknowledgements

Throughout my graduate school, there have been quite a few people who have made this experience absolutely wonderful, who have supported me when I needed it, listened to me complain, and provided me with countless hours of laughter and joy. I cannot express my gratitude…

Firstly, I would like to thank my thesis committee; they have been incredibly supportive and helpful throughout my entire time here at Caltech.
Doug, thank you for being my advisor, always pushing me to do my best and who providing me with much support and kindness. Your pushed me towards a wonderful project, maybe reluctantly…, that turned out to be a fantastic experience.
Jack, thank you for being a wonderful committee chair, helping me along through the years and always being available when I needed to talk!
Mitchio, thank you for being so supportive and kind and caring when tough times arose and always making me feel welcome.
Long, thank you for always been there to talk about science and for supporting me when I needed it.

Felicia Hunt, thank you for your kindness, support, and understanding. You made an incredible difference in my time here at Caltech.

Thank you to the wonderful administrators here at Caltech, especially Phoebe, Agnes and Anne. Phoebe, thank you for always helping out with everything with our lab and putting together such great parties for us! Thank you to Anne and Agnes for keeping everything moving and ensuring that paperwork and keys and reports were filed.

The Rees lab has been a wonderful place to spend my time in graduate school. I have had the pleasure to work with a great group of people who have taught me so much and provided me with so many laughs.

Team Nitro, wow… what a fantastic sub-group. I have had so many great times with all of you (Thomas, Limei, Belinda, Renee, Helen, Christine, Kyu, Felix, and Corinna). Long days of protein purification and activity assays were always pretty fun because of you guys (even if I did complain sometimes! Ha ha!). I can't imagine a better group of people to work with.

I would also like to thank Lorenz and Erik from the Weber group in Freiburg. Collaborating with you has been fun and exciting!

There are so many people I would like to thank for their friendship and support…

Janet and Selene (and Max and Sam!), thank you for being such wonderful friends… you both have made my time at Caltech so much fun. I will miss our coffee dates at Busters, but I'm sure we can find more coffee place in the bay area and Berlin! Can't wait for you to visit, and to visit you!

Kana and Laurence, you two were my first Caltech friends! I am so proud of both of your accomplishments, but more importantly, I am so happy to call you friends. You are both people who I look up to in so many ways, your kindness and patience are always so impressive. I look forward to visiting you both in Texas and Maine, and hope to see you in Berlin!

To the Euro group... Tobias, Evelyn, Ana, Joao, Alex, Karsten, Goga, Felix, thank you so much for the great times out with Stammtisch (and some German lessons)! All of you have been so much fun, and so kind to me! I hope to have lots of destination meet-ups!!!

To Andy and Belinda, thank you both so much for all of the fantastic times we have spent together! You have both been great friends to me, and incredible supportive… even reading through my terrible writing and providing me with great feedback. I still owe you both quite a few drinks, so you will have to come to Germany for drinks(sssss!)!!!

To Renee and Keith, thank you both so much for your friendship, kindness, and support! From having cocktails to eating junk food, we have had a lot of great times together! See you in Germany!

Helen and Erik, thank you both for being the fun and quirky pair that never fails to make me laugh! Helen, we have been at Caltech together the whole time! Between taking classes to taing together to working together in the end! It has been fantastic! I hope to see you in Europe!
To Phong and Duong, thank you both for being so kind. Phong, your cheerful attitude, never ending helpfulness, and laugh made coming to the Broad lab always fun. I hope to see you both in Berlin in the near future!

A little extra thank you to Belinda, Renee, and Helen… my office cohorts, friends, and best wine-drinking, cheese-night, fancy-lady day, treat-yo'self, lady-in-a-van, office-pranking, purification-day, Wednesday-night out ladies!!! I will miss our coffee breaks and laugh out loud afternoons more than you can imagine… I will try to keep teasing Thomas to remind him or how good he had in an office with five women… but it won't be the same without you!

To Nic, I would never have even applied to graduate school, or for my undergraduate degree for that matter, without your support. You always believed in me and encouraged me to grow and learn and develop. I can't tell you how much you have helped me to get to where I am today. Thank you…

To Amy and Malinda, you have been my best friends for a long time now, and you have never failed to support me when I needed it, cheer me up when I was down, calm me down when I was too crazy, listen when I needed to talk, and talk when I needed your advice. You are the ladies I hope to become old with and talk about when we were young together. Looking forward to the next 23 years (and more!!!) of our friendship!

To Thomas… you have made the last few years really amazing… You taught me so much in the lab, and welcomed me back to team nitro with so much kindness. I even learned to love crystallography… who ever would have bet that before could have made a lot of money! I can't thank you enough for working with me and for all of your help and support throughout these projects. More importantly though, the fantastic adventures we had in California were some of the best times ever; I can't express how much they meant to me. I can't wait for our next adventures in Europe, and those beyond!!!

To my family, I cannot thank you enough… You have been my biggest supporters and provided me with so much love and kindness throughout my life. You have made getting to, and getting through graduate school wonderful, and I can't tell you how much all of that means to me. Thank you so much for helping me when I needed it, and letting me get through things myself, while always knowing you would be there if I needed it.

Thank you!!! Vielen Vielen Dank!!! Muchisimas Gracias!!!